UNDERSTANDING THE IMPACT OF GEOLOGY

IN SUBSURFACE RESERVOIR

FLOW PROCESSES

by

Justin Wriedt

A dissertation submitted to the faculty of
The University of Utah
in partial fulfillment of the requirements for the degree of

Doctor of Philosophy

Department of Chemical Engineering

The University of Utah

May 2014

The University of Utah Graduate School

STATEMENT OF DISSERTATION APPROVAL

The following faculty members served as the supervisory committee chair and members for the dissertation of _____ Justin Wriedt _____ . Dates at right indicate the members' approval of the dissertation.

Milind D. Deo	, Chair	2/20/2014
		Date Approved
John McLennan	, Member	2/12/2014
		Date Approved
Peter Rose	, Member	1/14/2014
		Date Approved
Brian McPherson	, Member	2/13/2014
		Date Approved
Thomas Doe	, Member	1/13/2014
		Date Approved

The dissertation has also been approved by Milind D. Deo, Chair of the Department of Chemical Engineering and by David B. Kieda, Dean of The Graduate School.

ABSTRACT

Geology plays an important role in the subsurface reservoir flow processes. It is necessary to understand the interaction of geology and multiphase physics in various settings. This work investigates the interaction of multiple types of fluids in different depositional settings.

The first study is an investigation of risk analysis of carbon dioxide sequestration in a relatively homogenous sandstone. To properly screen sequestration sites it is necessary to understand how different geologic parameters influence potential risk factors. This is achieved by using a methodology that combines experimental designs with Monte Carlo sampling to develop probability density functions of these critical risk factors. These probability density functions can be used as a first-order screening method during geologic sequestration site selection.

The second study involves a full field study to understand the potential for long-term subsurface storage of carbon dioxide given a highly detailed geologic model with limited field production history. An application of best practices for a single well pattern is applied to the northern platform of the SACROC reservoir to determine the ideal conditions for economic return and carbon dioxide sequestration. It is found that either sequestration or oil recovery must be the primary goal with the other becoming secondary.

The final investigation involves a unique reservoir type where all fluid flows in faults and fractures rather than the matrix. This investigation attempts to understand the flow dynamics under various geologic and fluid parameter ranges to develop a method for

history matching these reservoirs. This is done using a simple model for a parametric study which will assist in understanding the production controls in basement reservoirs. This investigates whether low-rate recoveries will achieve higher overall recoveries due to the flow dynamics in faults and fractures. In no scenario was it possible to recover a higher volume of oil at lower recovery rates unless the geologic parameters are flow rate dependent, which is difficult to justify at this time. In each of these studies the impact of the geological parameters is used to determine either the risk factors or to develop optimal methods for economic recovery of reservoir fluids.

This is dedicated to my wife Tiffany and our children for their unconditional love and support during my studies.

TABLE OF CONTENTS

LIST OF FIGURES

LIST OF TABLES

ACKNOWLEDGEMENTS

CHAPTER 1

INTRODUCTION

Conceptual models are an integral part of the decision making process for reservoir engineers. The conceptual model describes the essential properties of the system but simplifies or makes assumptions about minor features and processes to reduce the computational cost of the simulation. Understanding the geologic data can improve the conceptual model of the reservoir and assist in improving decision making. The relationship between rock and fluid is the basis for developing models, interpretations and forecasting in reservoir engineering. Rock properties are mostly theoretical and correlations have been developed to predict specific physical properties using simplified physical concepts. These models are useful for predicting rock properties using arbitrary parameters. These imperfect solutions are generally accepted with some level of uncertainty, usually quantified with statistical trends or upper and lower bounds. It is important to understand how these essential geologic properties and complex multiphase flow processes interact.

There are challenges associated with integrating geology and engineering in reservoir modeling. Integrating the geologic information that is acquired at different scales is critical for geologic modeling. It is also necessary to understand and incorporate the uncertainties of these geologic parameters, where data is limited, in these models. As natural fractures become essential to oil recovery in nanoporous rocks, proper representation and modeling

are needed to understand the role they play in ultimate recoveries. All of the outcomes of the reservoir models will depend on the geologic characterization and complex physical models. The uncertainty in the outcomes can be compounding therefore every attempt must be made to understand these complex interactions at multiple scales. Throughout this work, attempts are made to understand the propagation and effect of uncertain geologic parameters and the physical models that are used. This work also seeks to integrate fracture modeling into reservoir models while considering the uncertainty in characterization, unique flow properties in fractures and interactions between faults and fractures.

Petrophysics is the study of the physical and chemical properties of rocks and their contained fluids and is important when determining geologic parameters. It relates the pore system to its fluid saturation distribution and flow characteristics. This is key in determining the interdependent reservoir and fluid characteristics including formation thickness, lithology, porosity, fluid saturations and pressures, fluid identification and characterization, permeability, and relative permeabilities. These properties all have large uncertainties that are difficult to define but are critical in dynamic flow reservoir engineering calculations.

In reservoir engineering, wettability is defined in terms of the interaction between two immiscible fluids and reservoir rock. Reservoir rocks are typically described as being water-wet, oil-wet, or intermediate-wet. A water-wet rock surface has a strong preference to be coated by the water phase. Oil-wet rocks prefer to be coated by the oil phase. Intermediate-wet describes reservoir rocks that have both water-wet and oil-wet surfaces. Defining the type of wettability for reservoir rocks is estimated with laboratory measurements that have some uncertainty associated with them.

There is high variability in petrophysical properties in different depositional

environments. There is also high spatial variability within a particular formation in a given geologic deposit. Clastics can be deposited by wind and water with a range of energies. These reservoirs are geologically young and the sediment has generally undergone limited compaction and cementation. Carbonates form in many environments by precipitation from water; either straight from the water, or induced by organisms, to make their shells or skeletons. The geologic properties will vary depending on the particular environment where the carbonates form. Igneous rocks are formed from the cooling of molten rock (magma). They are crystalline, which means they are made up of crystals joined together. Intrusive rocks are igneous rocks which form at depth. They take tens of thousand of years to cool. Due to the crystalline nature of these types of rocks, there is generally little or no flow in the matrix relative to faults and fractures that occur in these formations.

Primary oil production uses the reservoir's natural energy in the form of fluid and rock expansion, solution-gas drive, gravity drainage and aquifer influx. Secondary recovery, usually in the form of waterflooding, is used to increase oil production rates as the natural energy declines. Injection of water is a method to increase reservoir pressure to discovery levels and maintain those levels using voidage replacement. Water displaces oil from pore spaces due to buoyant forces, however, the efficiency is dependent on factors such as oil viscosity and rock characteristics. Tertiary recovery follows waterflooding and utilizes enhanced oil recovery (EOR) techniques such as thermal methods, gas injection (i.e., carbon dioxide), and chemical flooding. Recent reservoir development techniques may actually apply EOR methods at any stage of reservoir development to improve production.

Subsurface fluids occur in a variety of conditions and phases with a large variability in properties. Carbon dioxide becomes a supercritical fluid below depths of 800 meters where the density and viscosity properties are similar to liquids. The density is generally lower

than water and oil at formation temperatures and pressures which allows the CO_2 plume to migrate vertically. When CO_2 comes in contact with brine in reservoirs it begins to dissolve, up to the solubility limit. CO_2 is commonly used for miscible displacement in oil reservoirs to improve recovery and maintain pressure. Carbon dioxide is the most suitable fluid for EOR because it reduces the oil viscosity and reduces the interfacial tension between water and oil.

There is risk that CO2 may leak out of a storage reservoir through natural (faults) and man-made pathways (abandoned wells). A conceptual model is developed to address these risks and attempts to quantify them. For geologic sequestration in saline aquifers there is considerable uncertainty in the geologic parameters in the subsurface. Site screening is the first step in deep saline aquifer characterization and is dependent on data availability. Due to limited data, a range of expected properties must be used in numerical flow modeling. Potential sequestration sites can have a range of formation depths, thickness, permeability and porosity. There is also uncertainty in the formation fluids, such as brine salinity and the hysteresis of the brine displacement after injection ends.

A conceptual model is developed to determine the optimal methods for enhanced oil recovery and carbon dioxide storage in mature oil fields. The Scurry Area Canyon Reef Operator's Committee (SACROC) reservoir is a carbonate reef depositional environment with a long production history. The geologic model is well defined by the Texas Bureau of Economic Geology. Optimal application of enhanced recovery methods depends on reservoir temperature, pressure, depth, residual oil and water saturations, oil properties (i.e., viscosity and minimum miscibility pressure), permeability and porosity. This conceptual model required determination of the residual oil, water and carbon dioxide saturations as well as pressures prior to the forecast modeling.

The rock characteristics are especially unique in basement reservoirs where the faults and fractures define the flow characteristics. In general there is very high water production relative to oil production during waterflooding in fractured basement reservoirs. It is critical to understand how the properties of the faults and fractures interact to maximize oil recovery and minimize water production. This conceptual model seeks to understand how production rate affects oil recovery in a heterogeneous fault network. It also identifies the controlling parameters that affect oil recovery and water production in fractured basement reservoirs.

CHAPTER 2

A METHODOLOGY FOR QUANTIFYING RISK AND LIKELIHOOD

OF FAILURE FOR CARBON DIOXIDE INJECTION

INTO DEEP SALINE RESERVOIRS

Justin Wriedt[a], Milind Deo[a], Weon Shik Han[b] and Jim Lepinski[c]

2.1. <u>Abstract</u>

Tectonically stable deep saline reservoirs are considered to be the most abundant carbon dioxide (CO_2) sequestration sites. Pressure, temperature, salinity and other characteristics of these geologic formations vary at each injection site. It is essential to understand the roles of geologic and engineering factors to optimize the CO_2 injection conditions and to quantify the associated risks. Factors such as the magnitude of injection-induced reservoir pressure, quantity of supercritical phase CO_2 that comes in contact with caprock, and the amount of residually trapped CO_2 govern the fate of CO_2, and provide quantitative assessment of the storage integrity.

a.) Department of Chemical Engineering, 50 Central Campus Drive, University of Utah, Salt Lake City, Utah 84112.; b.) Department of Geosciences, University of Wisconsin-Milwaukee, Milwaukee, Wisconsin 53201; c.) Headwaters Clean Carbon Services, 10653 River Front Parkway # 300, South Jordan, Utah 84095-3527.

A streamlined protocol was developed using response surface methodology to quantify the risks related to CO_2 injection. The proposed methodology includes the design of simulation scenarios, selection and screening of parameters, multiple-linear regression of outcomes, and the development of probability density functions (PDF) of various potential risk factors. Multiphase numerical simulations were performed to understand the behavior of the injected CO_2 and associated parameters in deep saline reservoirs with prescribed geometries and petrophysical properties. Formation thickness, formation depth, porosity, horizontal permeability, brine density, and the end-point residual CO_2 saturation were the six critical parameters identified that affected important outcomes. A six-factor Box-Behnken experimental design procedure was used to establish an understanding of the sensitivity of the parameters on the important factors, and for subsequently establishing response surfaces. Closed boundary domains with different operational constraints were employed. A stepwise, sequential regression method was used to determine statistically significant coefficients of a response surface model. Monte Carlo simulations with logical distributions of input parameters were performed using the response surface coefficients. Uncorrelated and correlated porosity-permeability distributions were used to generate two types of probability density functions (PDF). PDFs of CO_2 plume extent under the caprock and average reservoir overpressure after injection were generated given *all* of the variability in the input parameters. These results will allow initial screening of a large number of potential injection sites without detailed simulations of each.

2.2.   Introduction

Carbon dioxide (CO_2) emissions are believed to be a cause of recent increase in mean global temperature. Capturing CO_2 from industrial sources and storing it in deep

permeable geologic formations has been proposed as an option to reduce atmospheric CO_2 concentrations [1]. Potential geologic formations include unmineable coal seams, depleted oil and gas reservoirs, and deep saline reservoirs. The deep and regional-scale saline aquifers contain over 90 percent of the subsurface volume available for storage. Their relative abundance in sedimentary basins make them attractive candidates for geologic CO_2 sequestration [2-3].

Currently, pilot- to commercial-scale geologic CO_2 sequestration demonstrations are being conducted in various geographical regions [4-5]. In the North Sea, CO_2 associated with produced gas from underlying reservoirs is being separated and injected into the Utsira formation [6-7]. Other applications include on-shore Nagaoka pilot test in Japan [8-9] and a commercial-scale Cranfield test in Texas where CO_2 is injected into a formation below 3,000 meters [10]. Storage of anthropogenic CO_2 in geologic formations has also been tested at several other locations [9, 11].

The pressure build-up resulting from CO_2 injection may induce preferential flow pathways within caprock or possibly activate faults adjacent to CO_2 injection sites, inducing an upward migration of brine from the injection formation to shallow potable water-storing formations [12]. Thus, CO_2 facilities should be designed to minimize pressure build-up to reduce the geomechanical impact on caprock integrity.

Experimental design methods are efficient in evaluating the effects of modeling input parameters and ranking the most important parameters within the system dynamics, and hence are effective tools for investigating risks of sequestration operations. The parameters such as permeability and porosity are typically based on the ranges encountered at potential sequestration sites.

Experimental design methods were originally developed for quality assurance purposes, but have since been used for many applications [13]. Experimental design refers to the process of planning an experiment so that appropriate data will be collected and analyzed by statistical methods, and valid and objective conclusions [14] are reached. A variety of experimental design methods exist where multiple parameters can be efficiently studied while including their interactions [15-16]. Experimental design methods have been utilized in many reservoir engineering applications, including reservoir performance prediction [17], uncertainty modeling [18-20], sensitivity studies [21-24], upscaling [25-26], history matching [27], and development optimization [28].

Selection of the design matrix is dependent on the study objective. The most commonly used experimental designs are two- and three-level designs where each achieves a different goal. A two-level design varies the inputs between the two extremes of the range of values. These designs are primarily used for screening input variables for sensitivity studies. The most common of these two-level designs are Plackett-Burman and 2^k factorial. For three-level designs, the inputs are varied between the two extremes of the range of values, and the midpoints of those extremes. These designs are better suited for predicting the output responses due the quadratic nature of the design. Response surface models should accurately predict the responses at conditions not used in their generation with acceptably small errors. The most commonly used three-level designs are 3^k factorial, Central Composite design, and Box-Behnken design.

An investigation of stratigraphic models with varying complexity levels and their effects on CO_2 sequestration outcomes, such as brine leakage, and trapped, dissolved and mobile gas, has been performed [29]. This study uses a two-level Plackett-Burman, which is most useful as a screening tool but typically not appropriate for response surface

development. An important result of their work was that simple formation models predicted similar fluid pressures relative to fully heterogeneous models. The methodology in this paper uses a three-level Box-Behnken that is better suited for developing response surfaces. This work focuses on developing response surfaces for overpressure and CO_2 plume area after injection since these are significant risk factors for surface leakage.

Response surface methodology uses a set of designed experiments to obtain an optimal result [30-31]. Response surfaces are an empirical fit of either simulated or experimental outcomes. The responses, or outcomes, are measured or computed for each factor combination specified by the experimental design. The polynomial proxy model is generated using stepwise linear regression methods. Every term in the polynomial is a function of one or more factors. The coefficients are indicative of the factor effects and interactions.

In this paper, an algebraic response surface equation is used to fit the outcomes (or responses) predicted from detailed reservoir simulations. These response surface outcome models are used in conjunction with a Monte Carlo random sample generator to develop probability density functions for various risk factors. This process significantly reduces the overall number of simulations required relative to direct Monte Carlo simulations. First, the type of experimental design is chosen among Central Composite, Full Factorial or Box-Behnken design. The numerical experiments are then performed for each prescribed combination of parameters as determined by the chosen experimental design. A regression is used to determine the best-fit coefficients of the individual variables and their interactions, which are used to create the response surface. The response surfaces generated are rigorously validated and PDFs of important outcomes like overpressure are generated.

2.3. Materials and Methods

2.3.1. Experimental Design

Experimental design requires a range of values for each factor. The ranges should include all feasible values scaled to a range between -1 and 1. Factor responses in complex physical problems, such as multiphase fluid flow, are usually nonlinear. Quadratic linear models should be used whenever possible to obtain the best fit of response surface equations. In general, second order polynomial response surfaces [Equation 2.1] are sufficient to develop acceptable surrogate equation models in reservoir studies [32]. This can be achieved by using three-level factorial designs which assign each factor its minimum, center point, or maximum value [-1,0,1] in all possible combinations with other factors [33] [Figure 2.1a].

$$y = \beta_0 + \sum_{i=1}^{k} \beta_i X_i + \sum_{i<j} \sum^{k} \beta_{ij} X_i X_j + \sum_{i=1}^{k} \beta_{ii} X_i^2 + \varepsilon \qquad [2.1]$$

where y = dependent variable or response; β_0 = the intercept (global mean); β_i = main linear effects; β_{ii} = the quadratic (nonlinear) effects due to the ith variable; β_{ij} = the two-way linear interaction effects due to the ith and jth variables; X = value of input parameters; ε = regression error.

Box-Behnken experimental designs are spherical, rotatable, or nearly rotatable second-order designs. The method is based on a three-level incomplete factorial design, which consists of the midpoints (black dots) of the edges from a cube and the center point (red dots) [Figure 2.1b]. It can be considered as three interlocking 22 factorial designs along
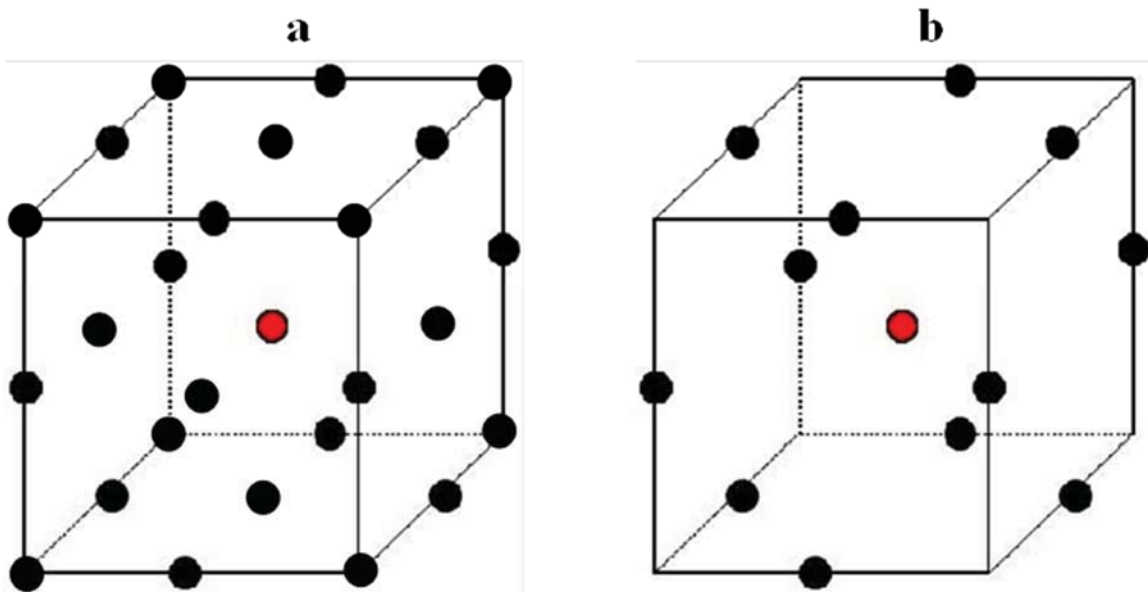
Figure 2.1: Examples of three input parameter designs. (a) Three-level factorial and (b) Box-Behnken design where each dot represents a simulation.

with a center point. Box- Behnken experimental designs do not combine all factors at the maximum and minimum levels. This design uses center point replicates, where all factors at midpoint values are repeated three times. These replicates make the design nearly orthogonal, thus improving the precision of the estimates of response surface coefficients.

The number of simulations required in full-factorial, three-level designs increases exponentially (3^k), where k is the number of factors. For six input parameters, a total of 729 simulations would be required to evaluate outcomes and develop response surfaces. In order to reduce the number of simulations required for large factor designs, modified three-level factorials, such as Box-Behnken experimental designs, may be used. For six input parameters there are 54 simulations required for the Box-Behnken design, however, six of those are base case (all parameters at midpoint values) replicates, reducing the total simulations to 49 [Table 2.1]. The tables use scaled rather than the true parameter values, with [-] as the low value, [0] as the midpoint value, and [+] as the high value. This

Table 2.1: Simulation table for a 6-factor Box-Behnken experimental design

Simulation Number	X_1	X_2	X_3	X_4	X_5	X_6
1	-	-	0	-	0	0
2	+	+	0	-	0	0
3	+	-	0	+	0	0
4	-	+	0	+	0	0
5	0	-	-	0	-	0
6	0	+	+	0	-	0
7	0	+	-	0	+	0
8	0	-	+	0	+	0
9	0	0	-	-	0	-
10	0	0	+	+	0	-
11	0	0	+	-	0	+
12	0	0	-	+	0	+
13	-	0	0	-	-	0
14	+	0	0	+	-	0
15	+	0	0	-	+	0
16	-	0	0	+	+	0
17	0	-	0	0	-	-
18	0	+	0	0	+	-
19	0	+	0	0	-	+
20	0	-	0	0	+	+
21	-	0	-	0	0	-
22	+	0	+	0	0	-
23	+	0	-	0	0	+
24	-	0	+	0	0	+
25	0	0	0	0	0	0
26	0	0	0	0	0	0
27	0	0	0	0	0	0
28	+	-	0	-	0	0
29	-	+	0	-	0	0
30	-	-	0	+	0	0
31	+	+	0	+	0	0
32	0	+	-	0	-	0
33	0	-	+	0	-	0
34	0	-	-	0	+	0
35	0	+	+	0	+	0
36	0	0	+	-	0	-
37	0	0	-	+	0	-
38	0	0	-	-	0	+
39	0	0	+	+	0	+
40	+	0	0	-	-	0
41	-	0	0	+	-	0
42	-	0	0	-	+	0
43	+	0	0	+	+	0
44	0	+	0	0	-	-
45	0	-	0	0	+	-
46	0	-	0	0	-	+
47	0	+	0	0	+	+
48	+	0	-	0	0	-
49	-	0	+	0	0	-
50	-	0	-	0	0	+
51	+	0	+	0	0	+
52	0	0	0	0	0	0
53	0	0	0	0	0	0
54	0	0	0	0	0	0

reduction of number of simulations leads to confounding or aliasing where the parameters may correlate with both the dependent and independent variables. It should also be emphasized that Box-Behnken designs are spherical, so the vertices of the cube (all inputs at extreme values) are not covered by the design, and prediction at these points is an extrapolation.

2.3.2. Independent Response Variables

A six-parameter Box-Behnken experimental design was developed for this study. The six parameters were formation thickness, formation depth, porosity, log_{10} permeability, brine density, and maximum residual CO_2 saturation. The ranges of values for the six selected parameters were chosen to be consistent with potential field observations [Table 2.2]. For each simulation, the real value shown in Table 2.1 is used that corresponds to the scaled values, and the outputs are recorded for the particular combination of parameters. Interaction between the parameters can also be determined by multiplying the scaled value of the individual parameters; a combination of [-1] for both X_1 and X_2 has a scaled value of [+1] for $X_1 \times X_2$.

Some points in the design may not be physically realistic. For example, it is unnecessary to consider scenarios with high permeability and low porosity, if porosity and permeability are positively correlated. It has been shown that in general there is correlation between porosity and permeability [34]. While there is positive correlation, there is generally large uncertainty in a fit of these data, where using a single relationship between porosity and permeability may not be prudent. Representations of heterogeneity at various scales have been discussed in a review paper [35]. Most of the geologic models were constructed in this paper by using spatially correlated properties in the forms of variograms. Even though

Table 2.2: Independent parameters varied during simulations

Independent Parameter	Variable	Low [-1]	Midpoint [0]	High [+1]
Formation Thickness [m]	X_1	40	80	120
Formation Depth [m]	X_2	1700	2000	2300
Porosity	X_3	0.1	0.2	0.3
Permeability [mD]	X_4	10	100	1000
Brine Density [kg/m^3]	X_5	1000	1150	1300
Maximum Residual CO_2	X_6	0.1	0.2	0.3

use of variograms would provide realistic spatially correlated models, generation of stochastic realizations would necessitate use of a different computational strategy for creating surrogate models and obtaining the PDFs. To properly model this uncertainty it would be necessary to incorporate the additional variables of these relationships, such as Kozeny-Carmen, which would increase the total number input variables replacing a single input, such as permeability, with multiple inputs, such as hydraulic radius, pore surface area, specific surface area or other variables of the selected relationship [35]. This large set of geological parameters will make it difficult to conduct a study that incorporates the range of reservoir and operational parameters used in this study due to the much larger number of simulations required. Instead, two sets of Monte Carlo simulations were performed in this study once the response factors were identified. The first was to sample uniformly over the entire range of the important parameter set and the other was to use a correlated porosity-permeability set. This is described more in detail when discussing PDF generation.

2.3.3. Simulation Physical Domain

For the sets of simulations, the model domain was chosen to be 45 km by 45 km with the formation thickness varying from 40 m to 120 m. A representative model with 40 m thickness is shown in Figure 2.2. The domain was discretized into 1000 m x 1000 m x 5 m grid-blocks. Additional refinement of 100 m x 100 m x 5 m was used for all grid-blocks that contained perforations of the CO_2 injection well.

One simulation set used a single injection well (fully penetrating the reservoir) with a constant mass injection rate of one million tons (Mt) per year of CO_2. The injection well is centered in the model domain. CO_2 was injected for a period of 25 years and the reservoir behavior was predicted for an additional 50 years after injection operations had ceased. The top, bottom and lateral boundaries are all considered no-flow for this simulation set.
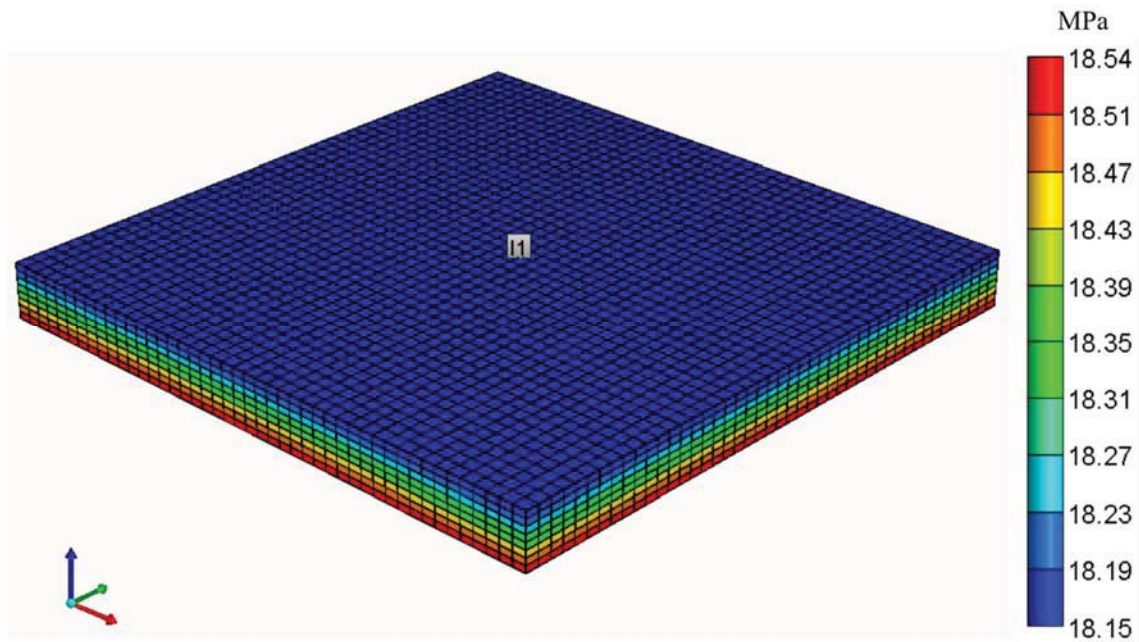
Figure 2.2: Simulation model domain displaying initial pressure condition

The reservoir was modeled without any dip to limit migration toward the boundaries. A second simulation set was developed using a fully penetrated injection well with a constant pressure injection scheme. The rock fracturing pressure threshold was calculated using a 15 kPa/m (0.66 psi/ft) fracture pressure gradient. The bottomhole injection pressure was designated to be 90 percent of the fracturing pressure. The injection well was also centered and all boundaries were considered no-flow for these simulations as well.

Boundary conditions will have an effect on both fluid pressure and the amount of CO_2 that can be injected. The choice of boundary conditions affects the potential risk factors and outcomes investigated here. If the reservoir is considered open or partially compartmentalized, there will be brine displacement caused by induced pressure gradients due to CO_2 injection rather than pressure buildup. Conversely, if the reservoir is fully compartmentalized the brine will not be displaced beyond the model boundaries and there will be a pressure increase due to CO_2 injection.

Previous work has shown that increased model complexity with various levels of heterogeneity in compartmentalized reservoirs will affect the quality of the simulated results [36]. For large-scale injection site appraisal, buildup or falloff tests to determine the boundary distance are generally not feasible due to large radius of influence requiring long testing periods [37]. Encountering open reservoirs are unlikely, even on the basin scale, unless the formation is open to the surface. This modeling assumes that there is no attenuation through the sealing layer, which can also affect the simulated outcomes [38].

2.3.4. Polynomial Response Surface Model

Since the experimental design matrix (Box-Behnken) contains more than one independent variable, a regression model to fit the data involves multiple linear regressions.

A stepwise regression method was utilized to uncover statistically significant coefficients based on p-values. Stepwise regression fits the least squares model in a sequential process, where at each step, only a single independent variable was either added to or removed from the model in the next fit. For these regressions, 0.05 and 0.1 were used, respectively, for maximum and minimum p-value criterion for addition and elimination of independent variables [39].

2.3.5. Monte Carlo Simulations

One application of response surfaces is probability density function (PDF) generation. Once the response surface coefficients are established, the distributions for parameters used in Monte Carlo simulations would normally be based on the site specific data. For each parameter that was varied in simulation, a random number was selected from a distribution of values for the chosen parameter. The distribution should be representative of the expected values in the region of interest. Two different types of PDFs were generated. One where a uniform distribution was sampled for all six parameters and the other where correlated porosity-permeability values were employed. The first method assumes that there was equal likelihood of the properties falling within the prescribed property ranges given in Table 2.2. The second method uses a sampling of porosity and permeability designed to eliminate low porosity – high permeability combinations and vice versa. The Monte Carlo simulations in each approach were subsequently repeated until convergence of the mean was achieved. It should be noted that these results are highly dependent on the chosen domain, operational parameters, and modeling assumptions.

2.3.6. Tools Utilized

All simulations were performed using Computer Modeling Group's Generalized Equation-of-State Model (CMG-GEM) Compositional reservoir simulator [40]. GEM is an equation of state (EOS) based compositional reservoir simulator for modeling the flow of three-phase, multi-component fluids. CMG-GEM have been used to model CO_2 sequestration in previous studies [37, 41-43].

Monte Carlo simulations were performed using Palisade's @RISK software, a spreadsheet based risk analysis tool [44]. This software performs risk analysis by compiling distributions of possible results by substituting a range of values—a probability distribution—for any factor that has inherent uncertainty. It then calculates results, each time using a different set of random values from the probability functions.

2.4.   Results

2.4.1. Quality of Regression

To validate the proxy model, the prediction of the linear polynomial response surface model was compared to the simulated data using the coefficient of determination (R^2) as a goodness-of-fit measure which indicates the overall accuracy of the regression. The calculated R^2 values close to one suggests that a model has a ratio of the sum of squares for the residuals relative to the sum of squares for the response near zero.

The Root Mean Square Error (RMSE) (also known as the root mean square deviation, RMSD), is used to measure the total residuals of the predicted and simulated values. The RMSE is defined as the square root of the mean squared error [Equation 2.2]:

$$RMSE = \sqrt{\frac{\sum_{i=1}^{n}\left(Y_{pred,i} - Y_{sim,i}\right)^2}{n}} \qquad [2.2]$$

where Y_{pred} = response surface outcome values and Y_{sim} = modeled output values from the simulator.

It is often difficult to analyze the error in terms of absolute values due to variation in the absolute values, ranges and units of the different outcomes. Non-dimensional forms of the RMSE are required to compare RMSE for different units and outcomes. The RMSE is normalized by dividing with the range of the observed data as follows [Equation 2.3]:

$$NRMSE = \frac{RMSE}{Y_{pred,max} - Y_{pred,min}} \qquad [2.3]$$

where $Y_{pred,max}$ = maximum value of the response surface predicted outcome, $Y_{pred,min}$ = minimum value of the response surface predicted outcome.

The NRMSE is often expressed in terms of percentage by multiplying by 100, where the smaller percentage values indicate higher accuracy in the predictability of the response surface data relative to the simulated outcomes.

Quality of regression plots are provided in Figures 2.3 and 2.4. The observed and predicted overpressure, the resulting increase above hydrostatic pressure due to CO_2 injection, was calculated at the upper boundary approximately 5 km from the injection well, immediately after CO_2 injection stopped (25 years) when the pressure is at a maximum [Figure 2.3a and 2.4a]. The average reservoir pressure increase, which is the increase above average hydrostatic pressure, was also calculated at the end of the injection
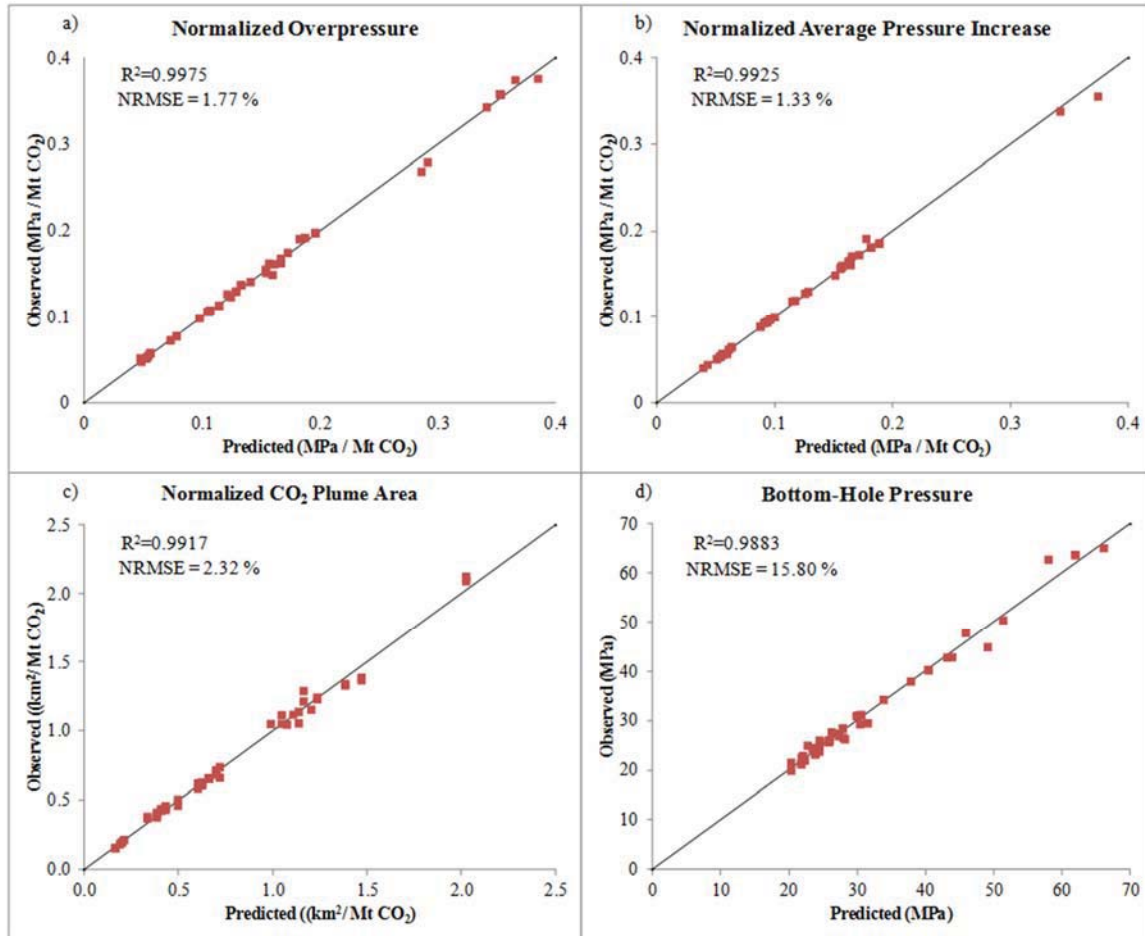
Figure 2.3: Constant mass injection response surface regression fits for (a) Normalized overpressure (b) Normalized average pressure increase (c) Normalized CO_2 plume area (d) Bottomhole pressure.

cycle [Figure 2.3b and 2.4b]. The areal extent of the CO_2 plume at the upper boundary was calculated after 75 years [Figure 2.3c and 2.4c]. Bottomhole pressure and cumulative CO_2 mass injected were calculated at the end of the injection period as well [Figure 2.3d and 2.4d]. All PDFs, with exception of cumulative CO_2 mass injected and bottomhole pressure, were normalized to the cumulative CO_2 mass injected for comparison between the two injection schemes. The high R^2 and low NRMSE values [Figures 2.3 and 2.4] indicate that were normalized to the cumulative CO_2 mass injected for comparison between the two
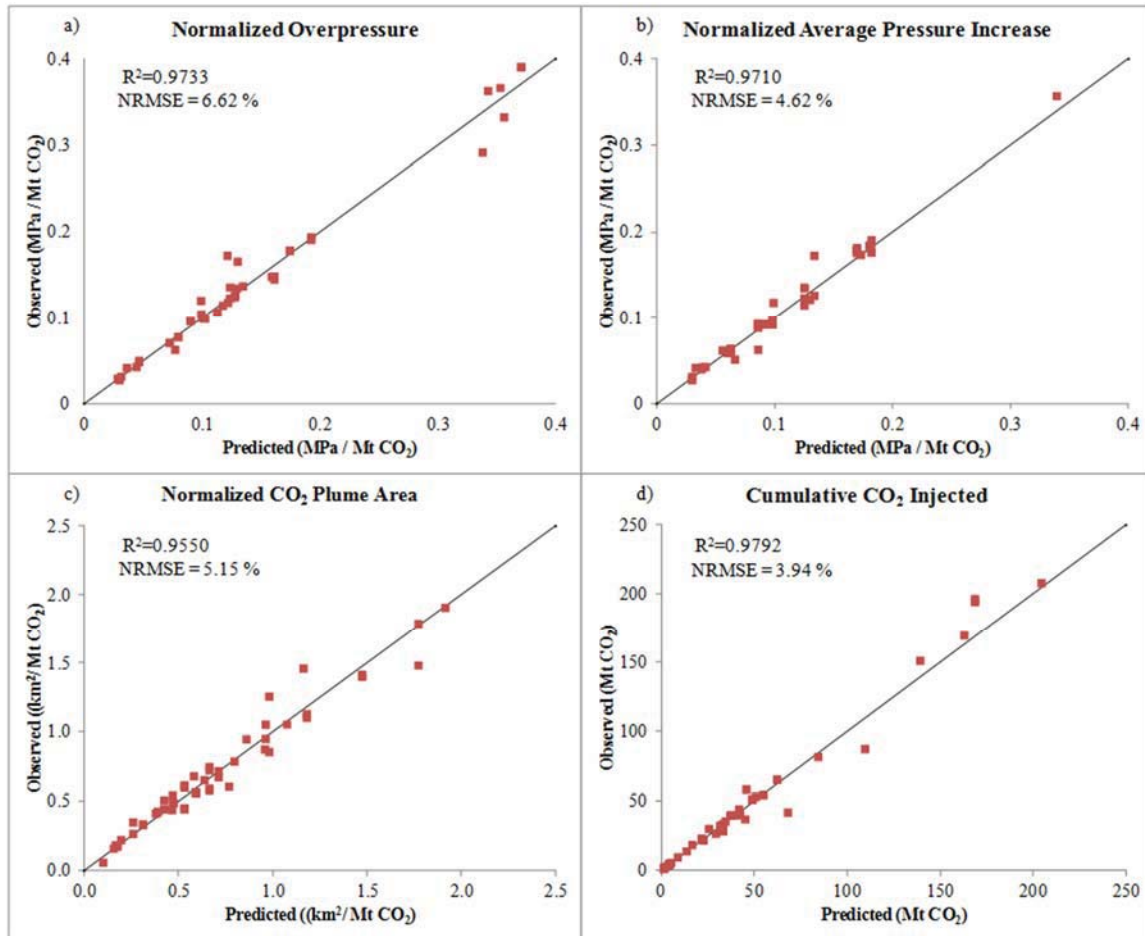
Figure 2.4: Constant pressure injection response surface regression fits for (a) Normalized overpressure (b) Normalized average pressure increase (c) Normalized CO_2 plume area (d) Cumulative CO_2 injected.

injection schemes. The high R^2 and low NRMSE values [Figures 2.3 and 2.4] indicate that the response surfaces fit the outcomes at the simulated values, and the models can be used with confidence to predict the outcomes for any of the input parameters within the given ranges.

2.4.2.   Response Surface Coefficients and Sensitivity Analysis

Stepwise regression analysis determines the values of the coefficients that cause the function to best fit the data. The log-transformed coefficients are included [Table 2.3] for all outcomes for both injection scenarios. The fitted response surface model was used to generate tornado diagrams [Figures 2.5 and 2.6] to visualize the parameter effect on the response. The summary ranking of input parameters [Table 2.4] shows that the most influential factors are porosity, permeability and formation thickness for all cases. There is not a strong dependency on brine density or depth for the chosen outcomes.

2.4.3.   Validation of the Response Surface Equations

Validation is needed to verify that the response surfaces generated are adequate proxy models for the reservoir simulators from which they were generated. A total of 100 randomized simulations were used for this validation. Each independent parameter's range was scaled from [-1] to [+1] and a value was selected randomly from a uniform distribution for all six parameters varied independently in the 100 simulations. Each simulated outcome was then plotted against the proxy model's expected outcome value for both constant pressure and constant mass injection well controls.

For random simulations for the constant mass injection, there is a reasonable match for the average reservoir pressure increase, overpressure 5 km from the injection well and

Table 2.3: Log-transformed regression coefficients for both constant mass injection and constant pressure injection scenarios

Coefficient	Constant Mass Injection				Constant Pressure Injection			
	Normalized Overpressure (MPa/Mt)	Normalized Avg Pressure Increase (MPa/Mt)	Normalized CO_2 Plume Area (km^2/Mt)	Bottom Hole Pressure (MPa)	Normalized Overpressure (MPa/Mt)	Normalized Avg Pressure Increase (MPa/Mt)	Normalized CO_2 Plume Area (km^2/Mt)	Cumulative CO_2 Mass Injected (Mt)
β_0	-16.06087036	-16.18245934	-7.320594814	10.15913922	-16.10773758	-16.20276685	-7.426935079	24.35114615
β_1	-0.532313487	-0.534401081	-0.15646478	-0.127275987	-0.619663386	-0.615453386	-0.295511042	0.594390471
β_2	-0.034423307	-0.019214543	-0.056540729	0.112635874	-0.0489709	0	-0.111246737	0.19200993
β_3	-0.457164851	-0.54491256	-0.581586474	-0.035350224	-0.439904898	-0.532493054	-0.664023337	0.21378079
β_4	-0.402986741	0	0.669597874	-0.349627577	-0.637792367	-0.24950278	0.553717538	1.716541329
β_5	0	0	0	0	0	0	0	0
β_6	-0.044266949	-0.044687779	0	0.05613656	-0.063398534	-0.066987809	0	-0.312524473
$\beta_1\beta_2$	0	0	0	0	0	0	0	0
$\beta_1\beta_3$	0	0	-0.039470849	0	0	0	0	0
$\beta_1\beta_4$	-0.027998677	-0.024903006	0.197760373	0.085950122	-0.088990266	-0.097379865	0.145698407	0.101849966
$\beta_1\beta_5$	0	0	0	0	0	0	0	0
$\beta_1\beta_6$	0	0	0	0	0	0	0	0
$\beta_2\beta_3$	0	0	0	0	0	0	0	0
$\beta_2\beta_4$	0	-0.024420621	0	0.047232283	0	0	0	0
$\beta_2\beta_5$	0	0	0	0	0	0	0	0
$\beta_2\beta_6$	0	0	0	0	0	0	0	0
$\beta_3\beta_4$	-0.147265738	0	0.064029417	-0.057767075	0	0	0.207724418	0.222102187
$\beta_3\beta_5$	0	0	0	0	0	0	0	0
$\beta_3\beta_6$	0	0	0	0	0.063259447	0.053065033	0	0
$\beta_4\beta_5$	0	0	0	0	0	0	0	0
$\beta_4\beta_6$	-0.035159849	-0.035477517	0	0	-0.100441688	-0.100053943	0.249379098	0.11439031
$\beta_5\beta_6$	0	0	0	0	0	0	0	0
β_1^2	0.132751453	0.12403907	0	0.052287585	0.13204959	0.12652878	0	-0.169737021
β_2^2	0	0	0	0	0	0	0	0
β_3^2	0.124985774	0.135760837	0.100380653	0	0.156704764	0.151758202	0.132465674	-0.142430641
β_4^2	0.16581195	-0.121593743	-0.168464965	0.259480786	0	-0.27987349	-0.222218048	-0.742124065
β_5^2	0	0	0	0	0	0	0	0
β_6^2	0	0	0	0	0	0	0	0

Figure 2.5: Tornado plots for constant mass injection responses for (a) Normalized overpressure (b) Normalized average pressure increase (c) Normalized CO_2 plume area (d) Bottomhole pressure.

Figure 2.6: Tornado plots for constant pressure injection responses for (a) Normalized overpressure (b) Normalized average pressure increase (c) Normalized CO_2 plume area (d) Cumulative CO_2 injected.

Table 2.4: Parameter rank for changes to output mean for constant mass injection and constant pressure injection scenarios

	Constant Mass Injection				Constant Pressure Injection			
Rank	Normalized Overpressure (MPa/Mt)	Normalized Avg Pressure Increase (MPa/Mt)	Normalized CO_2 Plume Area (km²/Mt)	Bottom Hole Pressure (MPa)	Normalized Overpressure (MPa/Mt)	Normalized Avg Pressure Increase (MPa/Mt)	Normalized CO_2 Plume Area (km²/Mt)	Cumulative CO_2 Mass Injected (Mt)
1	Formation Thickness	Porosity	Permeability	Permeability	Formation Thickness	Formation Thickness	Porosity	Permeability
2	Porosity	Formation Thickness	Porosity	Formation Thickness	Permeability	Porosity	Permeability	Formation Thickness
3	Permeability	Permeability	Formation Thickness	Depth to Saline Aquifer	Porosity	Permeability	Formation Thickness	Porosity
4	Residual Saturation	Residual Saturation	Depth to Saline Aquifer	Residual Saturation	Residual Saturation	Residual Saturation	Depth to Saline Aquifer	Residual Saturation
5	Depth to Saline Aquifer	Depth to Saline Aquifer	Brine Density	Porosity	Depth to Saline Aquifer	Brine Density	Residual Saturation	Depth to Saline Aquifer
6	Brine Density	Brine Density	Residual Saturation	Brine Density	Brine Density	Depth to Saline Aquifer	Brine Density	Brine Density

normalized area of review [Figure 2.7]. The average reservoir pressure, as well as the overpressure, plot shows a nearly linear correlation with an R^2 value of 0.978 and 0.97, respectively. These two pressure results, average pressure increase and overpressure, indicate the response surface equations, given their NRMSE of 3.18 and 3.66 percent, respectively, should be suitable proxies. The normalized area of review of the CO_2 plume has an R^2 value of 0.983 and NRMSE of 2.80 percent. This shows that areal extent could be estimated confidently for constant mass injection cases. The validation cross-plot for bottomhole pressure shows that there is less reliability between the response surface equation and the simulated result with an R^2 value of 0.756 and NRMSE of 20.61 percent. For the validation of constant pressure injection scheme, there is a reasonable match for the overpressure 5 km from the injection well with an R^2 value of 0.959 and NRMSE of 3.33 percent [Figure 2.8]. The average reservoir pressure increase shows high correlation with an R^2 value of 0.947 and NRMSE of 4.05 percent. The normalized area of review of the CO_2 plume has an R^2 value of 0.81 and NRMSE of 8.48 percent which indicates there is more error in the prediction. The validation cross-plot for cumulative CO_2 mass injected
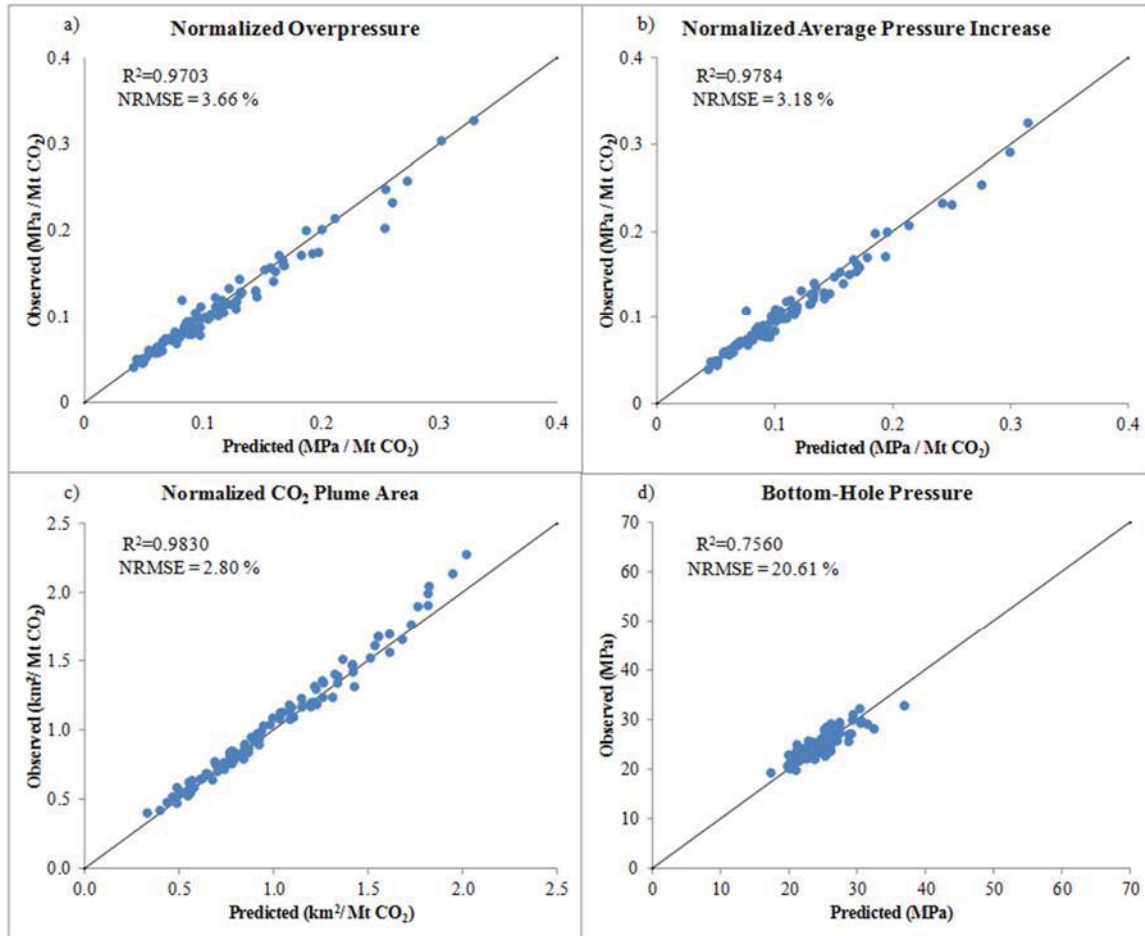
Figure 2.7: Constant mass injection randomized simulations validation plots for (a) Normalized overpressure (b) Normalized average pressure increase (c) Normalized CO_2 plume area (d) Bottomhole pressure.

indicates less correlation between the response surface equation and the simulated result with an R^2 value of 0.788 and NRMSE of 11.15 percent.

2.4.4. PDF Determinations

Once the response surface equations for each outcome had been determined and the parameter distributions selected, Monte Carlo simulations were performed to determine the PDFs. These Monte Carlo simulations were repeated until convergence of the mean and standard deviation was achieved. A set of Monte Carlo simulations was performed to
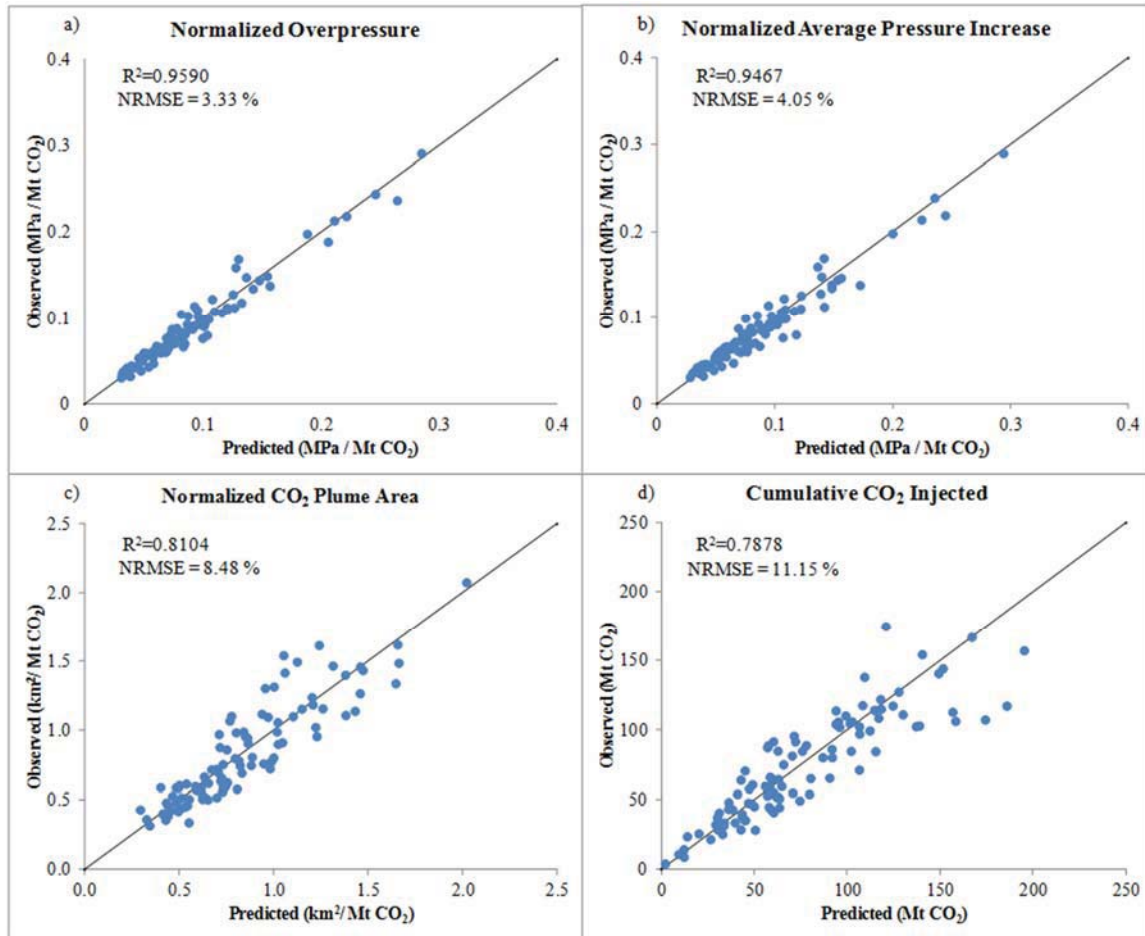
Figure 2.8: Constant pressure injection randomized simulations validation plots for (a) Normalized overpressure (b) Normalized average pressure increase (c) Normalized CO_2 plume area (d) Cumulative CO_2 injected.

investigate the effects of positive correlation between porosity and permeability in the parameter space. It is common to use correlated parameters within the experimental design matrix which may improperly limit the uncertainty in correlated parameters. Two different types of PDFs were generated – one where the entire ranges of porosity and permeabilities were sampled, and the other by using correlated porosity-permeability. The procedure for using the correlated porosity-permeability is described below. Three sets of simulations were performed combining a scaled high-permeability range [0,1] with a scaled high-porosity range [0,1], a low-permeability range [-1,0] with a low-porosity range [-1,0] as

well as a range that incorporates the middle range of permeability [-0.5,0.5] and middle

range of porosity [-0.5,0.5] [Figure 2.9]. The resulting PDFs were then combined into a

single output PDF to allow for comparison with the full parameter space sampling method.

This sampling method still allows for uncertainty in the porosity and permeability sampling

inputs while still providing the desired positive correlation.

2.4.4.1. Constant Mass Injection Process Model

Figures 2.10 – 2.13 provide PDFs for the constant mass injection model. In each of the

figures, (a) shows the PDF generated when sampling porosity-permeability over the entire

range, independently. Panel (b) in each of the figures was obtained by using the correlated

porosity-permeability Monte Carlo approach described above.

For the constant-mass-injection scenario, the average reservoir pressure increase
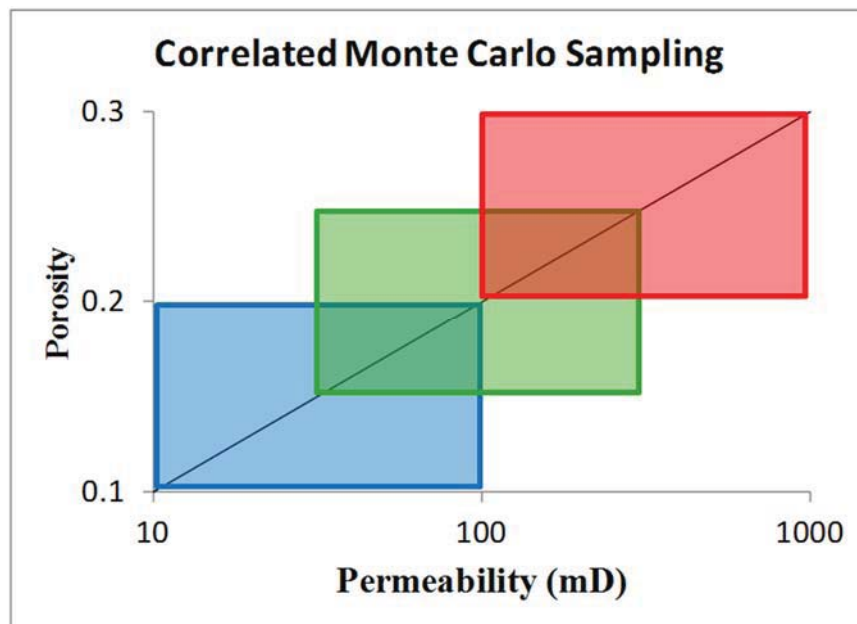
Figure 2.9: Porosity-permeability sampling bins used in creating probability density functions (PDFs) with correlated porosity-permeability distributions.
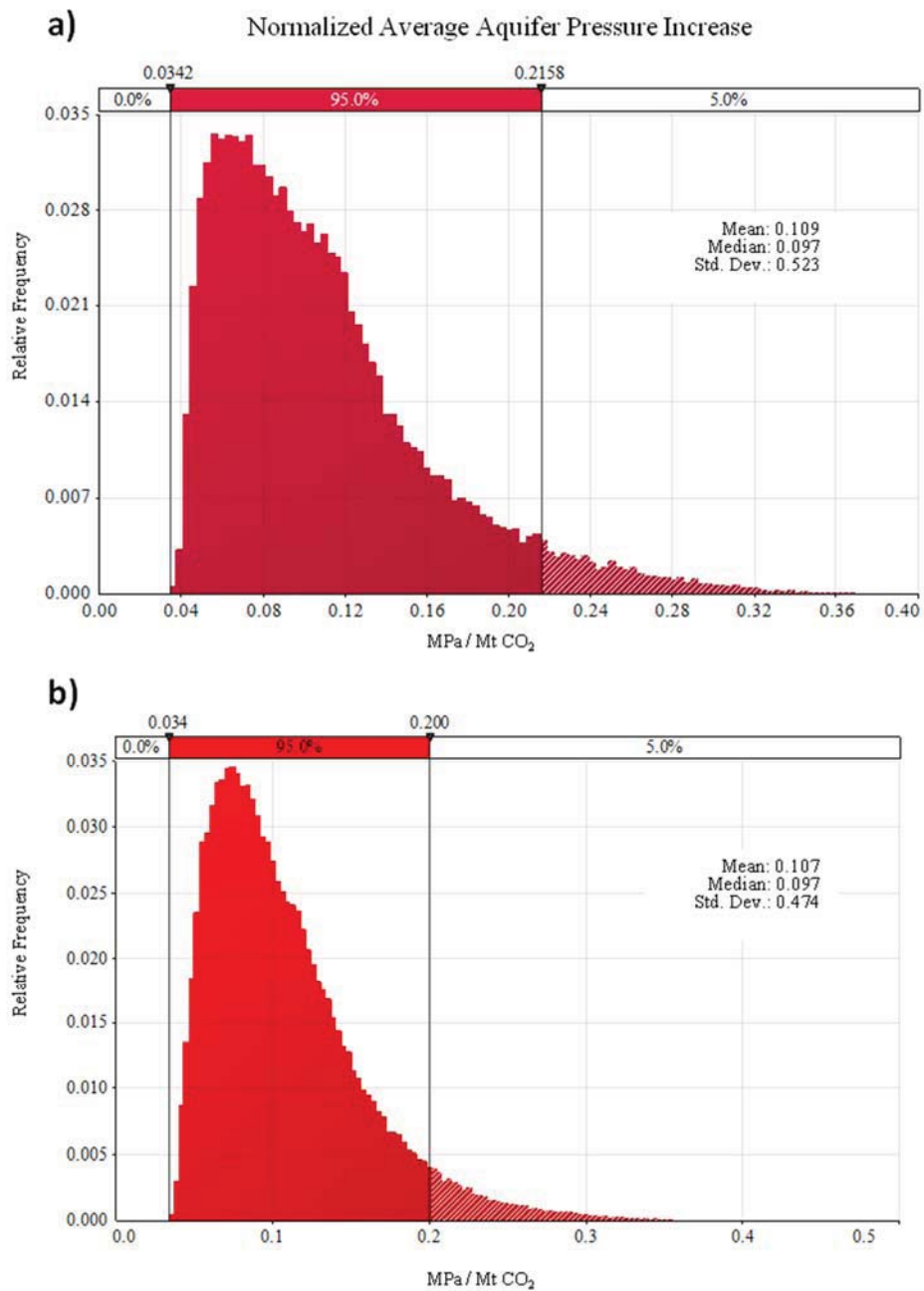
Figure 2.10: Constant mass injection normalized average pressure increase. (a) PDF created by sampling uniformly across distributions of all of the important parameters. (b) PDF created using correlated porosity-permeability values shown in Figure 2.9.
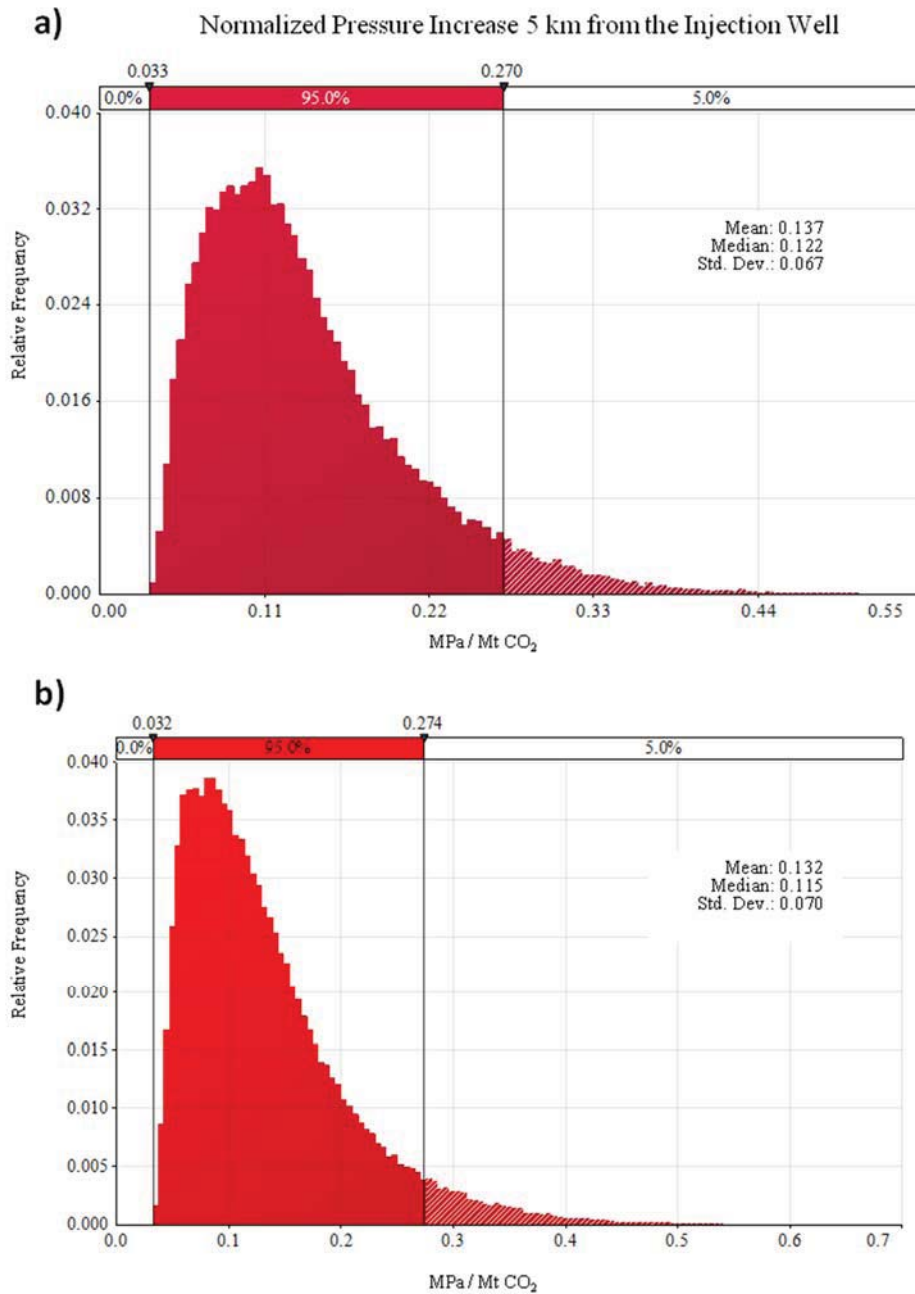
Figure 2.11: Constant mass injection normalized overpressure 5 km from the injection well. (a) PDF created by sampling uniformly across distributions of all of the important parameters. (b) PDF created using correlated porosity-permeability values shown in Figure 2.9.
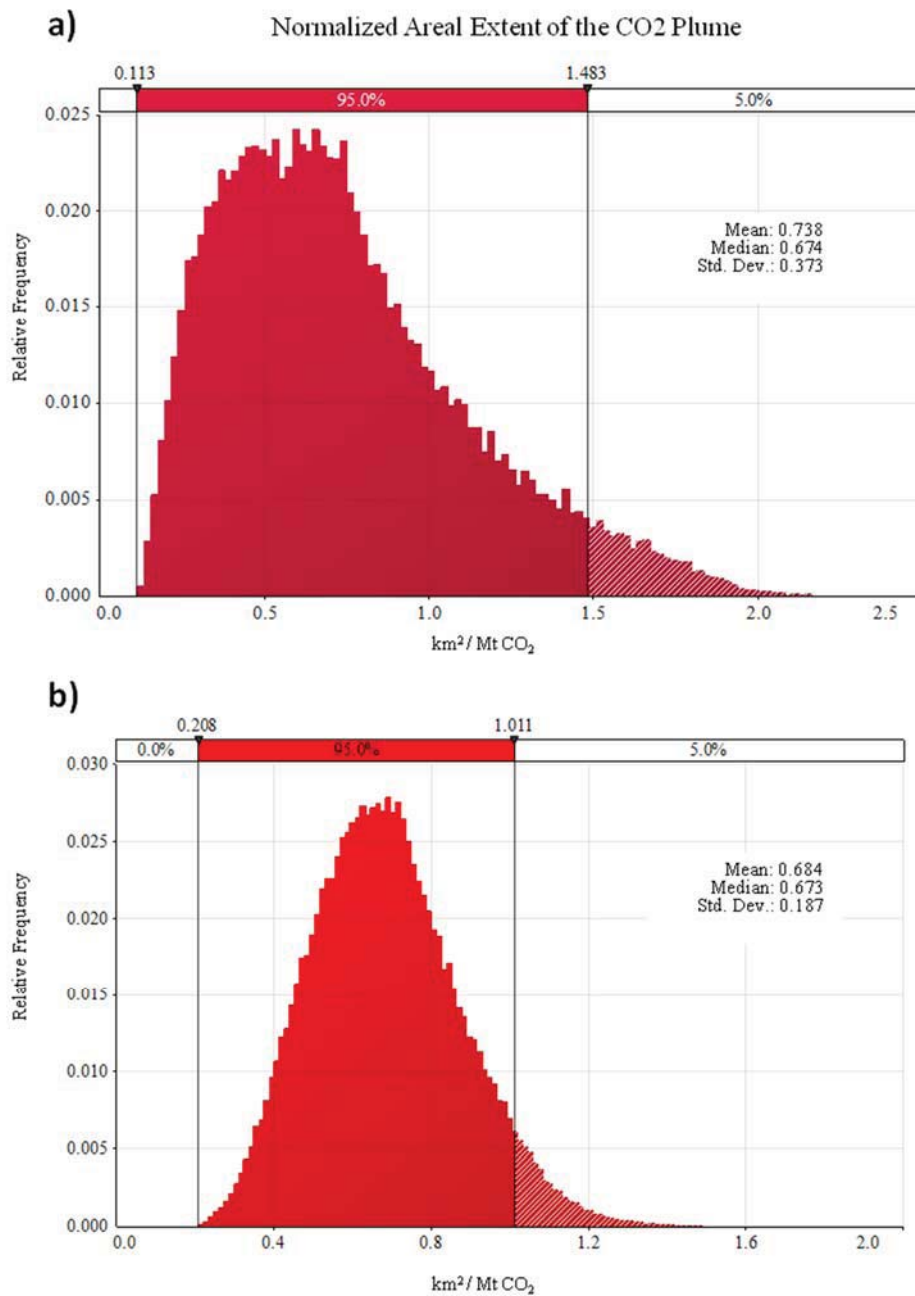
Figure 2.12: Constant mass injection normalized areal extent of the CO_2 plume. (a) PDF created by sampling uniformly across distributions of all of the important parameters. (b) PDF created using correlated porosity-permeability values shown in Figure 2.9.
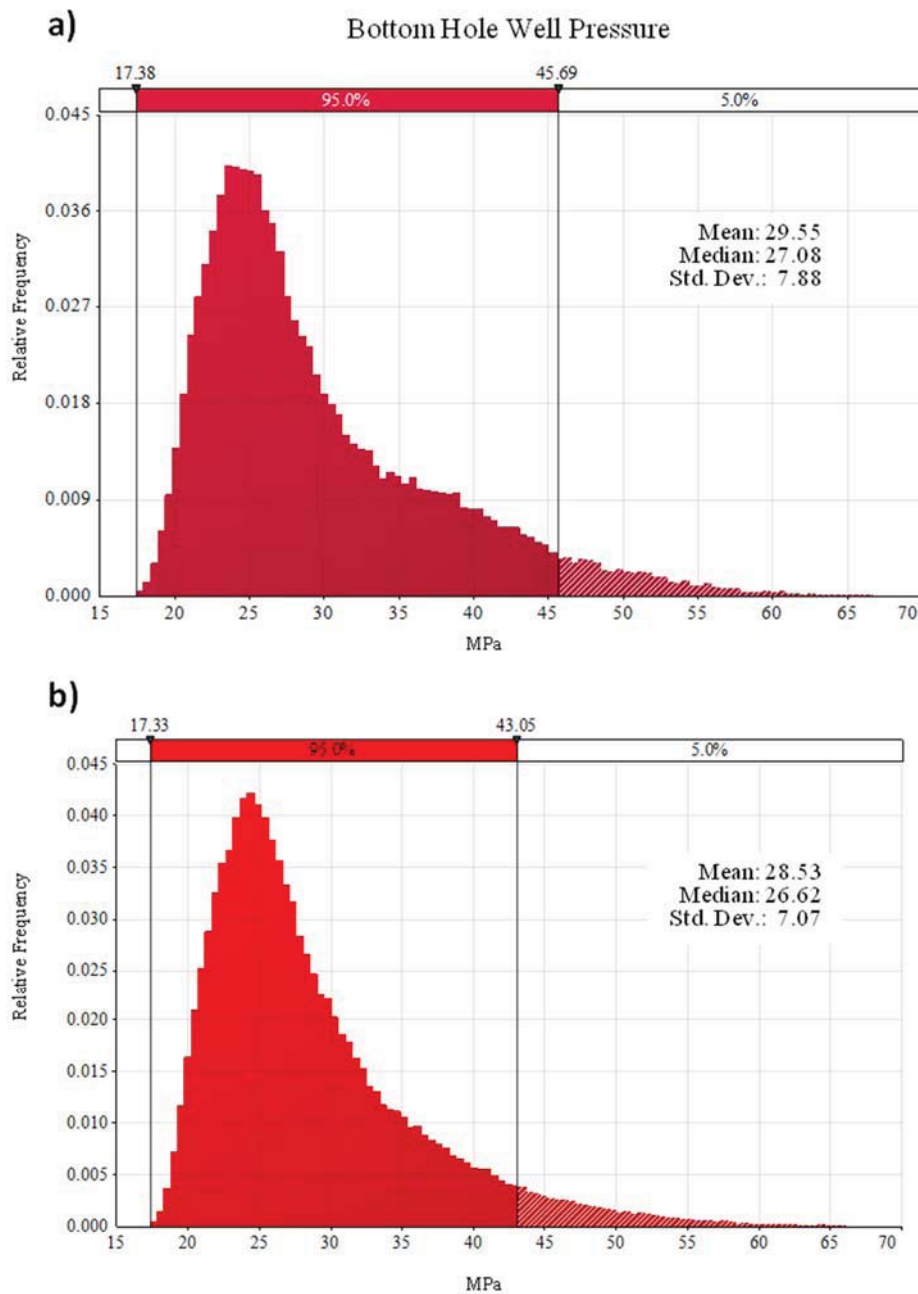
Figure 2.13: Constant mass injection well bottomhole pressure. (a) PDF created by sampling uniformly across distributions of all of the important parameters. (b) PDF created using correlated porosity-permeability values shown in Figure 2.9.

should not exceed 0.216 MPa per Mt injected to 95 percent confidence, assuming uniform distributions over the ranges for each of the six parameters as identified in Table 2.1 [Figure 2.10a]. This average reservoir pressure increase reduces to 0.2 when the correlated porosity-permeability approach is used [Figure 2.10b]. The overpressure 5 km from the injection well should not exceed about 0.270 MPa per Mt injected to 95 percent confidence [Figure 2.11a] and changes only slightly for the correlated simulations [Figure 2.11b]. With 95 percent confidence, the plume area should not occupy more than 1.48 km^2 per Mt of CO_2 injected [Figure 2.12a]. By eliminating low-porosity, high-permeability, and high-porosity-low-permeability combinations, the correlated PDF for area spread for 95 percent confidence decreases to 1.01 km^2 per Mt CO_2 injected [Figure 2.12b]. For the constant mass injection, where all outcomes are normalized to 25 Mt, this equates to 37.0 km^2 (approximately, 1.8 percent of the total areal extent of the reservoir) for uncorrelated and 25 km^2 for correlated simulations.

The bottomhole pressure for the constant mass injection scenario was an additional outcome that was generated. These distributions [Figures 2.13a and 2.13b] have a log normal distribution with a mean value of about 29 MPa. Porosity-permeability correlation based simulations are not significantly different for this outcome.

2.4.4.2. Constant Pressure Injection Process Model

PDFs for constant pressure injection for the two types of Monte Carlo simulations are shown in Figures 2.14 – 2.17. The uncorrelated porosity-permeability PDFs are in the (a) panel and the correlated ones are in the (b) panel. The average pressure increase, when the injection rate is not limited, would not exceed about 0.22 MPa per Mt injected to 95 percent confidence, assuming uniform distributions over the ranges for each of the six parameters
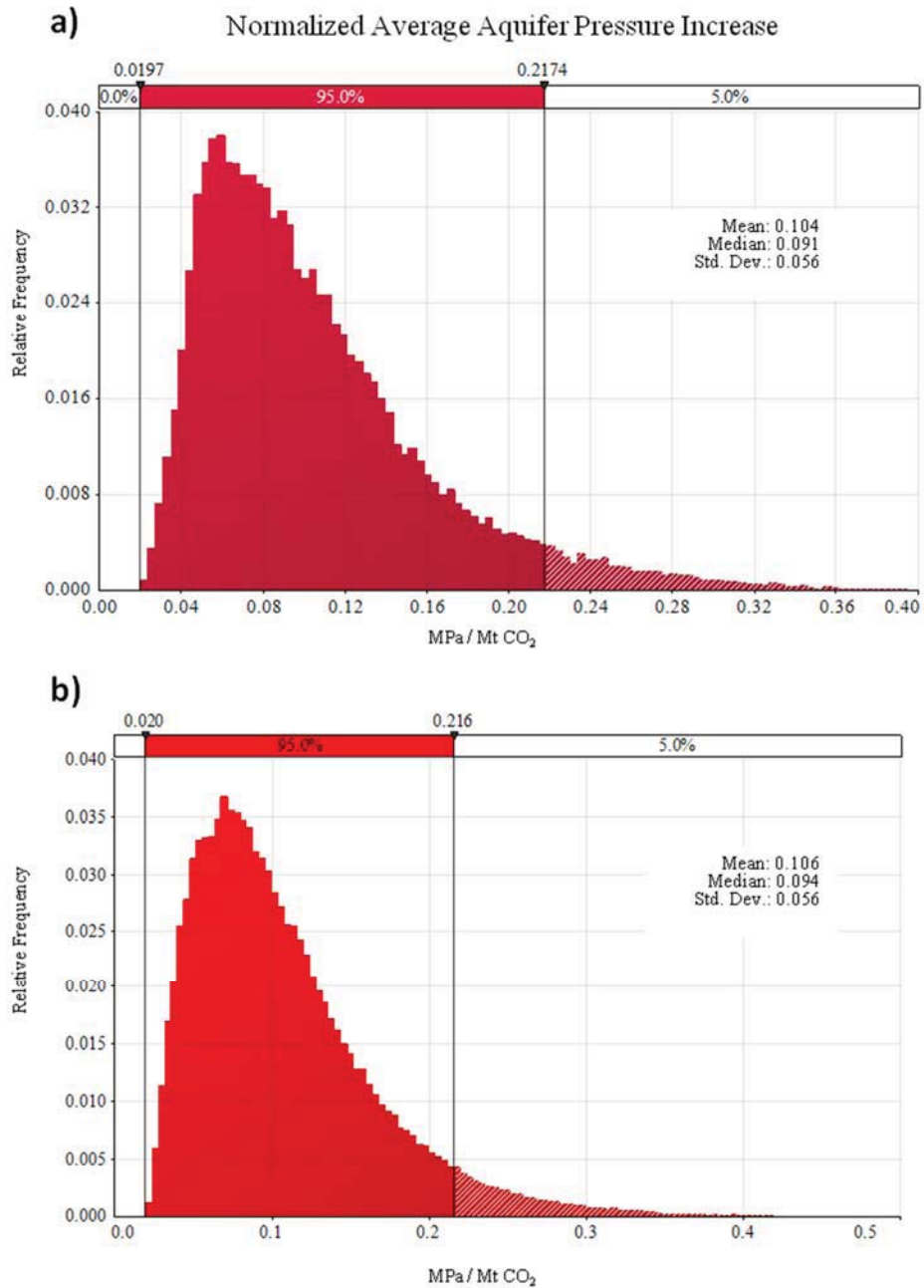
Figure 2.14: Constant pressure injection normalized average pressure increase. (a) PDF created by sampling uniformly across distributions of all of the important parameters. (b) PDF created using correlated porosity-permeability values shown in Figure 2.9.
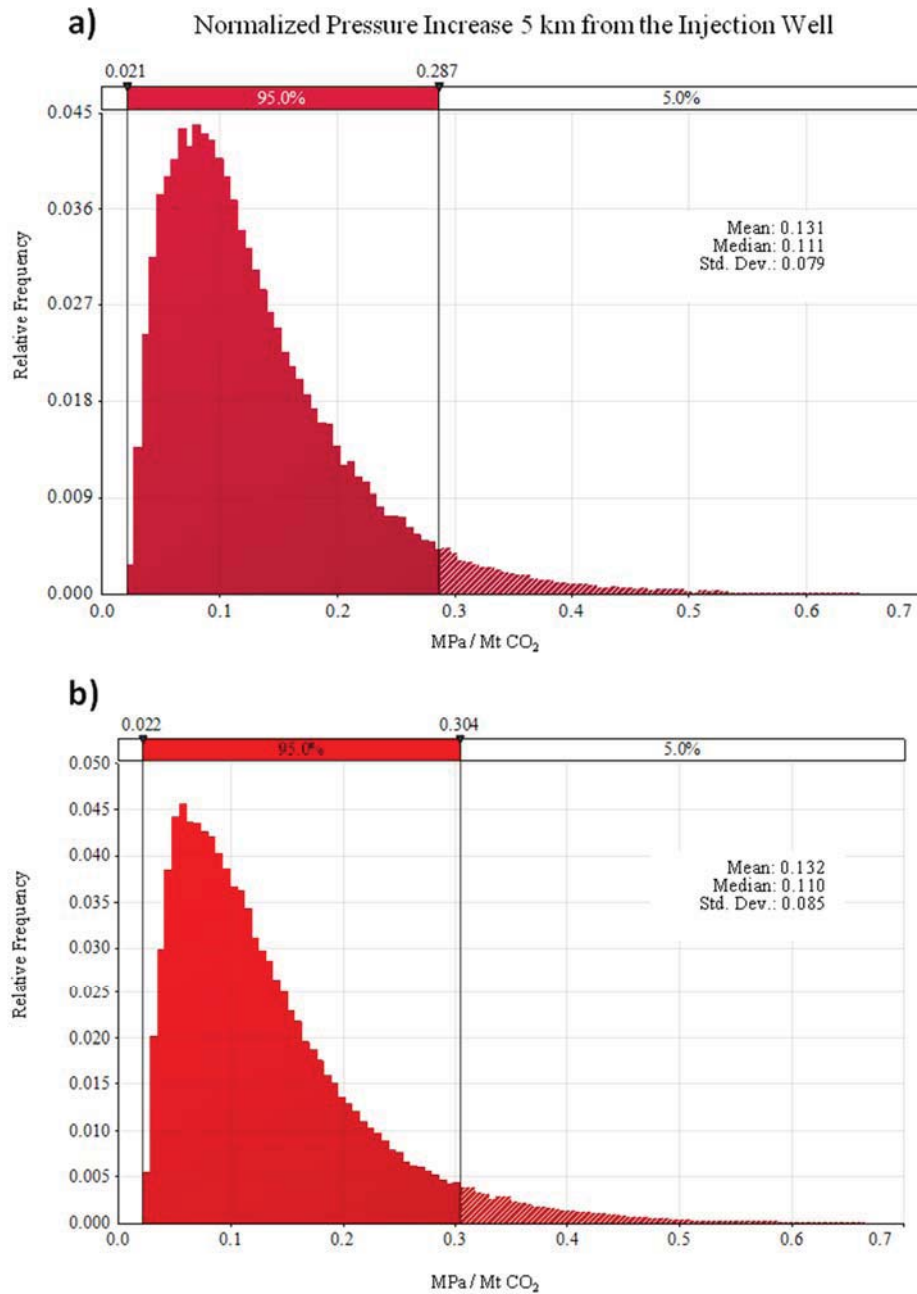
Figure 2.15: Constant pressure injection normalized overpressure 5 km from the injection well. (a) PDF created by sampling uniformly across distributions of all of the important parameters. (b) PDF created using correlated porosity-permeability values shown in Figure 2.9.
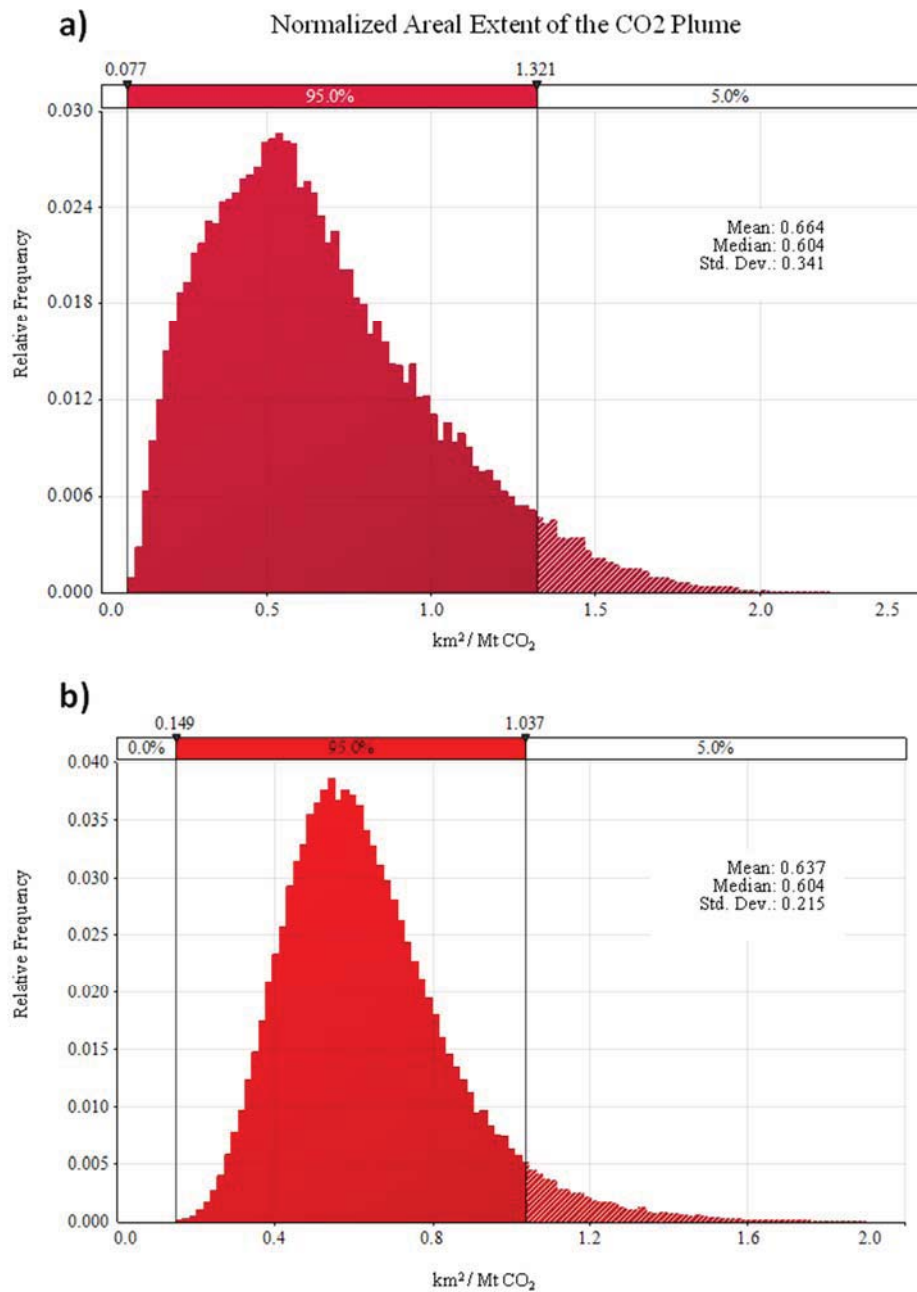
Figure 2.16: Constant pressure injection normalized areal extent of the CO_2 plume. (a) PDF created by sampling uniformly across distributions of all of the important parameters. (b) PDF created using correlated porosity-permeability values shown in Figure 2.9.
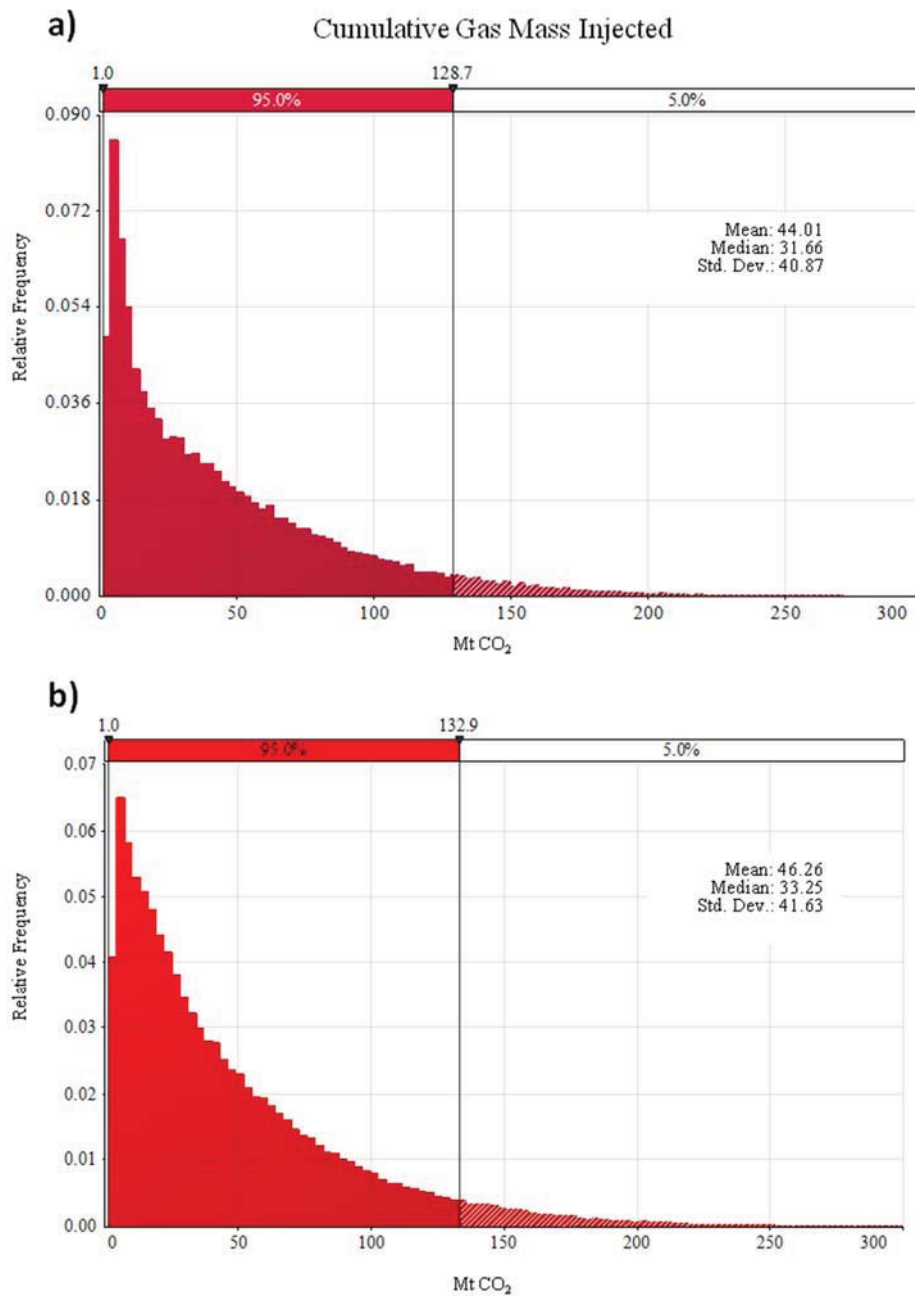
Figure 2.17: Constant pressure injection cumulative gas mass injected. (a) PDF created by sampling uniformly across distributions of all of the important parameters. (b) PDF created using correlated porosity-permeability values shown in Figure 2.9.

as identified in Table 2.1 [Figure 2.14a]. Use of correlated porosity-permeabilities in the Monte Carlo simulations does not change this outcome [Figure 2.14b]. Similarly, the overpressure 5 km from the injection well will not exceed about 0.3 MPa per Mt injected to 95 percent confidence [Figure 2.15a and 2.15b]. With 95 percent confidence, that the areal plume will not occupy more than 1.32 km^2 per Mt of injected CO_2 [Figure 2.16a] for uncorrelated simulations and 1.03 km^2 per Mt of injected CO_2 [Figure 2.16b] for correlated simulations. The spread becomes narrower as low-porosity, high-permeability and high-porosity-low-permeability combinations are eliminated.

The cumulative mass injected for the constant pressure injection simulations was an additional outcome that was investigated. These distributions [Figure 2.17a and 2.17b] exhibit exponential declines with a mean value of about 45 Mt of CO_2 in both types of PDFs. There is 95 percent confidence that the total mass injected will be less than about 130 Mt of CO_2 for the parameters used in these simulations. A summary of probability statistics are included [Table 2.5], showing the P10, P50, P90, and mean values for all constant mass and constant pressure injection uncorrelated PDFs.

2.5.   Discussion

In general all PDFs can be fit to a lognormal distribution. This is likely due to the logarithmic permeability distribution in the experimental design and the high effect of permeability on the outcomes. A secondary pressure limiting injection constraint was not used in the constant mass injection simulations in order to maintain an equal injection mass for all cases. This results in a pressure rise above the fracture pressure criterion in some cases. An example of the typical pressure curves for cases with identical geologic properties are shown in [Figure 2.18], where the pressure rise is limited in the constant

Table 2.5: Statistical summary for the constant mass and constant pressure injection scenarios.

	Constant Mass Injection					Constant Pressure Injection				
	Average Pressure Increase (MPa/Mt)	Over-pressure (MPa/Mt)	Uncorrelated Areal Extent of CO2 Plume (km²/Mt)	Correlated Areal Extent of CO2 Plume (km²/Mt)	Bottom-hole Pressure (MPa)	Average Pressure Increase (MPa/Mt)	Over-pressure (MPa/Mt)	Uncorrelated Areal Extent of CO2 Plume (km²/Mt)	Correlated Areal Extent of CO2 Plume (km²/Mt)	Cumulative Gas Mass Injected (Mt)
P10	0.054	0.064	0.31	0.45	21.75	0.048	0.051	0.268	0.396	5.24
P50	0.097	0.122	0.674	0.673	27.08	0.091	0.111	0.604	0.604	31.66
P90	0.182	0.23	1.28	0.934	41.24	0.18	0.236	1.147	0.916	102.1
Mean	0.109	0.137	0.738	0.684	29.55	0.104	0.131	0.664	0.637	44.01
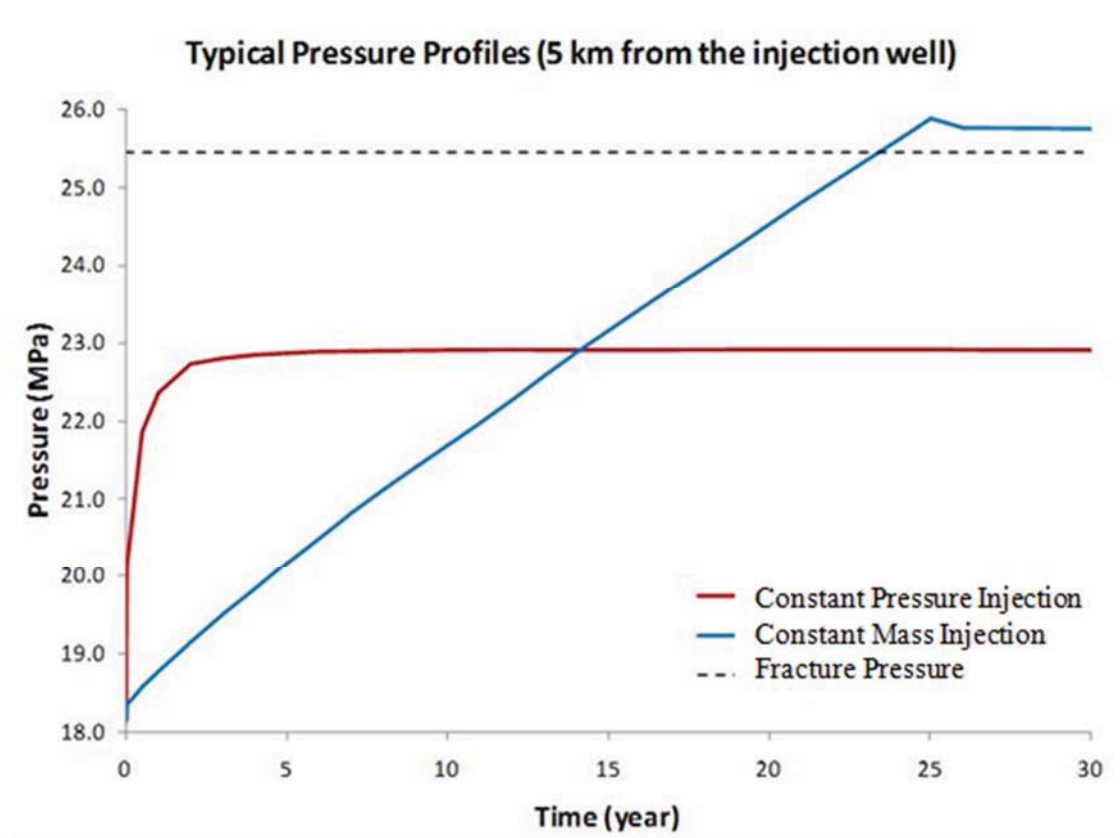
Figure 2.18: Typical pressure profiles for constant mass and pressure injection simulations

bottomhole pressure case but rises uninhibited for the constant mass. It was also observed that the constant-pressure injection resulted in a higher mean amount of CO_2 injected (44 Mt, according to Figure 2.12, in comparison to 25 Mt injected in the constant mass injection case). With the reduced risk of overpressure near the well, constant pressure injection is a better operational choice for CO_2 injection. This is not intuitively obvious while considering operational choices, and was one of the significant outcomes of this study. The conical shape of the CO_2 plume was not considered in these results. The areal extent focuses on the exposure to possible leakage pathways such as abandoned wells or induced fractures in the sealing layer. This value may be reduced by the choice of boundary condition and should be investigated further.

Ideally, input parameters and responses should be related linearly [15], however, this is rarely experienced in practice. Response models are difficult to use for time-varying responses. The injection rate is linear for the constant mass injection scenarios, whereas it is distinctly nonlinear for constant pressure injection scenarios [Figure 2.19]. It is also possible for an injection well to be shut-in completely for a period of time in the constant pressure injection cases, which can cause parameters to become discontinuous. This is likely the cause of the decrease in goodness of fit for constant pressure injection relative to constant mass injection.

A single injection well was used for simplification of the process model and represents an ideal situation, however, the large volumes injected in these simulations would likely be spread across multiple wells in practice. Typical profiles for bottomhole fluid rates of the constant pressure injection simulations for high and low permeability cases are included [Figure 2.19]. This indicates that for the high permeability case that the bulk of the CO_2 is injected in the first few years while for the low permeability cases the injection rate is
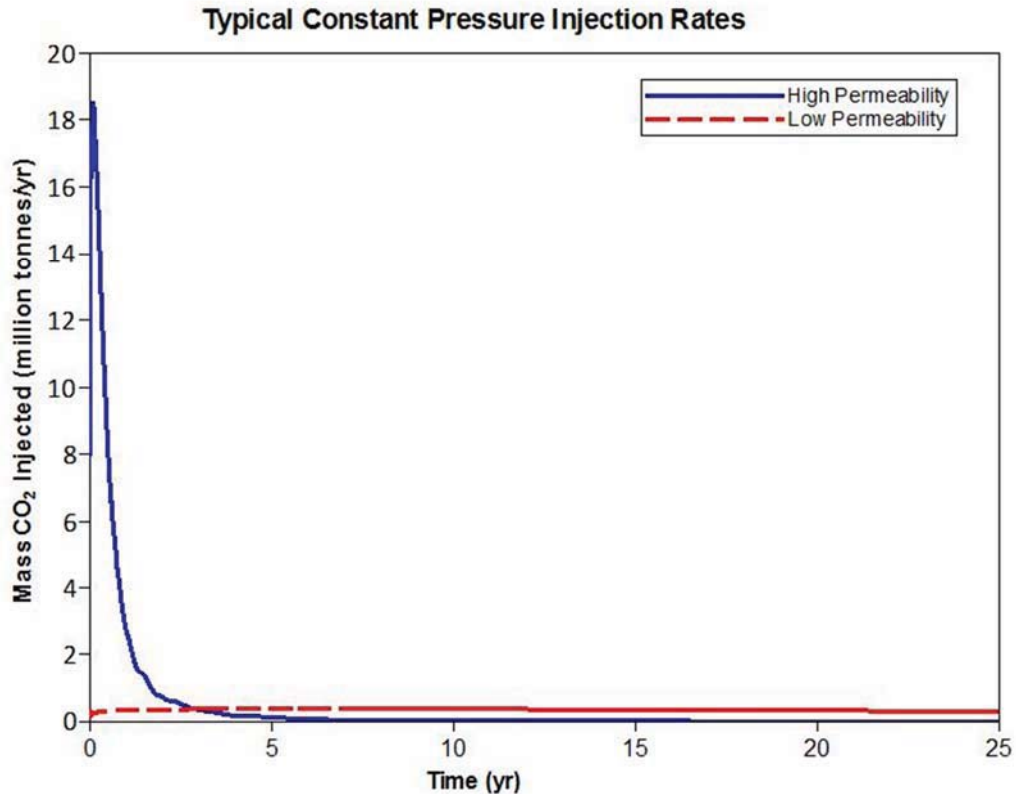
Figure 2.19: Typical injection rate profiles for high and low permeability constant pressure injection simulations

considerably lower but nearly constant throughout injection.

The distribution of permeability in a reservoir is dependent on the depositional environment. It has been shown for alluvial fan deposits [45] and fluvial or channelized deposits [46-47] that multimodal log permeability distributions may exist. These multimodal distributions are created when low energy deposits, such as flood plains, are nearby high energy deposits, such as streams or rivers. Conversely large erg deposits, similar to the Navajo sandstone formation in the San Juan basin display a relatively homogenous depositional environment in relation to fluvial or river deposits. It is recognized that all reservoirs are heterogeneous, but the level of heterogeneity varies. The choice of permeability distribution should be dictated by the potential sequestration site of interest.

Most deep saline aquifers are not extensively characterized and therefore CO_2 modeling assumptions require a simplification of the model domain. Without detailed site- specific data, one of the simplified assumptions is homogeneous permeability. It is therefore nearly impossible to model correlated heterogeneous permeability. An investigation of randomly populated heterogeneous domains was investigated to evaluate the errors imposed on the chosen outcomes. For these cases it was assumed that all values were at the base case values, where the mean of the log permeability field was its midpoint value of 100 mD. The permeability distributions were truncated at 10 and 1000 md, the extreme values. The standard deviation was varied from 10 (nearly normal distribution), 50, 100 and 500 (highly skewed). These results showed that there was not significant error in the homogeneous assumption except for the highly skewed distribution in the CO_2 plume area and cumulative mass injected outcomes [Table 2.6].

In general the set of response surface equations prove to be a good proxy for the normalized average pressure increase, normalized pressure increase away from the injection well, and normalized areal extent of the plume for both types of operations – constant mass and constant pressure injection.

2.6.   Conclusions

A general methodology was developed to determine probability density functions of possible risk factors in CO_2 sequestration. The method described can be used for any set of independent variables and risk factors that are deemed critical for a particular sequestration site. The injection operation can be performed by establishing a constant injection pressure (with varying injection mass) or by maintaining a constant mass injection rate (the injection pressure would have to change with time to accommodate this). This

Table 2.6: Percent error for random permeability fields with base case input parameters

Permeability Model	Constant Mass Injection				Constant Pressure Injection			
	Normalized Overpressure	Normalized Avg Pressure Increase	Normalized CO_2 Plume Area	Bottom Hole Pressure	Normalized Overpressure	Normalized Avg Pressure Increase	Normalized CO_2 Plume Area	Cumulative CO_2 Mass Injected
Homogeneous	0.4	0.2	0.9	0.5	1.0	0.1	5.9	4.6
Sigma 10	0.1	0.2	1.5	0.2	0.1	0.0	1.2	1.9
Sigma 50	0.7	0.6	2.6	0.5	1.4	0.3	0.9	5.3
Sigma 100	2.6	0.4	14.6	1.3	4.0	0.5	9.9	12.6
Sigma 500	5.8	2.7	22.0	2.7	7.8	0.4	12.1	59.9

methodology can be applied to any site where there is uncertainty in the reservoir parameters. The input parameter ranges can be modified to match those expected in a particular region. These new parameters can then be used to generate unique response surface equations using the appropriate experiment design matrix. It is also possible to use the response surfaces generated in this research for cases where only one parameter is known with a high degree of certainty, such as reservoir depth. The Monte Carlo simulations can then be repeated using the response surface equations, but rather than assigning a distribution with uncertainty for reservoir depth, a constant value can be used. In this work, two types of PDFs were generated – one by sampling uniformly over the entire parameter range and the other by using a correlated porosity-permeability set. The two types of PDFs are not significantly different for all outcomes except for the aerial spread of carbon dioxide.

The pressures experienced near the well during constant mass injection would certainly fracture the host rock. In practice an operator would reduce the injection rate prior to bottomhole pressure reaching fracture pressure similar to the constant pressure simulations performed in this research. This limits the applicability of these results unless the constant mass injection rate is kept sufficiently low or distributed among many wells.

One limitation of this methodology is that homogeneous reservoir properties, specifically permeability and porosity were used. Permeability and porosity have the largest effect on the outcomes selected and the true effect cannot be known without implementing heterogeneous distributions of these properties. This method can be useful as a screening method where the reservoir properties are not well known and an analysis is needed where some uncertainty in the outcome can be tolerated. Use of randomly distributed properties about the mean did not reveal significant changes with the base homogeneous models.

Further work is needed to make the results more widely applicable rather than limited by the initial domain that is selected. This can be done using dimensional analysis so the results are valid at any scale. Incorporation of heterogeneous geologic properties into these models will also improve the applicability of the results.

2.7. Acknowledgements

of authors expressed herein do not necessarily state or reflect those of the United States Government or any agency thereof. This project is managed and administered by Headwaters Clean Carbon Services LLC (HCCS) and funded by DOE/NETL and cost-sharing partners.

2.8.   References

1.   Special Report on Carbon Dioxide Capture and Storage. Intergovernmental Panel on Climate Change: Geneva, Switzerland, 2005.

2.   Bachu, S., Sequestration of CO_2 in Geological Media: Criteria and Approach for Site Selection in Response to Climate Change. *Energy Conversion and Management* **2000,** *41*, 953-970.

3.   Holloway, S., Underground Sequestration of Carbon Dioxide—A Viable Greenhouse Gas Mitigation Option. *Energy* **2005,** *30* (11-12), 2318-2333.

4.   Michael, K.; Golab, A. V.; Shulakova, V.; Ennis-King, J. G.; Allinson, G.; Sharma, S.; Aiken, T. T., Geological Storage of CO_2 in Saline Aquifers—A Review of the Experience from Existing Storage Operations. *International Journal of Greenhouse Gas Control* **2010,** *4*, 659-667.

5.   Litynski, J. T.; Klara, S. M.; McIlvried, H. G.; Srivastava, R. D., The United States Department of Energy's Regional Carbon Sequestration Partnerships Program: A Collaborative Approach to Carbon Management. *Environ. Int.* **2006,** *32* (1), 128-144.

6.   Korbøl, R.; Kaddour, A., Sleipner Vest CO_2 Disposal Injection of Removed CO_2 into the Utsira Formation. *Energy Conversion and Management* **1995,** *36* (6-9), 509-512.

7.   Baklid, A.; Korbøl, R.; Owren, G., Sleipner Vest CO_2 Disposal, CO_2 Injection into a Shallow Underground Aquifer. *SPE Journal* **1996,** *SPE 36600*.

8.   Sato, K.; Saeko, M.; Horie, T.; Ohkuma, H.; Saito, H.; Watanabe, J.; Yoshimura, T., Monitoring and Simulation Studies for Assessing Macro- and Meso-scale Migration of CO_2 Sequestered in an Onshore Aquifer: Experiences from the Nagaoka Pilot Site, Japan. *International Journal of Greenhouse Gas Control* **2011,** *5* (1), 125-137.

9.   Sakai, A. In *4D Seismic Monitoring of the Onshore Carbon Dioxide Injection in Japan*, Proceeding of SEGJ 8th International Symposium-Imaging and Interpretation, 2006.

10.   Lu, J.; Cook, P. J.; Hosseini, S. A.; Yang, C.; Romanak, K. D.; Zhang, T.; Freifeld, B. M.; Smyth, R. C.; Zeng, H.; Hovorka, S. D., Complex Fluid Flow Revealed by Monitoring CO_2 Injection in a Fluvial Formation. *Journal of Geophysical Research* **2012,** *117* (B3).

11.   Hovorka, S. D.; Benson, S. M.; Doughty, C.; Freifeld, B. M.; Sakurai, S.; Daley, T. M.; Kharaka, Y. K.; Holtz, M. H.; Trautz, R. C.; Nance, H. S., Measuring Permanence of CO_2 Storage in Saline Formations: The Frio Experiment. *Environmental Geosciences* **2006,** *13* (2), 105-121.

12. Birkholzer, J. T.; Zhou, Q.; Tsang, C.-F., Large-scale Impact of CO_2 Storage in Deep Saline Aquifers: A Sensitivity Study on Pressure Response in Stratified Systems. *International Journal of Greenhouse Gas Control* **2009,** *3* (2), 181-194.

13. Khuri, A. I., *Response Surface Methodology and Related Topics*. World Scientific: Singapore, 2006.

14. Montgomery, D. C., *Design and Analysis of Experiments*. John Wiley & Sons, Inc.: New York, NY, 2008.

15. Box, G. E. P.; Hunter, W. G.; Hunter, J. S., *Statistics for Experimenters: An Introduction to Design, Data Analysis, and Model Building.* John Wiley & Sons, Inc.: New York, NY, 1978.

16. Lawson, J.; Erjavec, J., *Modern Statistics for Engineering and Quality Improvement*. Brooks/Cole-Thomson Learning: Pacific Grove, CA, 2001.

17. Chu, C. In *Prediction of Steamflood Performance in Heavy Oil Reservoirs Using Correlations Developed by Factorial Design Method (SPE 20020)*, SPE California Regional Meeting, Ventura, California, 4-6 April, 1990.

18. Damsleth, E.; Hage, A.; Volden, R., Maximum Information at Minimum Cost: A North Sea Field Development Study With Experimental Design. *Journal of Petroleum Technology* **1992**, 1350.

19. Egeland, T.; Holden, L.; Larsen, E. A. In *Designing Better Decisions*, European Petroleum Computer Conference, Stavanger, Norway, 24-27 May, 1992.

20. Bu, T.; Damsleth, E., Errors and Uncertainties in Reservoir Performance Predictions. *SPE Formation Evaluation* **1996,** *11* (3), 194-200.

21. Bauman, J. H.; Deo, M. D., Parameter Space Reduction and Sensitivity Analysis in Complex Thermal Subsurface Production Processes. *Energy & Fuels* **2011,** *25* (1), 251-259.

22. Jones, A.; Doyle, J.; Jacobsen, T.; Kjonsvik, D., Which Subseismic Heterogeneities Influence Waterflood Performance? A Case Study of a Low Net-to-Gross Fluvial Reservoir. In *New Developments in Improved Oil Recovery*, Geological Society Special Publication: London, 1995; Vol. 84, p 5.

23. Kjonsvik, D.; Jacobsen, T.; Doyle, J. In *The Effects of Sedimentary Heterogeneities on Production From a Shallow Marine Reservoir - What Really Matters?*, European Petroleum Conference, London, England, 25-27 October, 1994.

24. Willis, B. J.; White, C. D., Quantitative Outcrop Data for Flow Simulation. *Journal of Sedimentary Research* **2000,** *70* (4), 788-802.

25. Narayanan, K.; White, C. D.; Lake, L. W.; Willis, B. J. In *Response Surface Methods for Upscaling Heterogeneous Geologic Models (SPE 51923)*, SPE Reservoir Simulation Symposium, Houston, Texas, 14-17 February, 1999.

26. Narayanan, K. Applications for Response Surfaces in Reservoir Engineering. Masters Thesis, The University of Texas at Austin, Austin, Texas, 1999.

27. Eide, A. L.; Holden, L.; Reiso, E.; Aanonsen, S. I. In *Automatic History Matching by Use of Response Surfaces and Experimental Design*, European Conference on the Mathematics of Oil Recovery, Roros, Norway, 7-10 June; 1994.

28. Dejean, J. P.; Blanc, G., Managing Uncertainties on Production Predictions Using Integrated Statistical Methods. *SPE Journal* **1999,** *SPE 56696*.

29. Liu, B.; Zhang, Y., CO_2 Modeling in a Deep Saline Aquifer: A Predictive Uncertainty Analysis Using Design of Experiment. *Environmental Science & Technology* **2011,** *45* (8), 3504-3510.

30. Myers, R. H.; Montgomery, D. C., *Response Surface Methodology: Process and Product Optimization Using Designed Experiments*. Wiley: New York City, 1995; p 700.

31. Box, G. E. P.; Draper, N. R., *Empirical Model Building and Response Surfaces*. Wiley: New York City, 1987; p 699.

32. Peng, C. Y.; Gupta, R. In *Experimental Design and Analysis Methods in Multiple Deterministic Modelling for Quantifying Hydrocarbon In-Place Probability Distribution Curve*, SPE Asia Pacific Conference on Integrated Modelling for Asset Management, Kuala Lumpur, Malaysia, 29-30 March, 2004.

33. White, C. D.; Willis, B. J.; Narayanan, K.; Dutton, S. P., Identifying and Estimating Significant Geologic Parameters With Experimental Design. *SPE Journal* **2001,** *6* (3), 311-324.

34. Nelson, P. H., Permeability-porosity Relationships in Sedimentary Rocks. *The Log Analyst* **1994,** *35* (3).

35. Koltermann, C. E.; Gorelick, S. M., Heterogeneity in Sedimentary Deposits: A Review of Structure-imitating, Process-imitating, and Descriptive Approaches. *Water Resources Research* **1996,** *32* (9), 2617-2658.

36. Li, S.; Zhang, Y.; Zhang, X., A Study of Conceptual Model Uncertainty in Large-scale CO_2 Storage Simulation. *Water Resources Research* **2011,** *47* (5).

37. Ehlig-Economides, C.; Economides, M. J., Sequestering Carbon Dioxide in a Closed Underground Volume. *Journal of Petroleum Science and Engineering* **2010,** *70* (1-2), 123-130.

38. Zhou, Q.; Birkholzer, J., On Scale and Magnitude of Pressure Build-up Induced by Large-scale Geologic Storage of CO_2. *Greenhouse Gas Science and Technology* **2011,** *1*, 11-20.

39. Draper, N. R.; Smith, H., *Applied Regression Analysis*. Wiley-Interscience: Hoboken, NJ, 1998.

40. CMG, *User's guide GEM, Advanced Compositional Reservoir Simulator (version 2010)*. Computer Modeling Group Ltd.: Calgary, Canada, 2010; p 843.

41. Han, W. S.; Kim, K.-Y.; Esser, R. P.; Park, E.; McPherson, B. J., Sensitivity Study of Simulation Parameters Controlling CO_2 Trapping Mechanisms in Saline Formations. *Transport in Porous Media* **2011,** *90* (3), 807-829.

42. Han, W. S.; Lee, S.-Y.; Lu, C.; McPherson, B. J., Effects of Permeability on CO_2 Trapping Mechanisms and Buoyancy-driven CO_2 Migration in Saline Formations. *Water Resources Research* **2010,** *46* (W07510).

43. Kumar, A.; Ozah, R. C.; Noh, M. H.; Pope, G. A.; Bryant, S. L.; Sepehrnoori, K.; Lake, L. W., Reservoir Simulation of CO_2 Storage in Deep Saline Aquifers. *SPE Journal* **2005,** *10* (3), 336-348.

44. Palisade, *Guide to Using @RISK: Risk Analysis and Simulation Add-In for Microsoft Excel*. Palisade Corporation: Ithaca, NY, 2012; Vol. 6, p 918.

45. Lu, S.; Molz, F. J.; Fogg, G. E.; Castle, J. W., Combining Stochastic Facies and Fractal Models for Representing Natural Heterogeneity. *Hydrogeology Journal* **2002,** *10*, 475-482.

46. Larue, D. K.; Friedmann, F., Stratigraphic Uncertainty in Field Development Studies: A Conceptual Modeling Approach. *The Leading Edge* **2001,** *20*, 28-33.

47. Friedmann, F.; Chawathe, A.; Larue, D. K., Assessing Uncertainty in Channelized Reservoirs Using Experimental Designs. *SPE Reservoir Evaluation & Engineering* **2003,** *6* (4), 264-274.

CHAPTER 3

OPTIMIZATION OF CO_2 SEQUESTRATION AND OIL RECOVERY

IN A MATURE OIL FIELD: SACROC RESERVOIR,

PERMIAN BASIN, WEST TEXAS

Justin Wriedt[a], Milind Deo[a], Weon Shik Han[b] and Jim Lepinski[c]

3.1. <u>Abstract</u>

The purpose of this work is to investigate the potential for carbon dioxide sequestration in a mature oil field with extensive history. The Scurry Area Canyon Reef Operator's Committee (SACROC) reservoir in the West Texas Permian Basin has nearly 65 years of oil production. This reservoir has been undergoing tertiary CO_2 water-alternating-gas recovery for over 40 years. Mature oil fields are a proven underground storage basin with known pressure constraints. Additionally, there has been extensive work done to characterize the geologic and fluid parameters of this site. An upscaled geologic model is provided from previous studies by the Southwest Regional Sequestration Partnership and the Texas Bureau of Economic Geology. The choice of mature oil fields gives the opportunity for some economic benefit in additional oil recovery in addition to long-term

a.) Department of Chemical Engineering, 50 Central Campus Drive, University of Utah, Salt Lake City, Utah 84112.; b.) Department of Geosciences, University of Wisconsin-Milwaukee, Milwaukee, Wisconsin 53201; c.) Headwaters Clean Carbon Services, 10653 River Front Parkway # 300, South Jordan, Utah 84095-3527.

sequestration of carbon dioxide. A history match of the northern platform region of SACROC is performed from the period between 1972 and 2002 when tertiary carbon dioxide flooding was active. Various forward modeling scenarios were simulated to investigate the long-term storage potential as well as oil recovery using the best practices models developed by the U.S. Department of Energy National Energy Technology Laboratory (NETL) for a single well pattern in the region. These results show that on a field scale, co-optimization of oil recovery and carbon dioxide sequestration does not occur. While there is some oil recovery associated with the carbon dioxide flooding cases, there is lower economic benefit for the high volume CO_2 cases.

3.2.   Introduction.

The SACROC Unit is the oldest continuously operated CO_2 enhanced oil recovery (EOR) operation in the United States. Tertiary recovery operations began in 1972 using CO_2 as the primary gas in a water-alternating-gas (WAG) injection scheme. This area has been extensively studied in an effort to better understand EOR[1-6]. In EOR operations, not all of the injected CO_2 is recovered, some portion remains trapped in the subsurface. The long 40-year history has been instrumental in demonstrating the success of CO_2 trapping below an effective sealing layer[7-9].

SACROC is located in the southeastern segment of the Horseshoe Atoll within the Permian Basin in western Texas [Figure 3.1]. The Horseshoe Atoll is a late Paleozoic reef mound comprised of in-place boundstones and bioclastic debris, it is approximately 914 m thick [2]. The Horseshoe Atoll is approximately 282 km long with a total area of 15,540 km^2. The SACROC unit within the Horseshoe Atoll consists of an area of approximately 356 km^2, with a length of 40 km and widths varying from 3 to 15 km. The carbonate reef
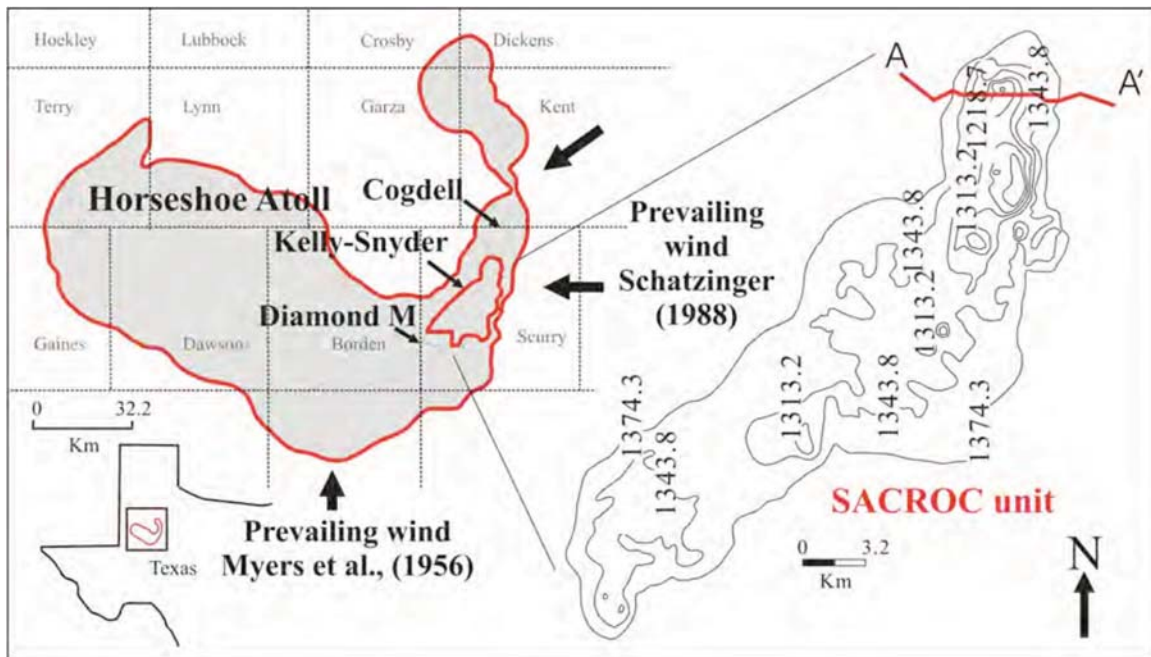
Figure 3.1: SACROC Unit in the Horseshoe Atoll in west Texas and structural contour map of the top of the carbonate reef (modified from Stafford, 1953) [11]. Contours are meter scale.

complex at SACROC is comprised of extensive bedded bioclastic limestone and thin shale beds (mm to cm thick) representing the Pennsylvanian Strawn, Canyon, and Cisco formations and the Lower Permian Wolfcamp Series [10]. Oil production in the SACROC unit is primarily from the Canyon and Cisco formations shown in cross-section A-A' [Figure 3.2] [2]. The Wolfcamp shale provides a low permeability seal overlying the Cisco and Canyon formations [10].

The SACROC unit was discovered by Standard Oil Company of Texas in November 1948. Original oil in place (OOIP) was initially estimated at 2.73 billion STB in the Canyon formation with a solution gas ratio just below 1,000 scf/STB and a bubble point pressure of 1,805 psi (12.45 MPa) [3]. Solution gas drive was the primary production mechanism from 1948 to 1953. The average reservoir pressure was reduced from 3122 psi (21.53 MPa) to 1560 psi (11.38 MPa) with only 5 percent of OOIP produced during this
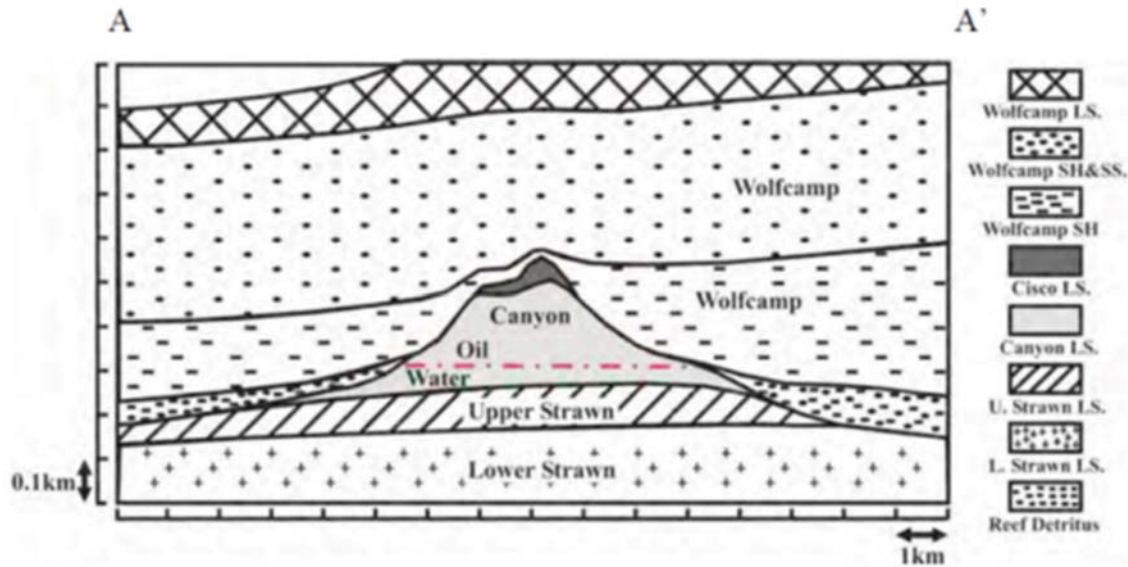
Figure 3.2: A structural and stratigraphic cross-section of profile A-A', located within the SACROC northern platform (modified from Vest, 1970) [2]. See Figure 3.1 for the location of profile A-A'.

period [3-4].

In September 1954 a secondary oil recovery and pressure maintenance plan was implemented with wells placed along the crest of Canyon reef [3-4, 12-15]. This "center-line pattern" was the first approved center-to-edge injection project adopted rather than a typical pattern flood design [16]. The objective of the center-line injection scheme was to not only increase the reservoir pressure above the bubble point but also to displace oil from the center of the SACROC unit toward producing wells on the eastern and western flanks. Production wells were converted to injection wells as the water flood front moved past them toward the margin [16-17]. At the end of the secondary waterflooding activities in 1971, 771 million barrels of water had been injected into the Canyon reef formation. The average reservoir pressure had increased to 2350 psi (16.20 MPa) from a low of 1560 psi (10.76 MPa) during primary production [3, 17]. Center-line water injection swept 72 percent of the reservoir volume, decreasing oil saturation to 26 percent [16].

A study performed by the SACROC engineering committee determined that CO_2–miscible enhanced oil recovery was the most feasible method of tertiary EOR. SACROC was divided into three equal hydrocarbon pore volume (HCPV) phases [Figure 3.3] and would alternate CO_2 flooding between them due to CO_2 supply limitations in the area. This study focuses on the northern platform of SACROC, which is primarily the Phase II section labeled in Figure 3.3. A Water-Alternating-Gas (WAG) injection process was chosen due to improved recovery estimates in the range of 1 to 2 percent more than continuous CO_2 flooding. Additionally, a WAG injection scheme allowed CO_2 flooding to be alternated between all three phases, which was a necessity due to supply issues.

A laboratory study identified the minimum miscibility pressure (MMP) as 1600 psi (11.03 MPa) for CO_2 in SACROC crude oil. The reservoir was undersaturated at the time of discovery having an average pressure of 1936 psi (12.18 MPa) [2].

A life-cycle assessment study was completed to estimate the "best practices" for WAG injection in the Permian Basin [18]. The models used were pattern-level stream tubes for all three cases, which were "historical," "best practices," and "next generation," all described in the following text. These models focused on a single 5-spot well pattern.

While the primary function of CO_2 – EOR is to increase incremental oil recovery, the process may also be a viable solution for storing anthropogenic CO_2 through geologic sequestration. The historical case considers previous CO_2-EOR recovery designs where the cost of CO_2 limited the volumes available for injection. For the purposes of this study the total cumulative CO_2 injected over the lifetime of the flood is 40 percent of the HCPV. Additionally, for the historical case, a slug of water is injected into the formation at the end of the CO_2 flood to recover residual CO_2 that remains in the formation.

A series of studies have been sponsored by the U.S. Department of Energy to evaluate
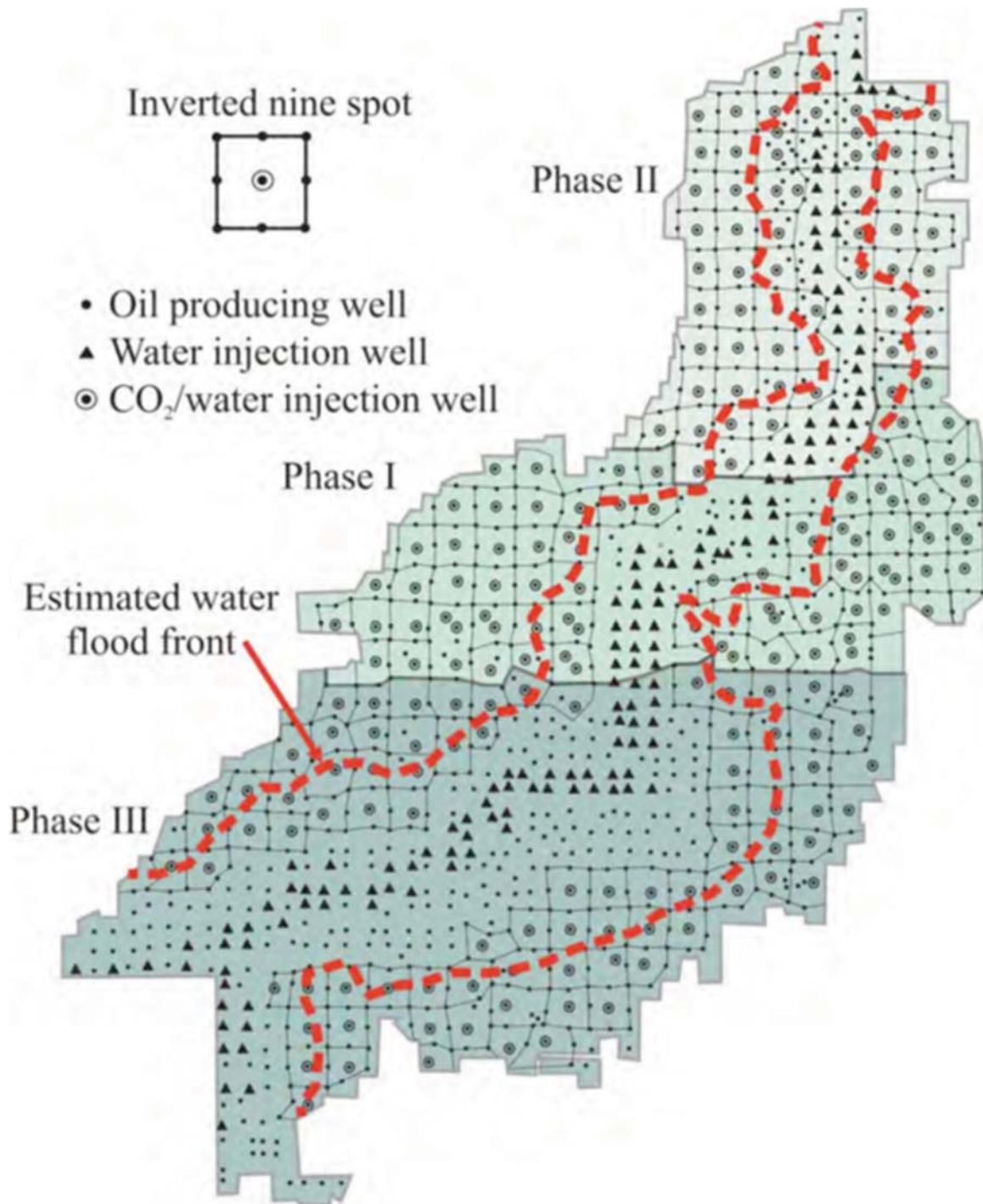
Figure 3.3: Well locations and phase areas in the 1973 SACROC Unit CO_2 development plan (modified from Kane, 1979) [17], with the estimated water flood front indicated in red.

CO_2 – EOR potential in basins and reservoirs within the United States. The culmination of these studies focused on multiple factors, including a variety of oil and price scenarios, to develop a CO_2 – EOR best practices injection scenario [19]. The best practices definition significantly increases the HCPVs injected to 1.0 (compared to 0.4 for historical). Another modification for the best practices scenario relative to the historical case was using a tapered WAG injection process rather than a water slug near the end of CO_2 injection.

The next generation techniques and practices are proposed to not only increase subsurface storage but also to stimulate oil recovery beyond what is typically recovered in the historical and best practice scenarios. NETL lists several technological or operational alternatives to the historical and best practices scenarios necessary to be considered a next generation injection method. In this case the requirement is satisfied by increasing the volume of CO_2 injection to 1.5 HCPV more than best practices [20]. The next generation case uses a tapered WAG injection process similar to the best practices scenario.

3.3.   Approach / Methodology

A high-resolution geocellular model of the SACROC northern platform was created by the Texas Bureau of Economic Geology using an array of information including core data, well-logs, sedimentological analysis, stratigraphic interpretation and three-dimensional seismic data [21] [Figure 3.4]. The permeability was estimated using a rock-fabric based approach based on the premise that pore size distribution in relation to rock fabric controls permeability in carbonate rocks [22-23]. The original geocellular model developed for the Cisco and Canyon formations had 9,450,623 (149 x 287 x 221) elements.

In order to reduce computational time, the geocellular model was upscaled using a renormalization technique. This is a local technique using an upscaling algorithm
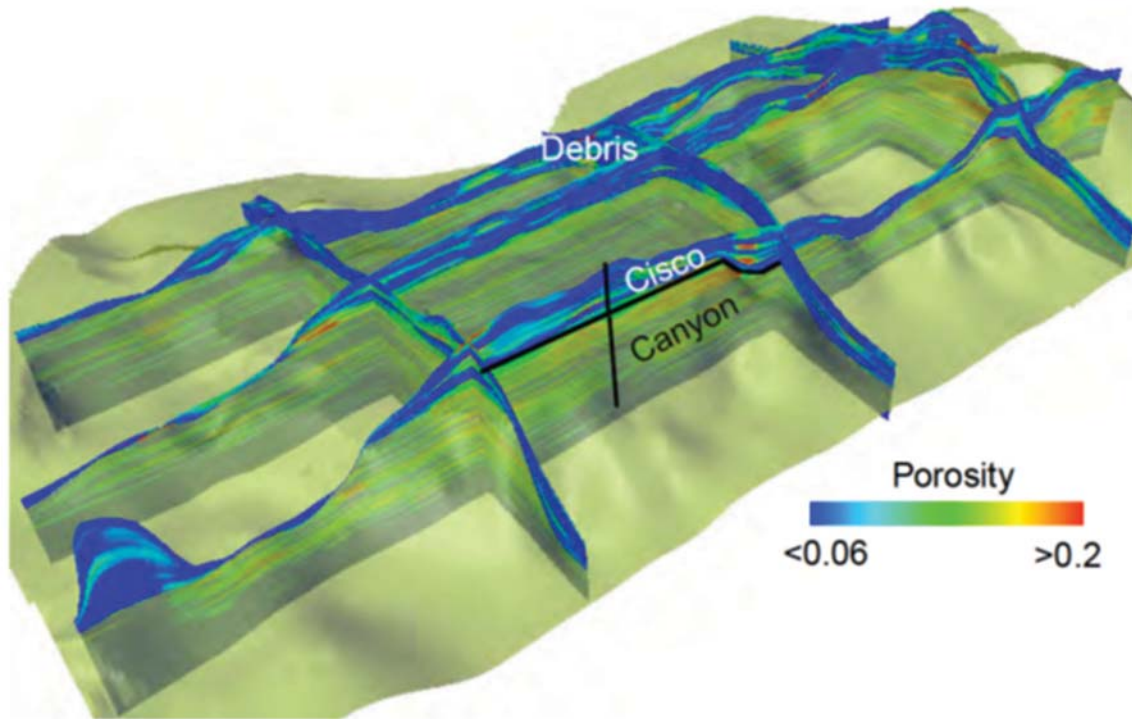
Figure 3.4 Spatial heterogeneity of porosity determined by wireline log.

developed through an equivalent resistor network model [24]. After a series of three renormalizations, a suitable model for CO_2 sequestration simulation, consisting of 13,600 grid blocks, was developed [Figure 3.5].

All simulations were performed using Computer Modeling Group's Generalized Equation-of-State Model (CMG-GEM) Compositional reservoir simulator [25]. GEM is an EOS based compositional reservoir simulator for modeling the flow of three-phase, multicomponent fluids. CMG-GEM have been used to model CO_2 sequestration in previous studies[26-30].

The PVT model used in these simulations was developed using the Peng-Robinson equation of state. The oil phase is regarded as a mixture of 11 different gas components. The initial oil composition used is summarized in Table 3.1 [3]. The CO_2 solubility in the
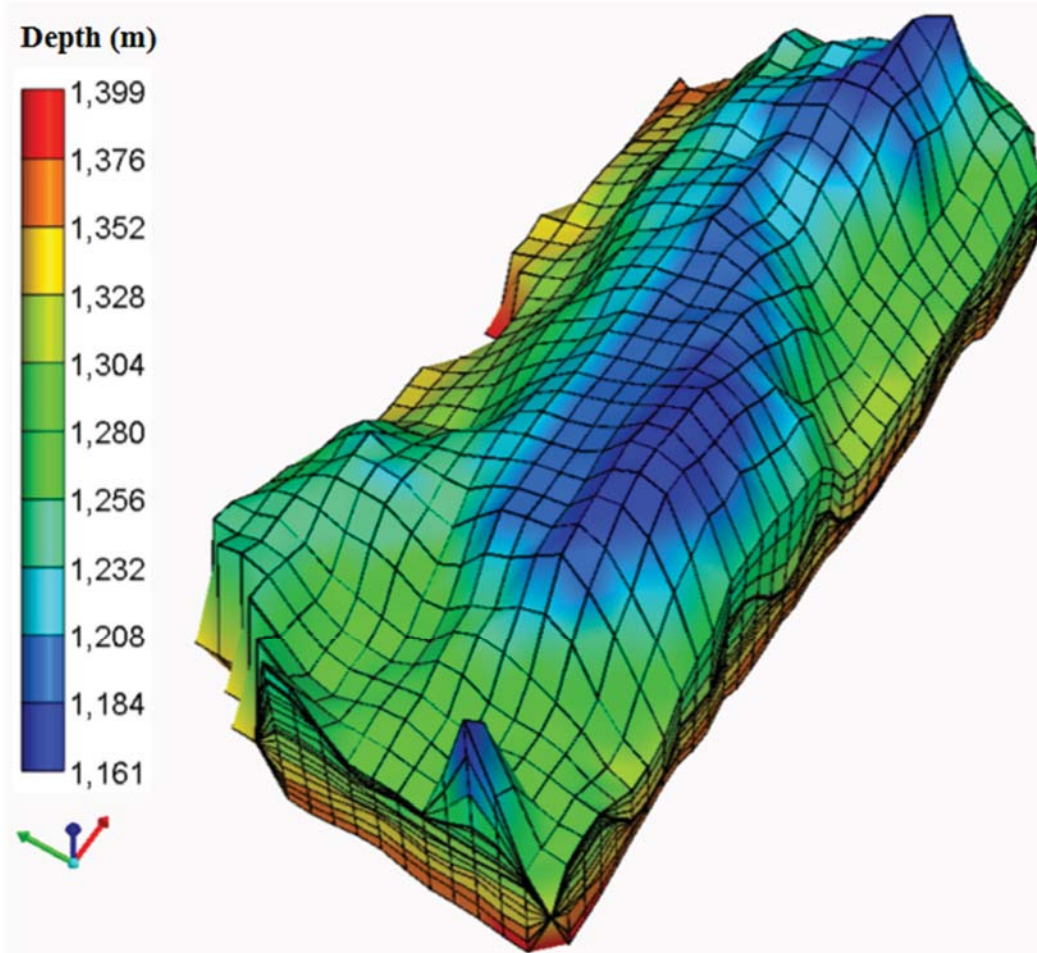
Figure 3.5: CMG simulation model displaying the depths in meters.

aqueous phase was modeled using Henry's Law [31]. No chemical reactions were considered in this modeling due to the computational expense. The reactions are not expected to be significant for the time frame investigated in this study.

The relative permeability function between supercritical CO_2 and liquid was extrapolated from relative permeability data measured in similar carbonate rock [Figure 3.6] [32]. Han used a relative permeability curve for oil measured from SACROC cores by Rohan and Haggerty[33] to calibrate oil relative permeability curves[21]. Hysteresis effects were modeled using a modified Land equation [34].

Table 3.1: Oil composition and molecular weights used in the fluid model.

Oil Composition	Mol	Molecular Weight
CO_2	0.0032	44.01
N_2	0.0083	28.01
C_1 (Methane)	0.2865	16.04
C_2 (Ethane)	0.1129	30.07
C_3 (Propane)	0.1239	44.10
$I-C_4$ (I-Butane)	0.0136	58.12
$N-C_4$ (N-Butane	0.0646	58.12
$I-C_5$ (I-Pentane)	0.0198	72.15
$N-C_5$ (N-Pentane)	0.0251	72.15
FC_6 (Hexane)	0.0406	86.00
C_7+ (Heptane plus)	0.3015	275.00
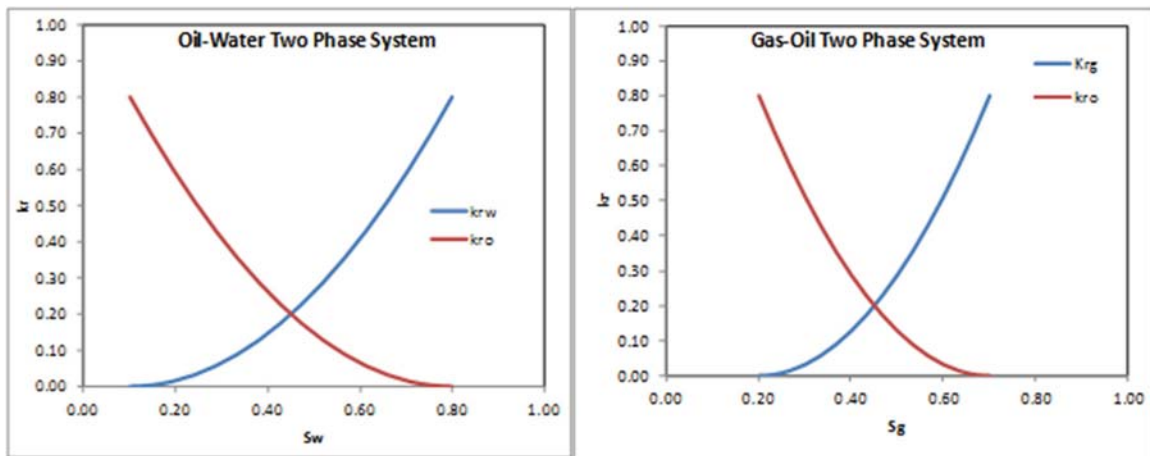
Figure 3.6: Relative permeability curves for the gas-water and oil-water system.

A flood front was estimated from the literature [17], with saturation estimates based on residual oil saturation values from core testing, assuming a full sweep of the affected area, as shown in Figure 3.3.

A volume balance for the SACROC Northern Platform was used to validate the initial pore volumes and saturations of the reservoir in 1972. At the time of discovery the SACROC unit was estimated to have 2.727 billion STB of original oil in place [3]. The initial oil and water saturations were estimated at 0.718 and 0.282 respectively [2]. Using the formation volume factor of 1.472 reported in Dicharry (1973) the total hydrocarbon pore volume is calculated to be 4.014 billion reservoir barrels. The Northern Platform Area is estimated to be 15000 acres, approximately 30 percent of the total SACROC Unit area.

A full-field history for the SACROC Unit was obtained from the Carbon Science and Engineering Research Group at the University of Utah. The production history between 1948 and 1971 was used to calculate the volumes of oil and water in place prior to the CO_2 flooding phase. The cumulative values from the provided data file, between 1972 and 2002, were used to obtain a better history match of the injected and produced fluid volumes summarized in Table 3.2. Only annual cumulative values were given for the Northern Platform with no individual well data.

Table 3.2: Cumulative volumes injected in the northern platform of SACROC between 1972 and 2002.

Fluid Stream	Cumulative Volume
CO2 Injected (TCF)	622.8
Water injected (MM BBL)	2,614.0
Oil produced (MM BBL)	358.6
Water produced (MM BBL)	2,177.0

The porosity of the Northern Platform reservoir averages 9.8 percent [35]. The upscaled porosity values were adjusted uniformly to be consistent with the total pore volume estimated for the material balance. The water saturation in the center-line waterflooded region was adjusted to match the total water and oil in place for the model in 1972. In this model the water saturation for the waterflooded region is considered 0.51; and the residual saturation value 0.28 in all other locations. The saturations are considered uniform in the z-direction. The volume balance comparison is shown in Table 3.3.

The initial pressure of the reservoir on January 1, 1972 is set at a constant value of 2386 psi (16.45 MPa). The wells were arranged in an inverted 9-spot pattern with three production wells for each injection well, with a single grid block spacing between patterns. The model has 165 producers and 55 water/CO_2 injectors. Due to the large grid block size it is not possible to include all of the wells in the Northern Platform Site.

3.4.   Forward Modeling

The projection modeling was done based on a report published by NETL for determining the "best practices" for WAG injection for a typical Permian Basin reservoir[18]. The NETL report only considers a single well pattern and the surrounding area. This

Table 3.3: Volume material balance comparison with the CMG model for the entire SACROC field and the northern platform at discovery and in 1972.

	Pore Volume (MM BBL)	HCPV (MM BBL)	OOIP (MM STB)	Average Porosity
SACROC Full Field (1948)	5.575	4.014	2.727	0.098
SACROC North Platform (1948)	2.509	1.806	1.227	0.098
SACROC North Platform (1972)	2.509	1.483	1.007	0.098
CMG Model (1972)	2.496	1.485	1.003	0.102

modeling applies these cases to the entire Northern Platform reservoir with a 5-spot injection pattern. Four cases were analyzed, a historical, best practices, next generation, as well as a continuous CO_2 flood. The historical case is based on methods adopted in the early years of tertiary recovery using CO_2. The best practices scenario is based on the optimal methods determined by NETL. The next generation case assumes there is an incentive to sequester long term and injects a large volume of CO_2 relative to the other scenarios. The best practices and next generation cases continue the WAG injection for the entire length of the flood and cumulative storage increases throughout the duration in these cases. For the historical case the stored volume decreases due to a water slug that chases the WAG cycle [Table 3.4].

The injection rate for the reservoir varied for each scenario. The historical and continuous case injected 0.4 HCPV while the best practices and historical cases injected 1 and 1.5 HCPV, respectively. The reservoir was modeled with 56 5-spot patterns due to the larger grid block sizes. Water curtains surrounding the individual patterns were not modeled; instead water and CO_2 were injected in an alternating pattern throughout the reservoir and were alternated bi-annually.

Table 3.4: Forward modeling scenarios indicating WAG cycle ratios and length of time in years for the total flood.

		Injection Increment (Years)				
		1–2–3	4–5–6–7	8–9–10–11–12	13–14–15	16–17
Historical	CO_2	100% · 50%	33%	25%	0%	
	Water	0% · 50%	67%	75%	100%	
Best Practices	CO_2	100% · 50%	33%		25%	
	Water	0% · 50%	67%		75%	
Next Generation	CO_2	100% · 50%	33%		25%	
	Water	0% · 50%	67%		75%	

3.5.   Results and Discussion

3.5.1. History Match

A cumulative history match should provide the relative saturation values for the entire

field after operation ceased. A yearly match was performed on injected water [Figure 3.7]

and CO_2 [Figure 3.8] amounts using a constant rate injection scheme. Injection values were

set for each individual well based on its injectivity where no well injects 15 percent more

than any other. The matching required that both water and CO_2 were injected in the field

continuously. The water and CO_2 injectors were assigned in an alternating pattern allowing

for half of each group of wells to be operating at all times. These groups were then

alternated yearly. Multiple iterations have been performed in order to match the produced

Figure 3.7: History match curves for cumulative water injection between 1972 and 2002.
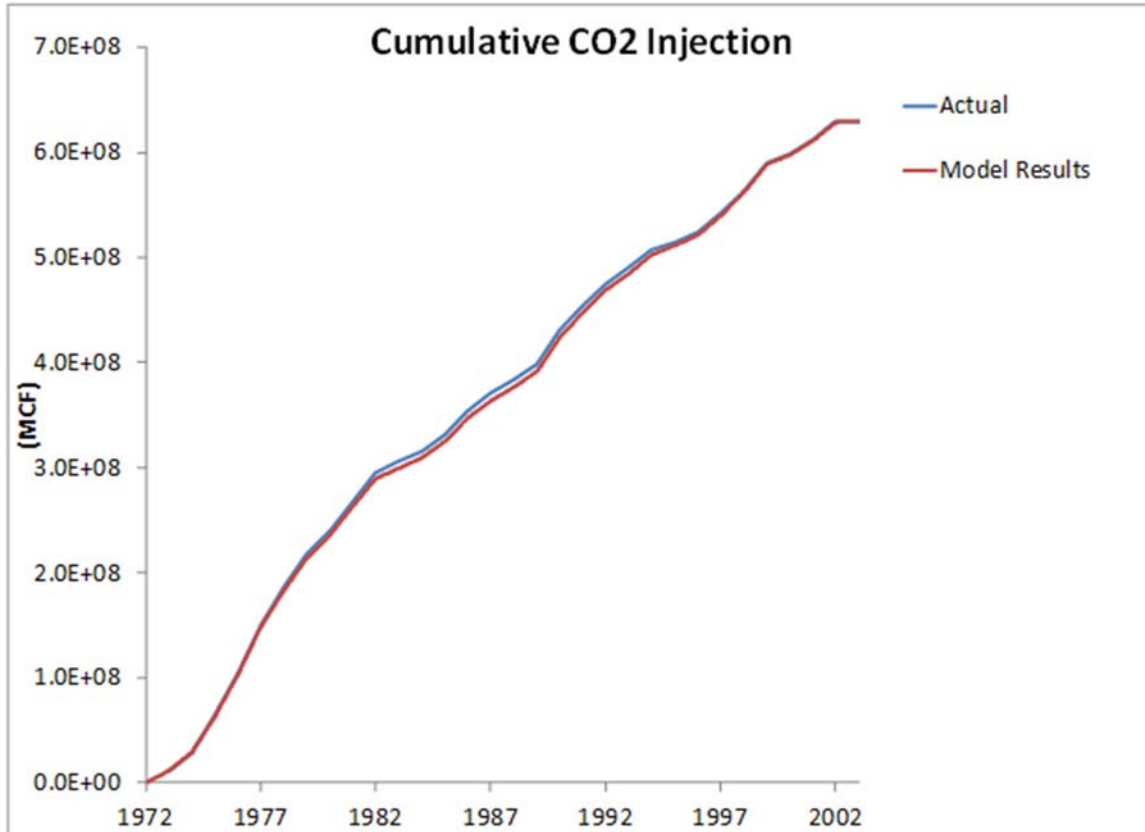
Figure 3.8: History match curves for cumulative CO_2 injection between 1972 and 2002.

volumes for oil, water and CO_2. A constant pressure production scheme was used for all producers. The production pressure was adjusted periodically to better match the oil production [Figure 3.9]. The water production trend matches closely with the field data; however, it over produces for the first 20 years and then under produces for the last few but nearly matches the cumulative volume produced in 2002 [Figure 3.10].

The model results match the field data relatively well with exception of the cumulative produced CO_2 [Figure 3.11]. A considerable volume of additional CO_2 is produced in the model. When evaluating the total gas production, shown in [Figure 3.12], the cumulative volumes are within 7.7 percent of the field data. Additionally, the hydrocarbon gas that is produced [Figure 3.13] is significantly less than the measured field volumes. It is possible
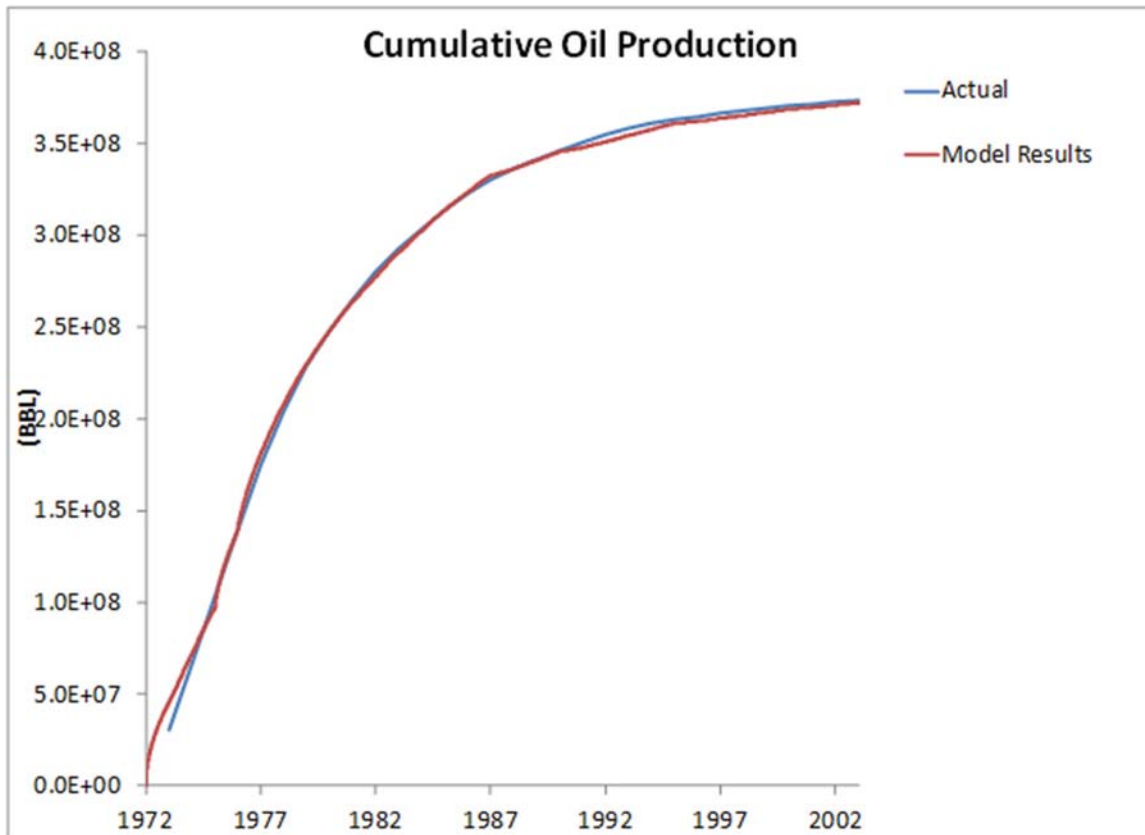
Figure 3.9: History match curves for cumulative oil production between 1972 and 2002.

that this is caused by the difference in volumetric accounting of the simulator compared to

the field operators. The operators generally consider hydrocarbon gas to be all gas that is

produced in solution, including CO_2. For the SACROC field the hydrocarbon gas-oil ratio

(HCGOR) was historically about 1000 SCF/STB from discovery in 1948 until the end of

waterflooding in 1972 [36]. During CO_2 flooding the HCGOR increased to 1449 SCF/STB

on average with a maximum value of 2829 SCF/STB in 1994 for the subset of wells used

to create the geologic model. We believe this increase in HCGOR is due to production of

CO_2 that has dissolved in oil. The reported CO_2 production values likely only include free

gas volumes that were produced, and did not include total CO_2 produced from the reservoir.

The model results report the volumes produced, at surface conditions, after all degassing
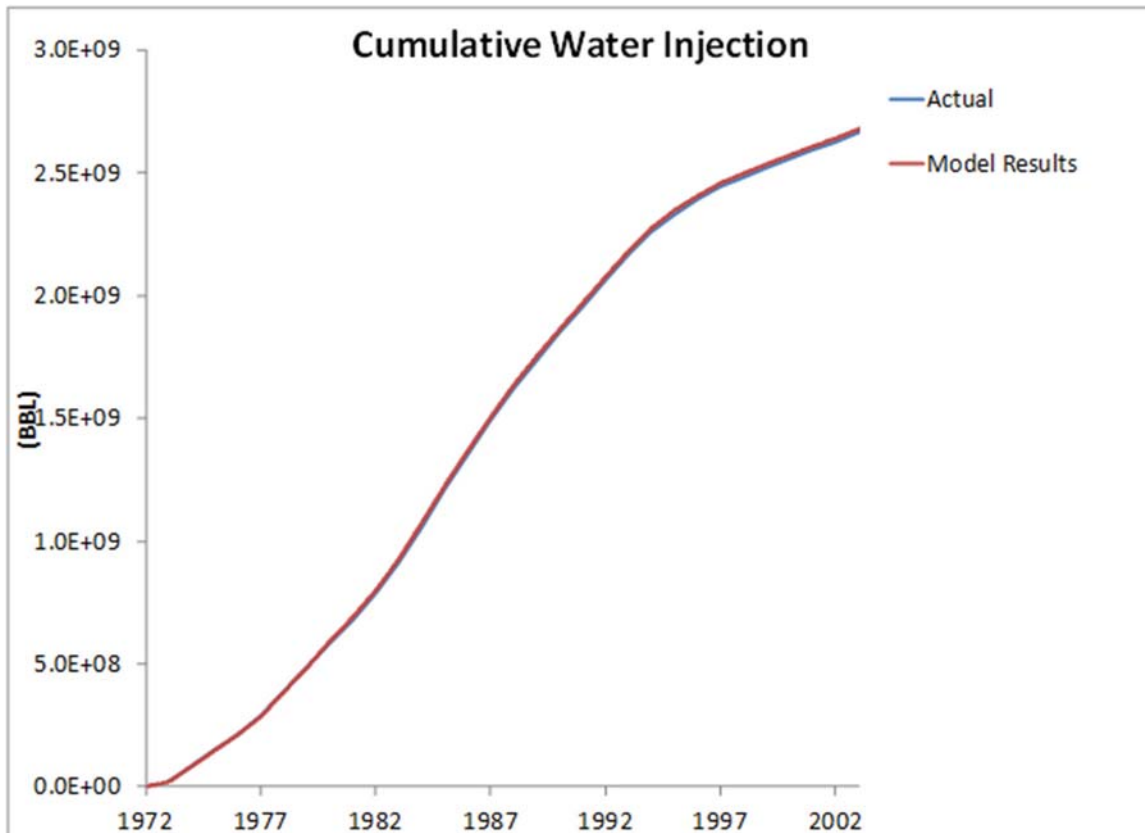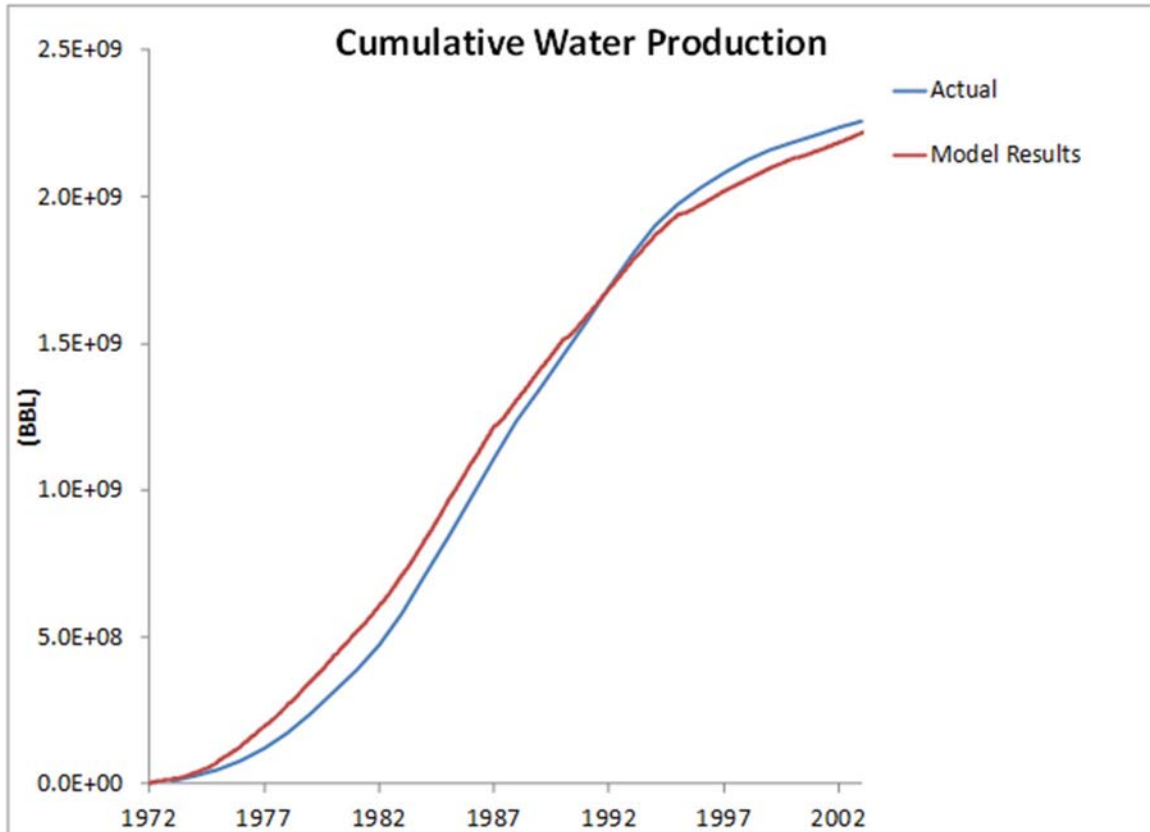
Figure 3.10: History match curves for cumulative water production between 1972 and 2002.
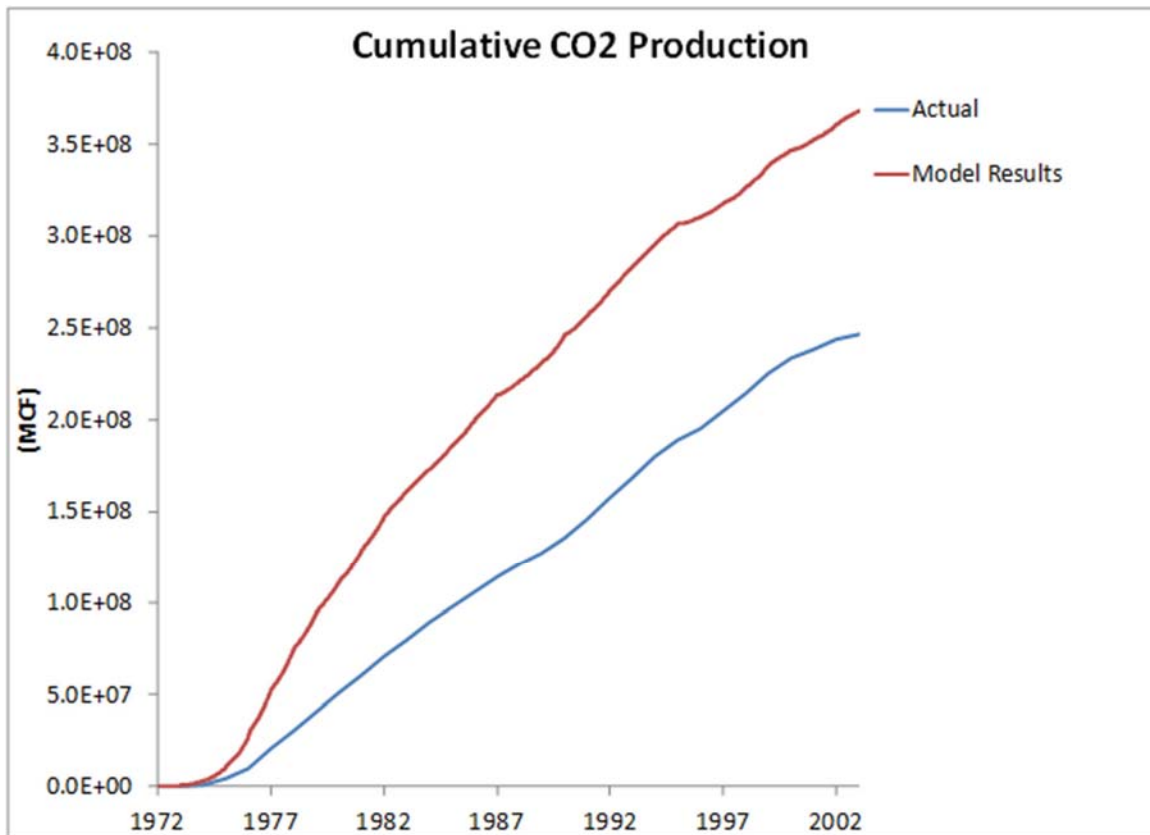
Figure 3.11: History match curves for cumulative CO_2 production between 1972 and 2002.
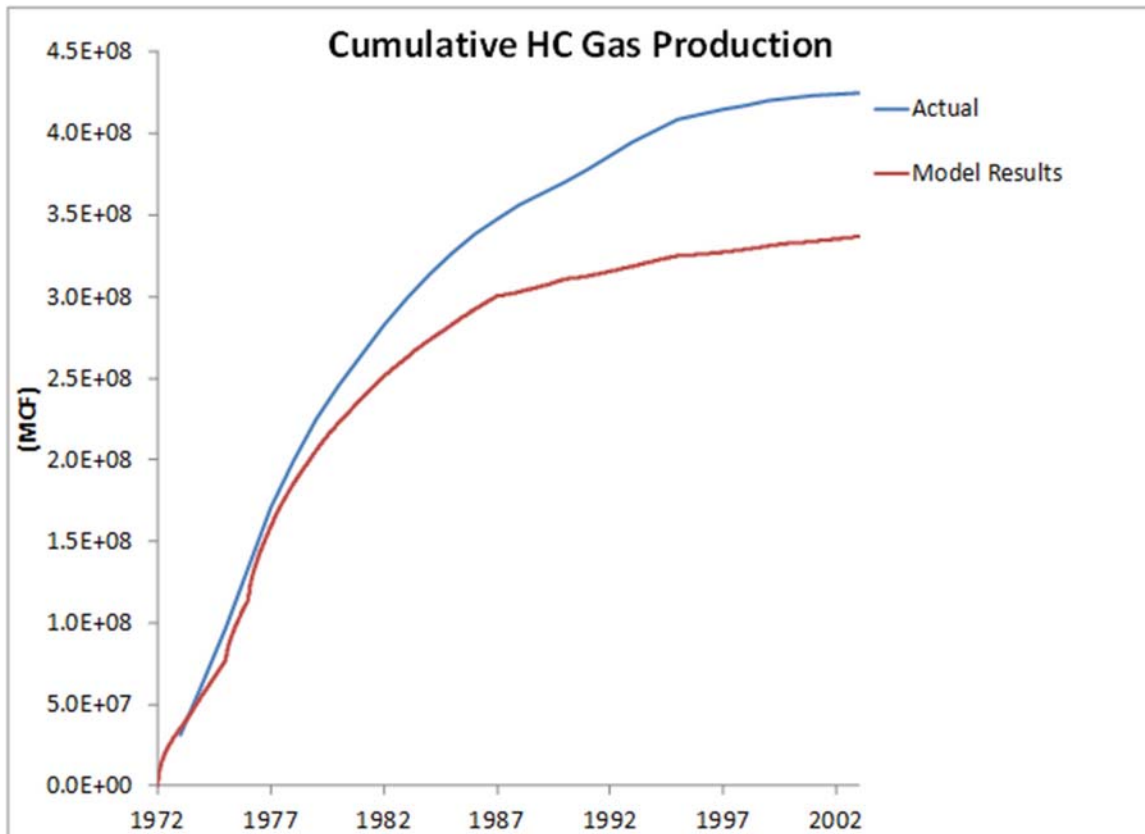
Figure 3.12: History match curves for cumulative hydrocarbon gas production between 1972 and 2002.

71
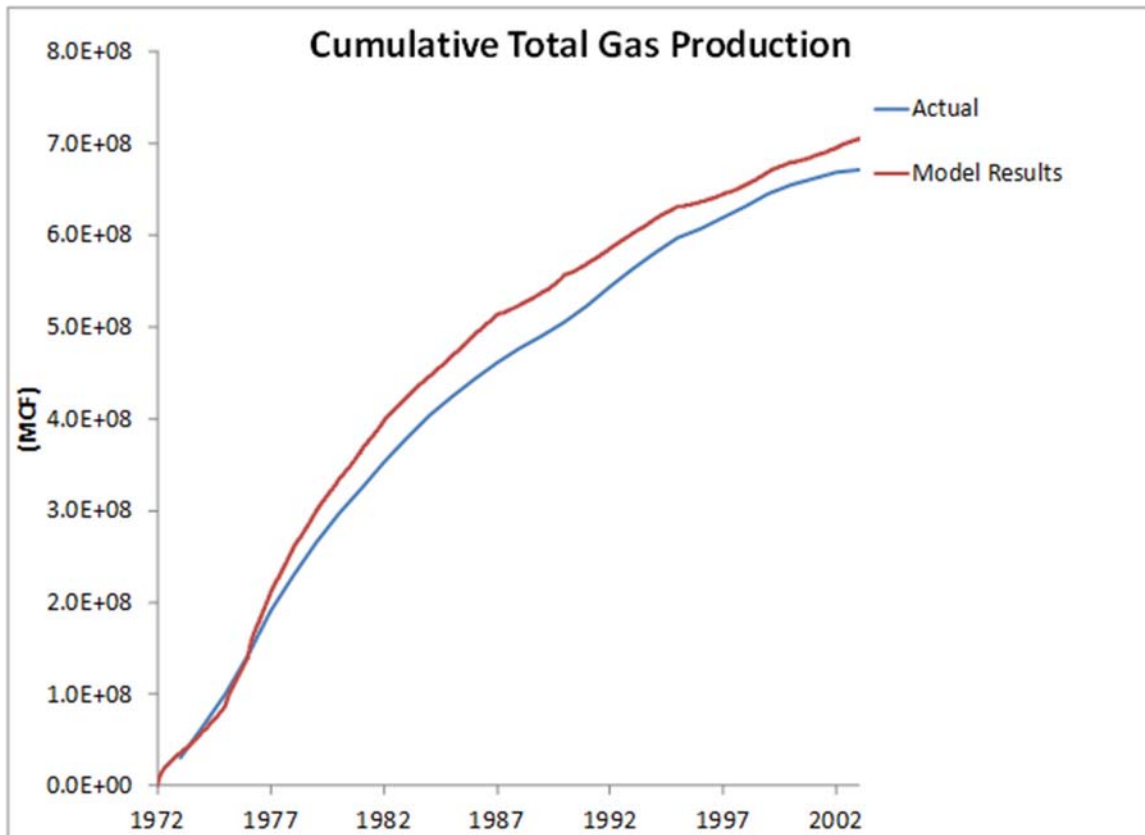
Figure 3.13: History match curves for cumulative total gas production between 1972 and 2002.

of the liquids has occurred, and does not account for free gas and dissolved gas separately. Overall the total gas production from the model is higher than the field data and could be caused by other modeling effects. This model only considers the Northern Platform and does not include any interaction with the southern portion of the SACROC field (Phase I). Although the southern border of the model is considered an open boundary, it does not allow for any pressure changes that may be occurring due to operation in the southern portion of the field. The spacing of the grid blocks, which cause the wells to be placed in adjacent blocks, may limit the ability of the CO_2 to migrate outside of the well pattern area.

Generalized relative permeability curves were used and attempts were made to modify the relative permeability curves to reduce the migration of CO_2 to the production wells;

however, these effects were minimal. Additionally, the wells in the model are perforated along the full thickness of the model, which may cause additional production of CO_2 that would normally remain in the reservoir. It is expected that some gravity override would occur near the top of the reservoir, which may not necessarily be produced without this completion scheme.   It is likely that a combination of all these effects may be contributing to the projected higher CO_2 production.

3.5.2. Forward Modeling

Operations in the SACROC Northern Platform site ceased in 2002 and were not restarted until 2009. Injection and production were shut-in after 2002, but the simulation was run until the beginning of 2009. The total percent of original oil in place (OOIP) produced prior to 2009 was 48.3 percent.

The relative incremental increases for the four scenarios are summarized in Table 3.5. For the four injection scenarios, the length of injection and CO_2 volume injected controls the overall oil production [Figure 3.14]. The best practices and next generation scenarios increase oil recovery at nearly the same rate.

Table 3.5: Percentage OOIP recoveries for each of the forward modeling where 48.3 percent OOIP was recovered prior to 2009.

Scenario	% OOIP recovered at end of injection period	Incremental Recovery (% OOIP)
Continuous	51.5	3.2
Historical	52.2	3.9
Best Practices	55.4	7.1
Next Generation	57.8	9.5
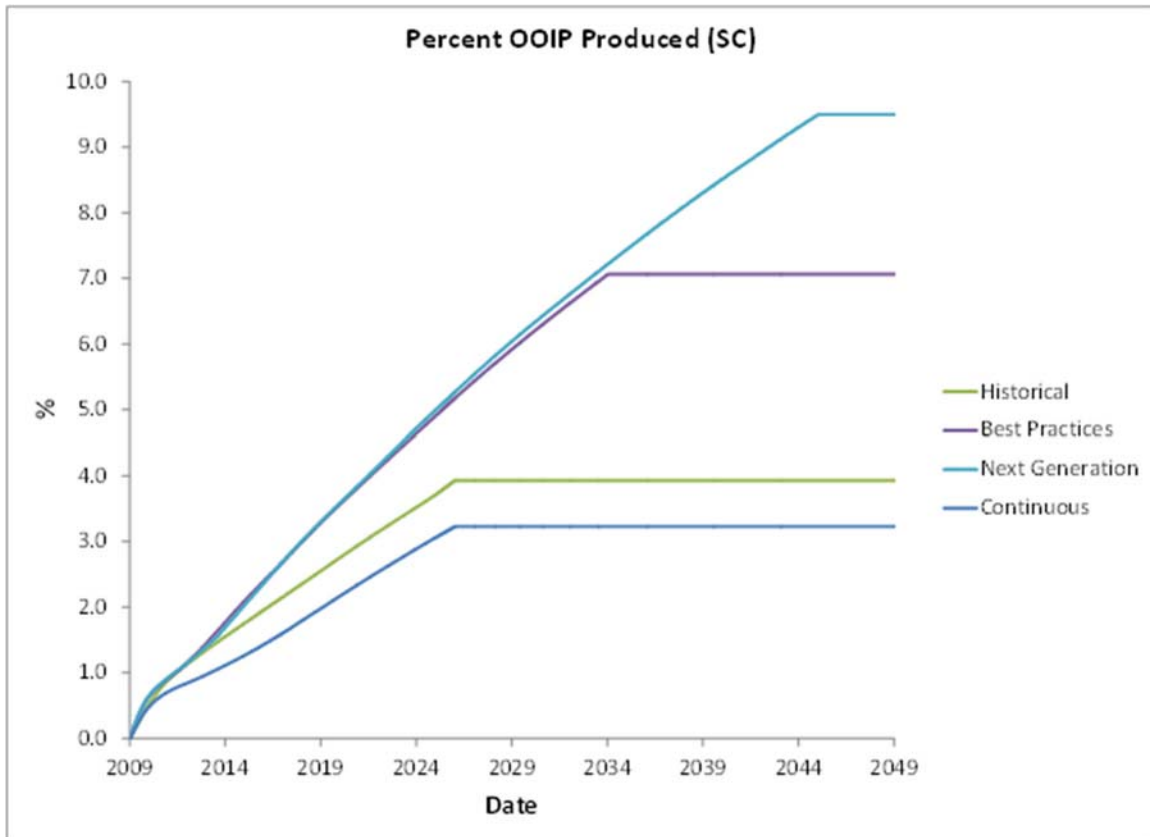
Figure 3.14: Percentage OOIP recoveries for each of the forward modeling scenarios where 48.3 percent OOIP was recovered prior to 2009.

While the oil recovery rates are similar, the next generation case requires the largest volume of CO_2 injected per barrel of oil recovered while also retaining the most CO_2 subsurface per barrel of oil produced [Figure 3.15]. The economic incentive of oil recovery is decreased for the highest volume CO_2 injection cases.

3.6.   Conclusions

A history match is performed to obtain the relative saturations of oil, water, hydrocarbon gas and carbon dioxide. Forward modeling is then performed to determine the best practices for CO_2 sequestration in mature oil fields based on NETL guidelines. For this investigation of carbon dioxide sequestration into a mature oil field, it is found that
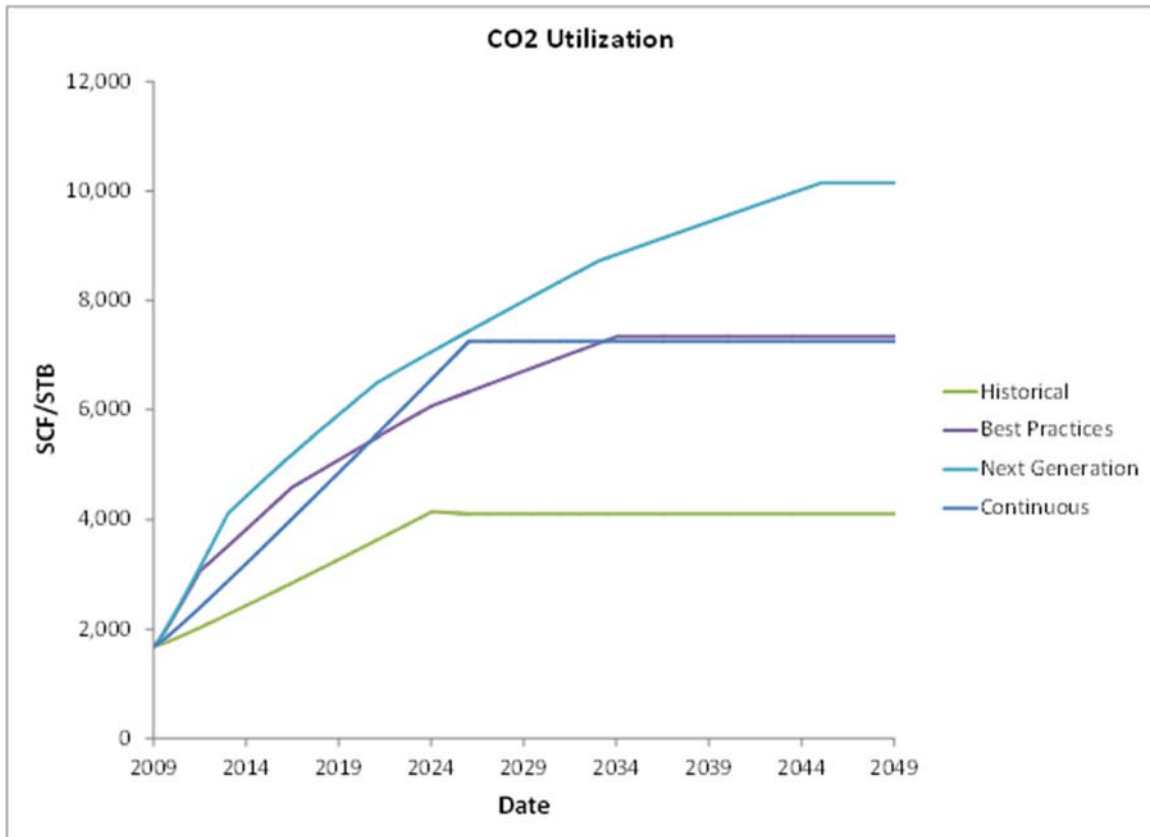
Figure 3.15: Total CO_2 utilization for all forward modeling cases in standard cubic feet of CO_2 injected per stock tank barrel of oil produced.

co-optimization of oil recovery and carbon dioxide is not possible. As higher volumes of CO_2 are injected, the oil production reaches a limit where it may not be economical for sequestration.

3.7. Acknowledgements

usefulness of any information, apparatus, product, or process disclosed, or represents that

its use would not infringe upon privately owned rights. Reference herein to any specific

commercial product, process, or service by trade name, trademark, manufacturer, or

otherwise does not necessarily constitute or imply its endorsement, recommendation, or

favoring by the United States Government or any agency thereof. The views and

opinions of authors expressed herein do not necessarily state or reflect those of the United

States Government or any agency thereof. This project is managed and administered by

Headwaters Clean Carbon Services LLC (HCCS) and funded by DOE/NETL and cost-

sharing partners.

3.8.   <u>References</u>

1.   Bergenback, R. E.; Terriere, R. T., Petrography and Petrology of Scurry Reef, Scurry County, Texas. *AAPG* **1953,** *37* (5), 1014-1029.

2.   Vest, J., E. L., Oil Fields of Pennsylvanian-Permian Horseshoe Atoll, West Texas. *Geology of Giant Petroleum Fields, AAPG, Memoirs* **1970,** *14*, 185-203.

3.   Dicharry, R. M.; Perryman, T. L.; Ronquille, J. D., Evaluation and Design of a CO_2 Miscible Flood Project - SACROC Unit, Kelly-Snyder Field. *Journal of Petroleum Technology* **1973,** *25* (11).

4.   Brummett Jr., W. M.; Emanuel, A. S.; Ronquille, J. D., Reservoir Description by Simulation at SACROC - A Case History. *Journal of Petroleum Technology* **1976,** *28* (10), 1241-1255.

5.   Graue, D. J.; Belevins, T. R., SACROC Tertiary CO_2 Pilot Project. *SPE Journal* **1978,** *SPE 7090*.

6.   Hawkins, J. T.; Benvegnu, A. J.; Wingate, T. P.; McKamie, J. D.; Pickard, C. D.; Altum, J. T., SACROC Unit CO_2 Flood: Multidisciplinary Team Improves Reservoir Management and Decreases Operating Costs. *SPE Journal* **1996,** *SPE 35359*, 141-148.

7.   Carey, J. W.; Wigand, M.; Chipera, S. J.; WoldeGabriel, G.; Pawar, R.; Lichtner, P. C.; Wehner, S. C.; Raines, M. A.; Guthrie, G. D., Analysis and Performance of Oil Well Cement with 30 Years of CO_2 Exposure from the SACROC Unit, West Texas, USA. *International Journal of Greenhouse Gas Control* **2007,** *1* (1), 75-85.

8.   Han, W. S.; McPherson, B. J.; Raines, M.; Sulaiman, A. I. In *Comparison of Two CO_2 EOS Algorithms: Minor Contrasts in State Properties may Translate to Significant Contrasts in Predicted Migration Histories*, Proceedings of the 5th Annual Conference on Carbon Capture & Sequestration, Alexandria, Virginia, 2006.

9.   Holtz, M. H.; Smyth, R. C.; McPherson, B. J.; Han, W. S. In *Subsurface Characterization of CO_2 Sequestration Sites, Examples from a Carbonate Reef Setting*, Proceedings of International Symposium on Site Characterization for CO2 Geological Storages (CO2SC), L.B.N.L., Berkeley, California, 2006.

10.   Raines, M.; Dobitz, J. K.; Wehner, S. C., A Review of the Pennsylvanian SACROC Unit. In *The Permian Basin: Microns to Satellites, Looking for Oil and Gas at All Scales*, Viveiros, J. J.; Ingram, S. M., Eds. The West Texas Geological Society: 2001; Vol. 01-110, pp 67-74.

11.   Stafford, P. T., Scurry Field: Scurry, Kent and Border Counties, Texas. In *Occurrence of Oil and Gas in West Texas*, Herald, F. A., Ed. Bureau of Economic Geology: 1954; Vol. 5716, pp 295-302.

12. Allen, H. H.; LaRue, C. R., SACROC Unit Operations. *SPE Journal* **1957,** *SPE 823-G*, 21-25.

13. Allen, H. H.; Thomas, J. B., Pressure Maintenance in SACROC Unit Operations. *SPE Journal* **1959,** *SPE 1259-G*, 42-48.

14. Bayat, M. G.; Pickard, C. D.; Benvegnu, A. J.; Wingate, T. P.; Larkin, R. In *Linking Reservoir Characteristics and Recovery Processes at SACROC - Controlling Wasteful Cycling of Fluids at SACROC While Maximizing Reserves*, Second Annual Subsurface Fluid Control Symposium and Conference, Houston, Texas 1996.

15. Dixon, B. P.; Newton Jr., L. E., Reinjection of Large Volumes of Produced Water in Secondary Operations. *SPE Journal* **1965,** *SPE 1147*, 781-789.

16. Burkett, G. D., Review of the Carbon Dioxide Enhanced Oil Recovery Project at the SACROC Unit-Kelly-Snyder Field, Texas. *Chevron Technical Report* **1979**.

17. Kane, A. V., Performance Review of a Large-Scale CO_2-WAG Enhanced Recovery Project, SACROC Unit Kelly-Snyder Field. *Journal of Petroleum Technology* **1979,** *31* (2), 217-231.

18. An Assessment of Gate-to-Gate Environmental Life Cycle Performance of Water-Alternating-Gas CO_2-Enhanced Oil Recovery in the Permian Basin. NETL, Department Of Energy: 2010.

19. Storing CO_2 with Enhanced Oil Recovery. NETL, Department Of Energy: 2008.

20. Storing CO_2 with Next Generation CO2-EOR Technology. NETL, Department Of Energy: 2009.

21. Han, W. S. Evaluation of CO_2 Trapping Mechanisms at the SACROC Northern Platform: Site of 35 Years of CO_2 Injection. Doctorate of Philosophy, The New Mexico Institute of Mining and Technology, Socorro, New Mexico, 2008.

22. Lucia, F. J., Rock-fabric/Petrophysical Classification of Carbonate Pore Space for Reservoir Characterization. *AAPG Bulletin* **1995,** *79* (9), 1275-1300.

23. Lucia, F. J., *Carbonate Reservoir Characterization*. Springer-Verlag: Berlin, 1999.

24. King, P. R., The Use of Renormalization for Calculating Effective Permeability. *Transport in Porous Media* **1989,** *4*, 37-58.

25. CMG, *User's guide GEM, Advanced Compositional Reservoir Simulator (version 2010)*. Computer Modeling Group Ltd.: Calgary, Canada, 2010; p 843.

26. Ehlig-Economides, C.; Economides, M. J., Sequestering Carbon Dioxide in a Closed Underground Volume. *Journal of Petroleum Science and Engineering* **2010,** *70* (1-2), 123-130.

27. Han, W. S.; Kim, K.-Y.; Esser, R. P.; Park, E.; McPherson, B. J., Sensitivity Study of Simulation Parameters Controlling CO_2 Trapping Mechanisms in Saline Formations. *Transport in Porous Media* **2011,** *90* (3), 807-829.

28. Han, W. S.; Lee, S.-Y.; Lu, C.; McPherson, B. J., Effects of Permeability on CO_2 Trapping Mechanisms and Buoyancy-driven CO_2 Migration in Saline Formations. *Water Resources Research* **2010,** *46* (W07510).

29. Kumar, A.; Ozah, R. C.; Noh, M. H.; Pope, G. A.; Bryant, S. L.; Sepehrnoori, K.; Lake, L. W., Reservoir Simulation of CO_2 Storage in Deep Saline Aquifers. *SPE Journal* **2005,** *10* (3), 336-348.

30. Wriedt, J.; Deo, M.; Han, W. S.; Lepinski, J., A Methodology for Quantifying Risk and Likelihood of Failure for Carbon Dioxide Injection into Deep Saline Aquifers. *International Journal of Greenhouse Gas Control* **2014,** *20*, 196-211.

31. Li, Y.-K.; Nghiem, L., Phase Equilibria of Oil, Gas, and Water/Brine Mixtures from a Cubic Equation of State and Henry's Law. *Canadian Journal of Chemical Engineering* **1986**, 486-496.

32. Bennion, D. B.; Bachu, S., Relative Permeability Characteristics for Supercritical CO_2 Displacing Water in a Variety of Potential Sequestration Zones in the Western Canada Sedimentary Basin. *SPE Journal* **2005,** *SPE 95547*.

33. Rohan, J. A.; Haggerty, D. *Carbonate Special Core Analysis Study for Pennzoil Exploration and Production Company: Elevated Temperature Centrifuge Study*; Technical Report, Westport Technology Center International, IIT Research Institute: 1996.

34. Land, C. S., Calculation of Imbibition Relative Permeability for Two- and Three-phase Flow from Rock Properties. *SPE Journal* **1968,** *SPE 1942*.

35. Raines, M., Kelly-Synder (Cisco-Canyon) Fields/SACROC Unit. In *Oil & Gas Fields in West Texas*, West Texas Geological Society: 2005; Vol. 8, pp 69-78.

36. Famodimu, O. O., Impact of Miscible CO_2 Flooding on HCGOR. *Hart's E & P* **2008,** *81* (6), 66-67.

CHAPTER 4

RATE-DEPENDENT OIL RECOVERY IN

FRACTURED BASEMENT

RESERVOIRS

Justin Wriedt[a], Milind Deo[a], Thomas Doe[b] and Huabing Wang[c]

4.1. Abstract

   In fractured basement reservoirs, oil is primarily stored in fractures, due to impermeability of the host rock. Generally, only large aperture fractures are visible from seismic reflection surveys. However, there may be considerable reserves in subseismic fractures that are not visible from seismic data. An investigation, using a discrete fracture network (DFN) simulator, is undertaken to examine oil and water displacements at varied production rates in a fractured reservoir.

   During waterflooding the displacement of oil from fractures is controlled by gravity, viscous, and inertial forces. In multiphase flow gravitational effects are introduced by the density differences between the fluids. Viscous effects are complex because the relative permeability of each phase depends on saturation, density, and viscosity. Multiphase

a.) Department of Chemical Engineering, 50 Central Campus Drive, University of Utah, Salt Lake City, Utah 84112.; b.) FracMan Technology Group, Golder Associates, Inc. 18300 NE Union Hill Road, Redmond, Washington 98052; c.) iReservoir, 1490 W. Canal Court, Suite 2000, Littleton, Colorado 80120

displacement in fractures is further controlled by fracture dip and by the continuity of flow paths in the direction of buoyant flow. The higher capacity for flow in large aperture seismically-visible fractures can lead to high water production before subseismically-identified fracture oil is recovered. High watercuts observed in two-phase oil-water Type I fractured reservoirs may make oil production economically unrealistic.

It was hypothesized that a lower production rate would recover a higher percentage of oil in place from subseismic fractures while decreasing total water production. This parametric study investigated the effects of threshold capillary pressure, wettability, relative permeabilities, and storage ratios in seismic and subseismic fractures on rate-dependent recovery. Results indicate that in almost all situations a higher rate of production will maximize oil recovery when time is considered. When comparing the pore volumes injected, equivalent recovery is achieved with fewer pore volumes injected for the lower waterflooding rate. In most cases there is delayed water production in low rate waterflooding, however, overall recovery is not increased relative to high rate waterflooding. The hypothetical occurrence of rate-dependent relative permeabilities would make low recovery rates more beneficial, however, there is no known physical basis for rate dependent relative permeabilities in two-phase oil-water systems at this time. The viscous forces in high rate simulations dominate other forces that could potentially reduce recovery. The assumption of Darcy flow in the DFN simulator neglects inertial forces which may become important in large aperture faults if a Reynolds number greater than 1 is achieved at higher rate waterflooding.

Results from this study may be used to develop operational guidelines for waterflooding rates in fractured basement reservoirs where matrix flow and storage volume is negligible. History matching using a DFN simulators can improve the understanding of

subseismic fractures and the flow interaction with seismic fractures.

4.2. Introduction

4.2.1. Background

Naturally fractured reservoirs occur worldwide. Understanding this type of reservoir is important in reservoir engineering applications. These formations contain about 60 percent of the world's remaining petroleum resources. In conventional naturally fractured reservoirs fluid flows in both the matrix and fractures. For those reservoirs the bulk of the fluid volume is contained in the rock matrix and the fractures act as the highly permeable flow conduits. These reservoirs are highly heterogeneous and have complex interactions between the matrix and fractures that can affect oil and gas production.

Optimizing the recovery from fractured reservoirs has become increasingly important for reservoir engineers. Reservoirs where the fracture permeability dominate generally produce less of the reserves than a conventional reservoir where the matrix permeability controls recovery. This causes some difficulty in predicting how completions, water flood patterns and tertiary recovery processes will perform in these fractured reservoirs. Fractures can fundamentally alter reservoir permeability, connectivity and heterogeneity. Characterization of these fracture networks is a vital task in optimal reservoir management.

Fractured reservoirs are usually classified based on how the fracture system enhances the reservoir productivity. A fracture classification was developed [1] which provides geologists and engineers with a fractured model standard. Nelson's four types of fractured reservoirs classification are listed below.

- Type I: Fractures provide the essential reservoir porosity and permeability.

- Type II: Fractures provide the essential reservoir permeability.

- Type III: Fractures enhance permeability in an already producible reservoir.

- Type IV: Fractures are barriers with no additional porosity or permeability.

The first three types describe positive reservoir attributes of the fracture system. The fourth type describe fractures which create flow anisotropy and reservoir partitioning.

This work focuses on fractured basement reservoirs. These are defined as Type I where the faults and fractures provide the porosity and permeability. Geologically, Type I reservoirs are granitic, basalt or other crystalline formations that have low permeability and porosity and do not contribute to oil recovery. Essentially all of the oil within these basement reservoirs resides in the fault zones and fractures. Since almost all of the oil resides in the fracture networks, a discrete fracture network (DFN) model is one of the best ways to characterize a basement type reservoir.

4.2.2. Discrete Fracture Network Simulations

Three common methods are used to model fractured reservoirs: single porosity models, dual porosity models and DFN models. Compared with the other two models, the DFN models the geometry of the fracture network explicitly and provides a realistic way of modeling fractured reservoir performance [2].

Despite their numerical efficiency, dual porosity models have some drawbacks. These are limited to sugar cube representations of fractured media. Shape factors may oversimplify the representation of fluid flow when gravity and viscous effects are involved. A dual porosity model also assumes a dense, closely-connected fractured network and may not be very accurate when treating only a few fractures.

Discrete fracture models are a useful alternative to the single porosity models. In a discrete fracture model, the dimensionality of fractures is reduced from n to (n-1) [3-4]. This

allows a fracture to be modeled as a planar feature with no thickness. The thickness is input separately to create the storage pore volume. This reduction greatly decreases the computational time. Compared to the continuum models, there are many advantages of the DFN model. It accurately accounts for the heterogeneity and orientation of the fracture sets. The performance of the method is not affected by very thin fractures where mesh effects may be problematic when accounting for fracture thickness. DFN models can explicitly account for the effect of even a single fracture on fluid flow and there is no need to compute transfer functions.

4.2.3. Fault and Fracture Characterization

Basement reservoirs are often modeled using maps of faults imaged from seismic reflection information. Only large features are imaged and the reservoir is constructed using these trace maps. In discrete fracture network modeling, significant fractures and faults are represented as discrete features. Smaller scale, or subseismic, fractures cannot be seen in the seismic reflection data. The low frequency seismic waves result in limited detection and resolution scale. During interpretation only large size faults in the basement reservoirs are observed. Smaller subseismic scale features cannot be represented in conventional deterministic modeling [5]. Their locations and characteristics can be inferred from image log interpretation, which are based on resistivity or acoustic methods. Since the fractures, faults, breccias, and alteration zones have low resistivity values, wireline resistivity logs also should be a means of identifying fault zones and altered rock in basement reservoirs. There are numerous well known fault studies that compare geologic logs of fault intersections with resistivity logs.

Characterization of the petrophysical properties of fractured basement reservoirs is also

challenging. It has been reported that there are large variations in oil properties of offshore Vietnam basement reservoirs with depth varied from 1750 to 2440 m [6]. Fracture porosity has also been quantified from well logs in fractured basement reservoirs and used to estimate permeability [7]. Permeability is the most difficult parameter to assess in a reservoir and this is even more challenging in a basement reservoir. Li et. al., 2004, reported a method to quantitatively evaluate a basement reservoir's permeability based on image logs with the integration of other open-hole logs, mud gas data, drilling data, dynamic well testing and production logging data [8].

4.2.4. Motivations

Storage and production of oil from basement reservoirs depends on porosity, permeability, and capillary properties of the material in the faults and fractures. This work addresses several questions related to the production characteristics of fractured basement reservoirs. An attempt is made to determine the influence that subseismic feature permeability has on oil displacement and overall recovery by comparing different permeability ratios between the seismic and subseismic features. This work seeks to identify how oil distributions in seismic/subseismic features affect recovery and water cut behavior. This is an important question in the recovery of oil from basement reservoirs. The distribution of oil in the seismic and subseismic features was varied in these simulations. This study also qualitatively identifies how waterflood injection rate influences ultimate recovery and watercut. This is another important question that relates to the operational controls and reservoir management.

This study systematically varies proportions of storage in the seismic and subseismic fault populations. Its objective is to see whether or not the overall oil recoveries are

sensitive to the distribution of oil between subseismic and seismic faults. The simulations also vary the permeability, porosity, capillary and wettability properties of the seismic and subseismic faults as an additional variable.

The simulation work focused on how production rate affects oil recovery in a heterogeneous fault network. Faults in granitic basements contain heterogeneities at several scales [9]. At a large scale, a basement reservoir has faults that range in thickness from a few centimeters to tens of meters with extents from a few tens of meters to several kilometers including the altered zone. Faults also contain a heterogeneous internal structure, where the flow may be concentrated in a relatively small portion of a fault's thickness, and a major portion of the storage in the fault may lie outside the main flowing channels in brecciated or altered zones.

The issue of heterogeneity at all scales lies at the heart of a production strategy for a fault-dominated basement reservoir. The major portion of the ultimate recovery of the reservoir comes from secondary recovery, generally the displacement of oil by water due to reduced costs. The water source may be either an aquifer or water that is injected for pressure support. In either case, water moving in the flowing portions of the faults may bypass the oil that resides in the altered zone outside the high permeability vuggy and solution enhanced pathways.

Two criteria are used to evaluate the effect of production rate on recoveries. The first is whether a higher or a lower rate water injection will produce a higher ultimate recovery. The answer to this question lies in whether or not the lower rate cumulative oil production curve crosses the higher rate curve, in which case the lower rate produces the higher recovery over time. The second aspect is the water cut. High water cut reduces the economic efficiency of production since there are higher pumping costs per unit volume of

oil and there are increased costs for water handling. A serious consideration for oil production from basement reservoirs is excess water production. This reduces artificial lift efficiency and also causes fines migration formation damage in the oil zones [10]. A detailed study of multiphase flow in basement reservoirs has not been reported.

4.3. Model Development

The numerical models described in this chapter simulate multiphase flow in simple heterogeneous fault networks. These networks domininantly contain a set of more conductive vertical features that represent the seismic faults and intersecting less conductive features representing the subseismic fractures. The simulations addressed the effect of pumping rate on ultimate recovery. The simulations vary the pore volume and permeability contrasts of the seismic and subseismic faults. They also vary the wettability relationships and include horizontal conductors that allow water to surround oil-bearing volumes.

The basic model has two parallel, vertical features that represent seismic faults [Figure 4.1]. A set of 12 vertical subseismic faults lies between the two seismic faults; intersecting the seismic faults orthogonally. This is the base case model. A later variation on this model adds three horizontal faults at different depths between the seismic faults. As a check on the effect of a more heterogeneous geometry, we also used a simple random network of fractures in a vertical slab region.

Sandia Laboratory's Cubit was utilized for all domain meshing. Uniform coarse mesh size was used for the seismic and subseismic features for all domains. Triangular meshing is required in control volume finite element (CVFE) simulators for fault and fracture features where they are reduced dimensionally.
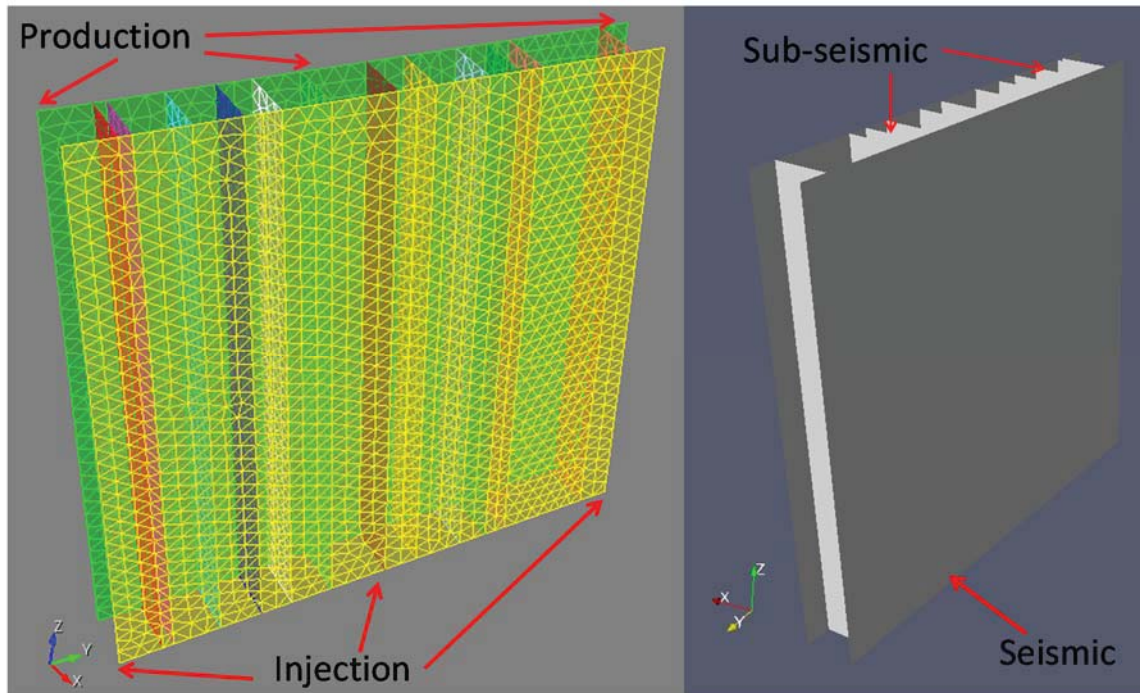
Figure 4.1: Simple model showing seismic and subseismic fractures with triangular meshing.

Simulations were performed using Utah Finite Element Simulator (UFES) version 2.0, a CVFE simulator developed at the University of Utah. This CVFE formulation has been validated and verified through indexing methods [11], a manufactured solution method [3-4], and core-scale verifications with fracture water level experiments [11-12]. The flux-based upstream-weighting function in CVFE discretization formulation is good at handling rotatable permeability tensor which is critical for dimension reduction. This makes the direct accurate simulation of DFN modeled fractured basement reservoir possible. The Black Oil module was used for all simulations, this assumes homogenous oil properties.

The fluid properties used in multiphase simulations, including fluid viscosity, compressibility, density, and formation volume factor, have an important effect on the results. The properties used in the simulations are listed in Table 4.1. Linear relative

Table 4.1: Simulation properties which were held constant for all scenarios

Simulation Properties		
Fluid Properties	**Water**	**Oil**
Density (lbf/ft^3)	62.4	52.9
Reference pressure (P_{ref}) [psi]	14.7	14.7
Formation volume factor (B_r) [rb/stb]	1.00	1.17
Compressibility C_B [psi^{-1}]	3.25E-06	1.0E-06
Viscosity (μ_r) [cp]	0.3	1.0
C_μ [psi^{-1}]	0.0	0.0
Initial Conditions		
Pressure (P_0) [psi]	3300	3300
Saturation (S_f)	0.001	0.999

* Pressure related reservoir fluid properties are calculated using equations 4.1 & 4.2

$$B = B_r exp[-C_B(P - P_{ref})] \qquad [4.1]$$

$$\mu = \mu_r exp[-C_\mu(P - P_{ref})] \qquad [4.2]$$

permeability curves are used as the base case [13]. Different capillary pressure curves were used throughout the simulations and were exaggerated in some cases to investigate the effect of these forces. Initial water saturation is assumed to be nearly 100 percent. In this model, we assume that both seismic and subseismic features have constant porosity and thickness. The vertical seismic fractures are 2906.8 ft (886 m) wide and 2906.8 ft (886 m) in height. The subseismic fractures are 328 ft (100 m) wide and 2906.8 ft (886 m) high. All models have a total pore volume of 3,000,802 ft^3 to allow for one pore volume to be

displaced in a reasonable amount of time. Constant injection and production rates were used throughout and adjusted using the values in Table 4.1. Water was injected along the entire base of the vertical seismic features. Production wells were placed along the top of the vertical seismic fractures. No oil is produced directly from the subseismic fractures; it is expected that completions would be in the faults in practice.

4.4. Results and Discussion

4.4.1. Simple Model

4.4.1.1. Base Case

A base case was developed with parameters that are varied systematically [Table 4.2]. The base case model had a permeability ratio of 100 to 1 between the seismic and subseismic fractures, respectively. Twenty percent of the total pore volume was stored in the seismic fractures and 80 percent in the subseismic. Straight line relative permeability curves were assigned to all fractures with no residual saturations. Six injectors and producers are positioned at the corners and center of the seismic fractures along the top and bottom. It is assumed for the base case that there is no capillary pressure in the fractures.

4.4.1.2. Permeability Contrast

Permeability contrast was modified to assess the effects on overall recovery in fractured reservoirs. The permeability in the subseismic fractures was increased and decreased by two orders of magnitude to determine the effects on overall recovery. The change in recovery rate after water breakthrough is dictated by the subseismic permeability. Where the subseismic permeability is high the rate is high, whereas low subseismic permeability has an abrupt change in the recovery rate once the seismic features are swept of all oil. For

Table 4.2: Property table for the simple model varied cases

Simple Model Simulation Properties								
	Seismic Features				Sub-seismic Features			
Scenario Name	Injection Rate (bbl/day)	Permeability (mD)	Pore Volume (%)	Wettability	Permeability (mD)	Pore Volume (%)	Wettability	Capillary Pressure Curve
SMBCH	37739.0	10000	20	oil	100	80	oil	none
SMBCL	3773.9	10000	20	oil	100	80	oil	none
SMKR1H	37739.0	10000	20	oil	10000	80	oil	none
SMKR1L	3773.9	10000	20	oil	10000	80	oil	none
SMKR2H	37739.0	10000	20	oil	1	80	oil	none
SMKR2L	3773.9	10000	20	oil	1	80	oil	none
SMPV1H	37739.0	10000	5	oil	100	95	oil	none
SMPV1L	3773.9	10000	5	oil	100	95	oil	none
SMPV2H	37739.0	10000	1	oil	100	99	oil	none
SMPV2L	3773.9	10000	1	oil	100	99	oil	none
SMWWH	37739.0	10000	20	water	100	80	water	none
SMWWL	3773.9	10000	20	water	100	80	water	none
SMOWWH	37739.0	10000	20	oil	100	80	water	none
SMOWWL	3773.9	10000	20	oil	100	80	water	none
SMPC1H	37739.0	10000	20	oil	100	80	oil	2
SMPC1L	3773.9	10000	20	oil	100	80	oil	2
SMPC2H	37739.0	10000	20	oil	100	80	oil	1
SMPC2L	3773.9	10000	20	oil	100	80	oil	1

all scenarios this generated lower recovery at early times with greater water production

between the high and low rate [Figure 4.2a]. Ultimately the overall recovery was the same

for the low and high rate cases for all scenarios. The recovery from the seismic fracture is

relatively equivalent for the initial pore volumes injected. However, there is variation in

recovery rate after breakthrough relative to pore volumes injected based on subseismic

fracture permeability [Figure 4.2b]. The water cut breakthrough for the three scenarios is

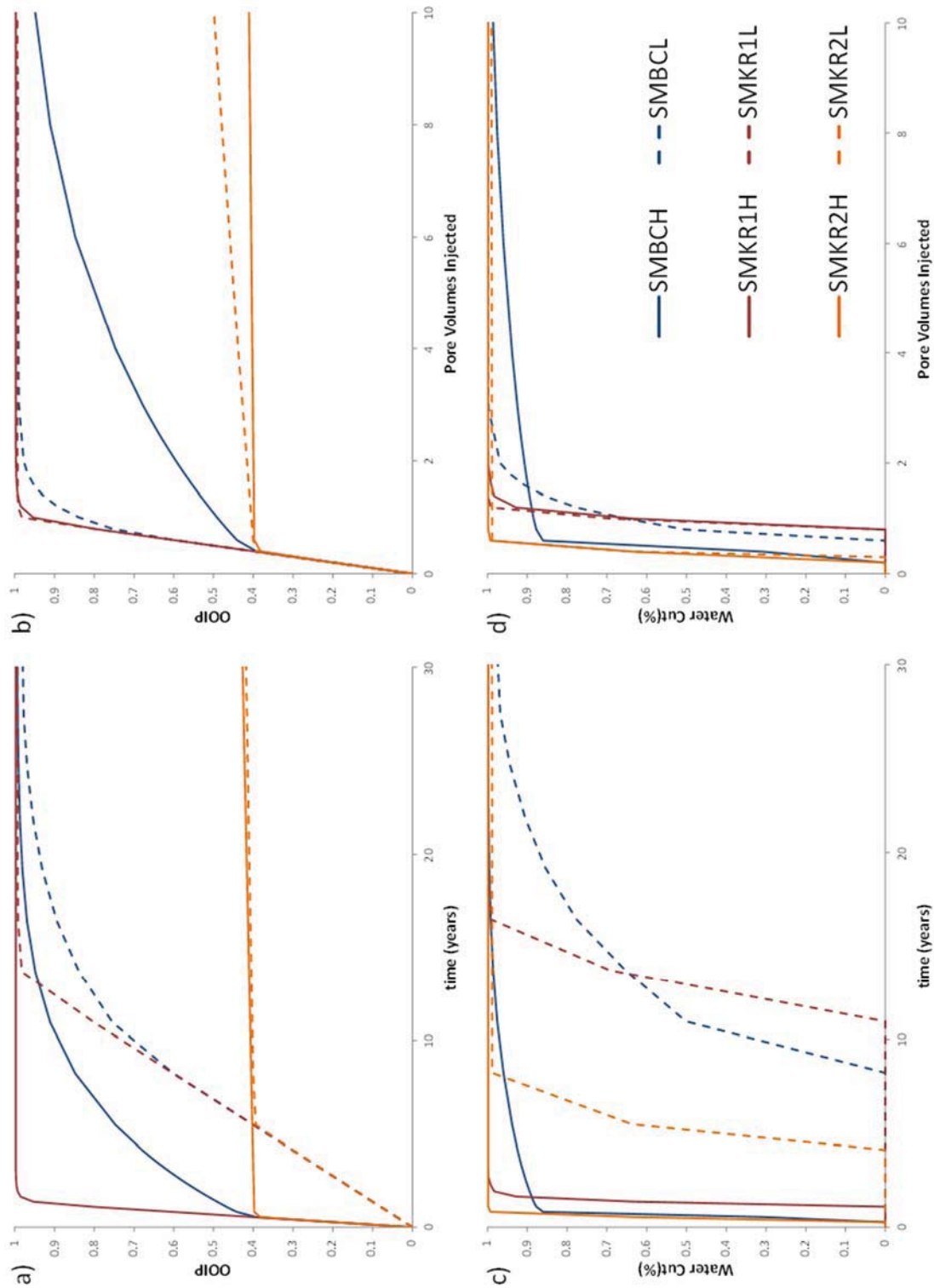dictated by the seismic fracture permeability [Figure 4.2c,d].

Figure 4.2: Comparison of recoveries and watercut by varying permeability ratios for the simple model. (a) Fraction OOIP vs. time (b) Fraction OOIP vs. pore volumes injected (c) Watercut vs. time (d) Watercut vs. pore volumes injected.

4.4.1.3. Pore Volume Comparison

A comparison was made by varying the storage ratios of OOIP within the seismic and subseismic features. The ratios were adjusted while keeping the total pore volume equal to the base case. The volumes were reduced for the seismic and increased for the subseismic fractures. Overall, the higher the percentage of storage within the seismic fractures, the higher the overall recovery [Figure 4.3a]. Oil recovery is higher relative to pore volumes of water injected for all cases [Figure 4.3b]. Reducing the seismic feature pore volume reduces the time until water breakthrough, which indicates higher recovery at early time with the same ultimate recovery [Figure 4.3c]. The low rate cases all have higher water cut percentage relative to pore volumes injected for the pore volume storage comparison [Figure 4.3d].

4.4.1.4. Wettability Comparison

Wettability of the host rock could affect how oil is recovered from fractures. A comparison is made using oil-wet and water-wet scenarios. The base case is assumed to be oil wet. One modified case is simulated with all features water wet and another is simulated with water wet properties in the seismic features and oil wet properties in the subseismic fractures. The oil recovery rate in all three cases is dictated by the subseismic features, where oil recovery rates are equivalent until water breakthrough occurs [Figure 4.4a]. The water wet case has higher oil recovery at the time of breakthrough, where more oil is recovered from the subseismic fractures on initial sweep due to their wettability. The initial recovery is lower relative to pore volumes injected but overall recoveries are equivalent [Figure 4.4b]. The scenario with water-wet subseismic features has the most delayed water breakthrough, however, the case with oil-wet seismic combined with water-

Figure 4.3: Comparison of recoveries and watercut by varying pore volume storage ratios for the simple model. (a) Fraction OOIP vs. time (b) Fraction OOIP vs. pore volumes injected (c) Watercut vs. time (d) Watercut vs. pore volumes injected.
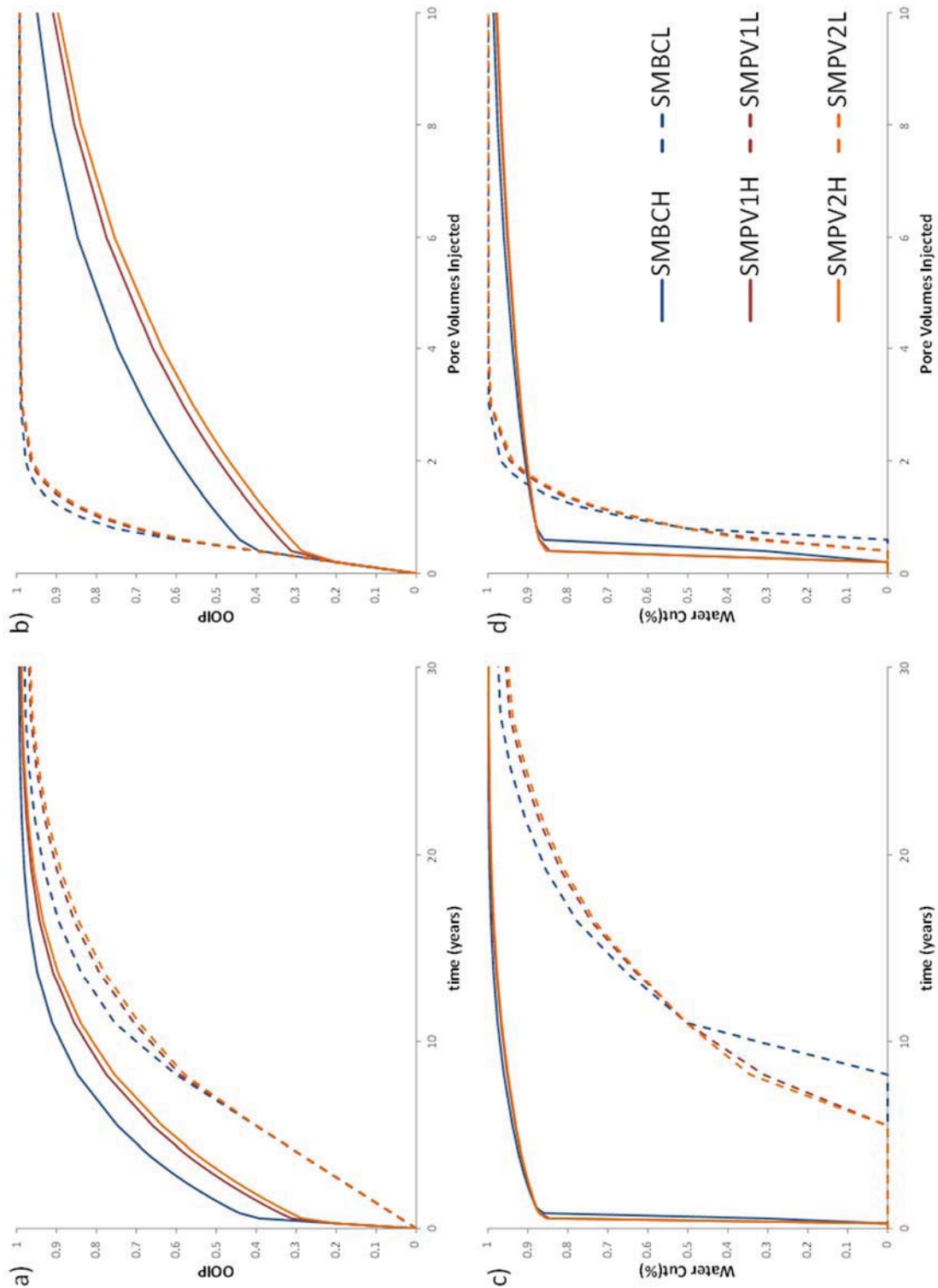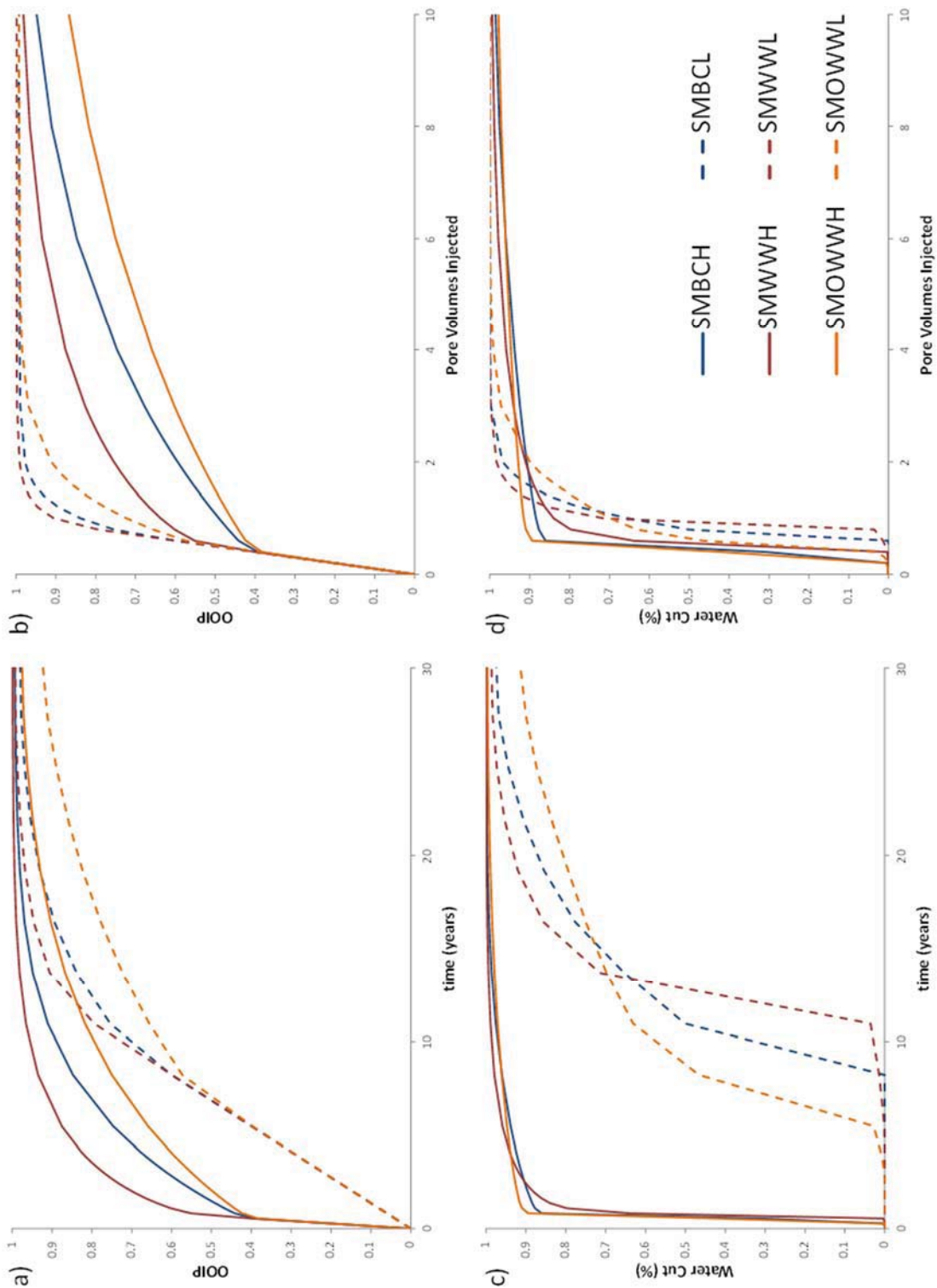
Figure 4.4: Comparison of recoveries and watercut by varying wettability for the simple model. (a) Fraction OOIP vs. time (b) Fraction OOIP vs. pore volumes injected (c) Watercut vs. time (d) Watercut vs. pore volumes injected.

wet subseismic have the lowest overall water cut [Figure 4.4c,d].

4.4.1.5. Capillary Pressure Comparison

Capillary pressure was applied to subseismic fractures to determine how oil recovery would be affected. Both low and high value threshold capillary pressure curves for the subseismic fractures were used for comparison to the base case. Overall recovery is less in the model with capillary pressure where the high threshold capillary pressure has a significant effect on overall recovery [Figure 4.5a]. The effect of capillary pressure results in lower recovery initially, followed by higher recovery, with lower overall recovery relative to the base case. The high threshold capillary pressure scenario always has significantly lower oil recovery initially than the other low rate cases. Ultimately the other two cases achieve the same overall recovery as the high threshold capillary pressure scenario. The time to water breakthrough is dictated by the threshold pressure. The lower threshold pressure has little effect relative to the base case initially, however, the rate is affected after breakthrough occurs [Figure 4.5c,d].

4.4.1.6. Observations

For this simple fracture system, where the properties of each of the fracture sets are homogeneous, some observations can be made. There is significant impact on recovery by the permeability of the subseismic features. Lower subseismic permeabilities result in lower recoveries and quicker breakthroughs for the same injection rates.

In reservoirs with significant vertical extent, the displacement of oil by water is gravity dominated due to the density differences between the fluids. The relative magnitude of the gravity forces with respect to the viscous forces is defined by the dimensionless gravity
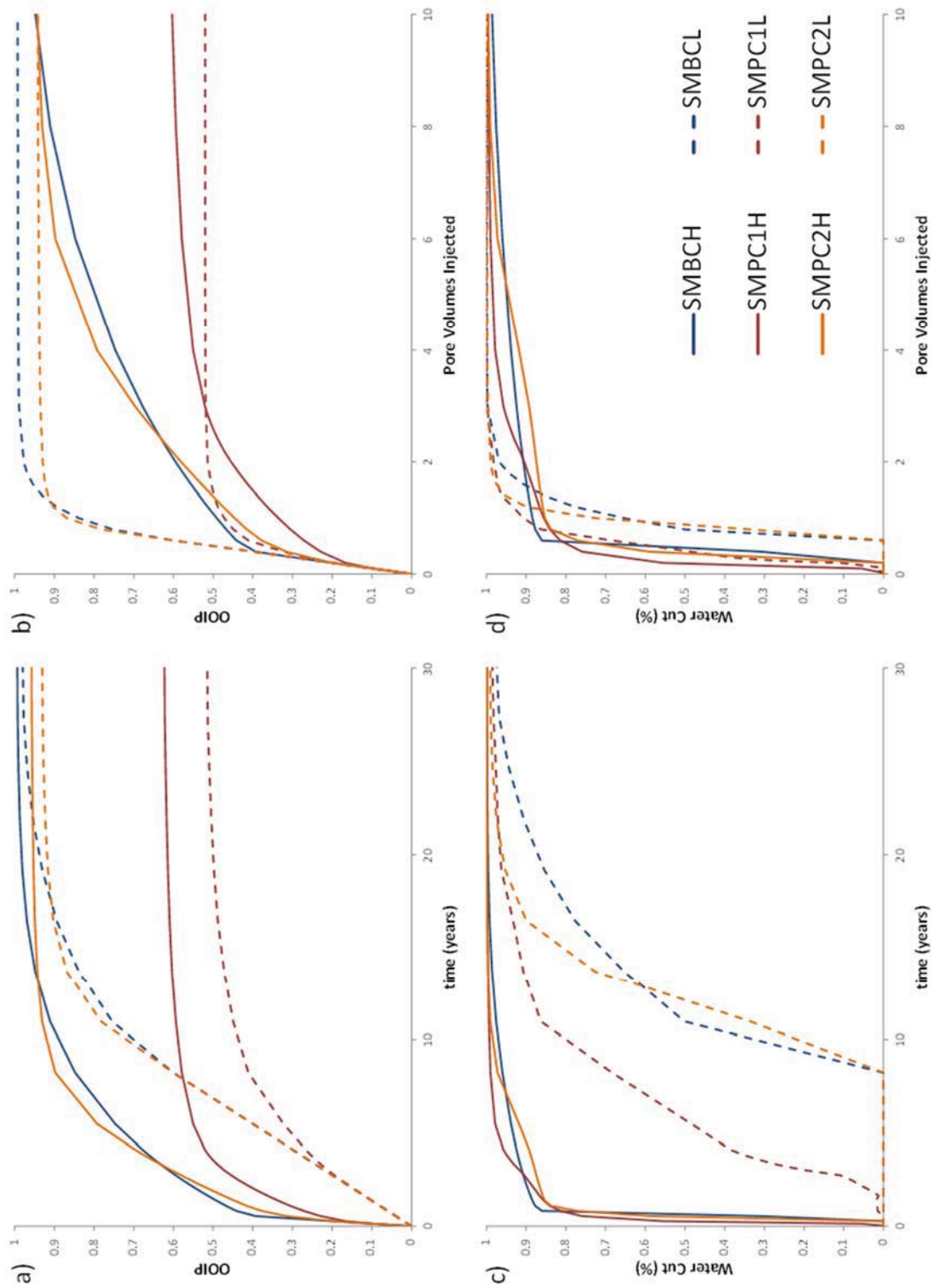
Figure 4.5: Comparison of recoveries and watercut by varying capillary pressure for the simple model. (a) Fraction OOIP vs. time (b) Fraction OOIP vs. pore volumes injected (c) Watercut vs. time (d) Watercut vs. pore volumes injected.

number, also known as the buoyancy number [Equation 4.3] [14-15].

$$N_G = \frac{\Delta\rho.g.\text{k}/\varphi}{\mu_o.v} \qquad [4.3]$$

where $\Delta\rho$ is the fluid density difference, g is the gravitational constant, k is permeability, φ is porosity, μ is viscosity of oil and v is fluid velocity.

In general, as the gravity number increases the recovery in gravity dominated systems also increases. This assumes that sufficient time is available for buoyancy forces to take effect. As the system permeability decreases, so do the gravity number and the recovery decreases. As the injection rate, and thus velocity, increases the gravity number is decreased. The reduction of injection rate in these studies is not sufficient to significantly reduce the overall recoveries significantly.

4.4.2. Horizontal Fracture Model

In fractured systems it has been shown that gravitational pressure governs displacement when the block height is considerably larger than the capillary height [16]. Alternatively, capillary pressure governs displacement when the blocks heights are very small, which can be described by the dimensionless Bond number [Equation 4.4].

$$N_B = \frac{\Delta\rho.g.\text{L}^2}{\sigma} \qquad [4.4]$$

where $\Delta\rho$ is the density difference between the reservoir fluids, g is the gravitational

constant, L is the characteristic length and σ is surface tension.

Horizontal seismic fractures are added to the original domain to disrupt the continuous fluid column in the subseismic fractures. Reducing the column height effectively reduces the characteristic length, therefore reducing the Bond number. It is posited that if the water in the vertical seismic fractures moves past the horizontal seismic fractures at a high rate, the bypassed oil in the subseismic fractures would become trapped due to capillary forces. However, if the production rate of the reservoir is reduced then it may be possible that additional oil can be recovered from the subseismic fractures by increasing the gravity number relative to the Bond number.

These simulations are modifications to the simple model that include high-conductivity horizontal seismic features [Figure 4.6]. There are two vertical seismic fractures, three horizontal seismic fractures, and 12 vertical subseismic fractures. The subseismic fractures are orthogonal to the vertical seismic fractures. There are six injection wells, three at the base of each vertical seismic fault, and six production wells, with three intersecting the top of the vertical seismic features. Three high permeability horizontal fractures cut across the subseismic faults creating connections between the two seismic faults. The horizontal seismic faults have the same properties as the vertical seismic faults.

4.4.2.1. Base Case Comparison

The base case horizontal fracture model had a permeability ratio of 100 to 1 between the seismic and subseismic fractures, respectively. Twenty percent of the total pore volume was distributed in the seismic fractures, with 7 percent in the vertical and 13 percent in the horizontal, and 80 percent in the subseismic. Straight line relative permeability curves were assigned to all fractures with no residual saturations. Six injectors and producers are
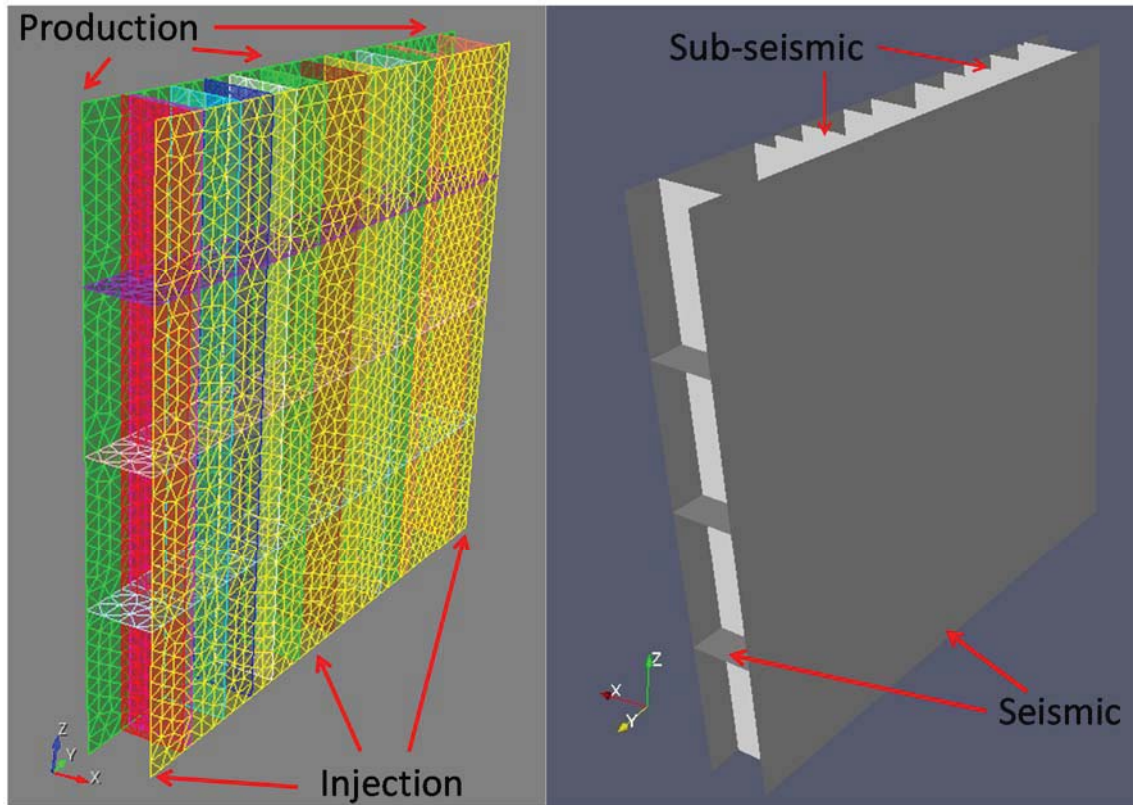
Figure 4.6: Horizontal fracture model showing seismic and subseismic fractures with triangular meshing.

positioned at the corners and center of the seismic fractures along the top and bottom. It is assumed for the base case that there is a threshold capillary pressure in the subseismic fractures and no capillary pressure in the seismic fractures. A summary table of the properties for all cases, with the geometry, flow, and reservoir properties, for the varied simulations is included [Table 4.3].

A comparison of the simple model and horizontal fracture model is made to determine the effects of the horizontal fractures without capillary pressure in the subseismic features [Figure 4.7a - d]. The total pore volume of the subseismic fractures between the two models is identical. In order to accommodate the horizontal seismic fractures the vertical seismic pore volume in the horizontal fracture model was reduced to keep the total pore

Table 4.3: Property table for the horizontal fracture model varied cases.

| Horizontal Fracture Model Simulation Properties | | | | | | | | |
| Seismic Features | | | | | Sub-seismic Features | | | |
Scenario Name	Injection Rate (bbl/day)	Permeability (mD)	Pore Volume (%)	Wettability	Permeability (mD)	Pore Volume (%)	Wettability	Capillary Pressure Curve
3HBCH	37739.0	10000	20	oil	100	80	oil	1
3HBCL	3773.9	10000	20	oil	100	80	oil	1
3HKR1H	37739.0	10000	20	oil	10000	80	oil	1
3HKR1L	3773.9	10000	20	oil	10000	80	oil	1
3HKR2H	37739.0	10000	20	oil	1	80	oil	1
3HKR2L	3773.9	10000	20	oil	1	80	oil	1
3HPV1H	37739.0	10000	5	oil	100	95	oil	1
3HPV1L	3773.9	10000	5	oil	100	95	oil	1
3HPV2H	37739.0	10000	1	oil	100	99	oil	1
3HPV2L	3773.9	10000	1	oil	100	99	oil	1
3HWWH	37739.0	10000	20	water	100	80	water	1
3HWWL	3773.9	10000	20	water	100	80	water	1
3HOWWH	37739.0	10000	20	oil	100	80	water	1
3HOWWL	3773.9	10000	20	oil	100	80	water	1
3HPC1H	37739.0	10000	20	oil	100	80	oil	2
3HPC1L	3773.9	10000	20	oil	100	80	oil	2
3HPC2H	37739.0	10000	20	oil	100	80	oil	none
3HPC2L	3773.9	10000	20	oil	100	80	oil	none
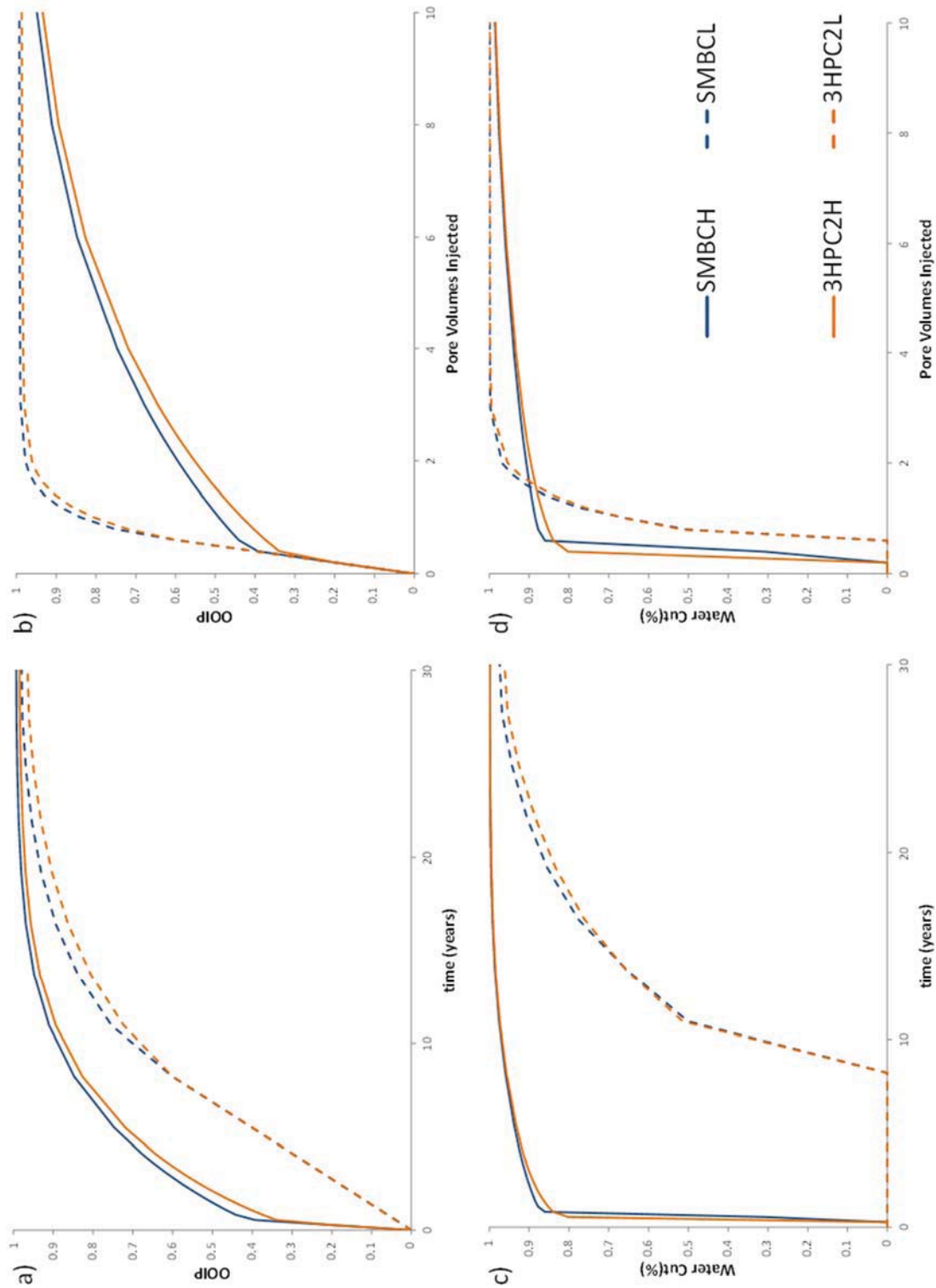
Figure 4.7: Comparison of recoveries and watercut for the simple model and horizontal fracture base case models without capillary pressure in the subseismic features. (a) Fraction OOIP vs. time (b) Fraction OOIP vs. pore volumes injected (c) Watercut vs. time (d) Watercut vs. pore volumes injected.

volume equivalent between the two models. The recoveries between the two scenarios is nearly equal, however, there is some delay in recoveries due to the lower storage in the vertical seismic fractures.

When the two models are compared with capillary pressure in the subseismic fractures the results are quite different. The overall recovery is lower for the horizontal fracture base case relative to the simple model base case with threshold capillary pressure [Figure 4.8a,b]. Water breakthrough occurs sooner for the horizontal fracture case compared to the simple model base cases [Figure 4.8c,d].

As predicted, oil is trapped due to the capillary pressures below the horizontal seismic fractures for the high and low rate cases. However, less oil is trapped in the high rate case where the viscous forces are able to overcome the trapping forces [Figure 4.9]. This phenomenon can be explained by the dimensionless capillary number [Equation 4.5], which is the ratio of viscous to capillary forces. The threshold to overcome the capillary force is found between the high and low injection rates when N_c greater than 1.

$$N_C = \frac{\mu.v}{\sigma} \qquad [4.5]$$

where μ is the fluid viscosity, v is the fluid velocity and σ is surface tension.

4.4.2.2. Permeability Contrast

The ratio of seismic permeability to subseismic fracture permeability was varied to determine whether additional recovery would occur in low rate cases. Ratios of 1:1 and 10000:1 were compared to the base case with a 100:1 ratio. Higher recovery at early times occurs relative to the base case when the permeability of the subseismic fractures is highest.
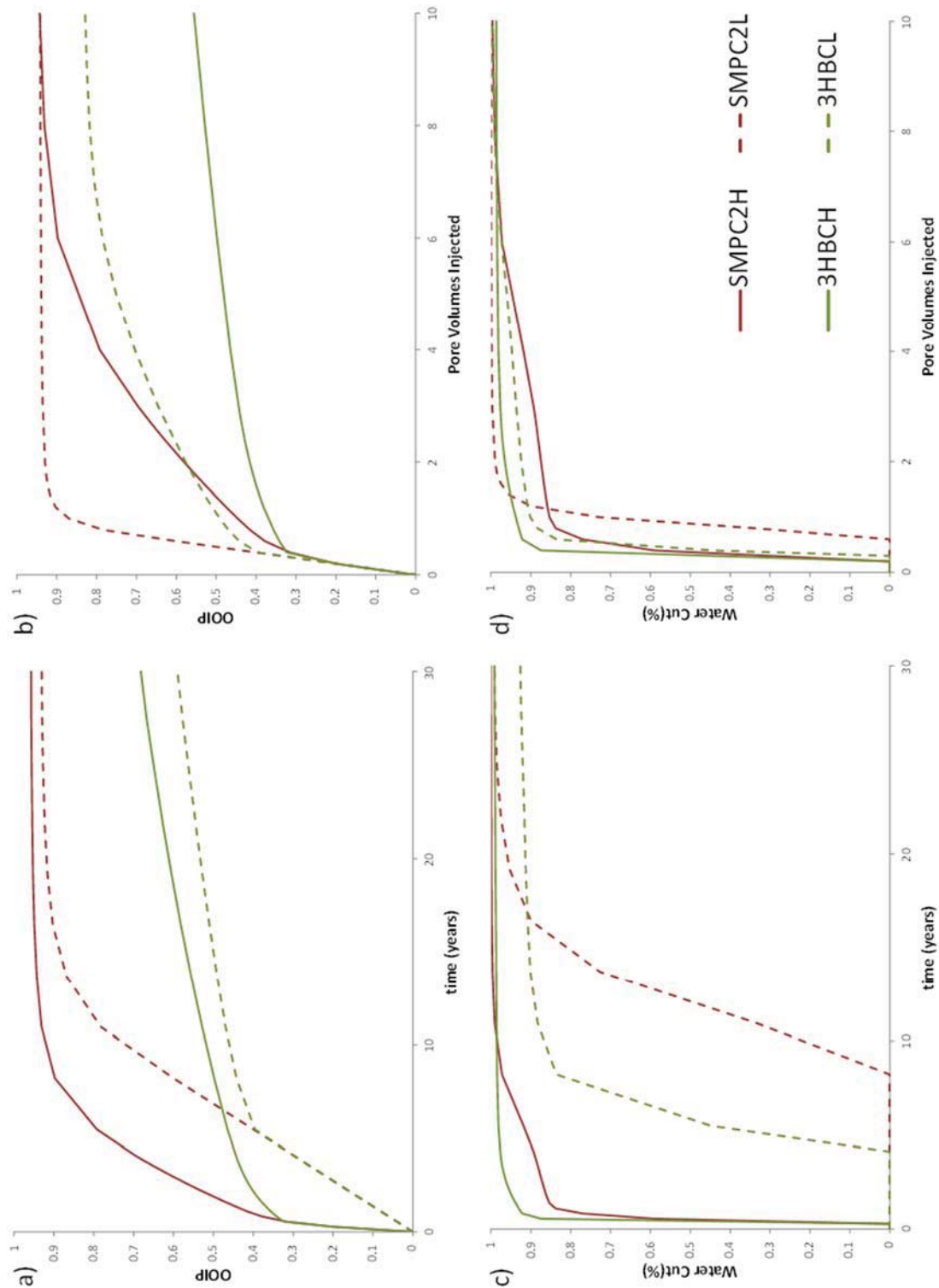
Figure 4.8: Comparison of recoveries and watercut for the simple model and horizontal fracture base case models with capillary pressure in the subseismic features. (a) Fraction OOIP vs. time (b) Fraction OOIP vs. pore volumes injected (c) Watercut vs. time (d) Watercut vs. pore volumes injected.
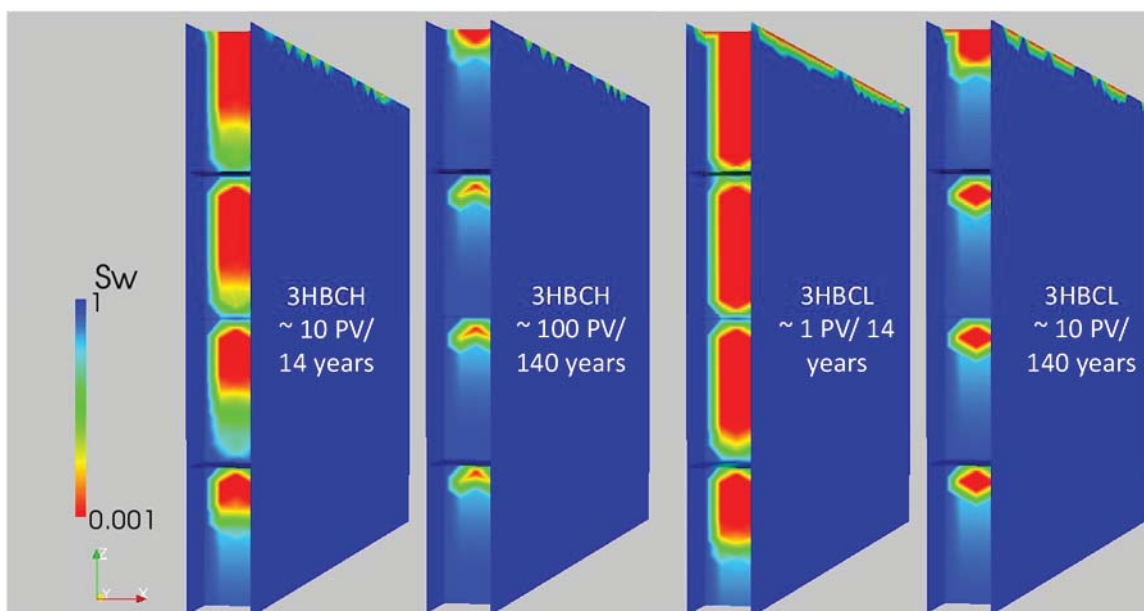
Figure 4.9: Visualization of the recovered oil and water saturations in the horizontal fracture model for the high and low rate base cases after equivalent pore volumes (10 PV) and times (140 years).

There is significant bypass trapping when the seismic fractures have a permeability five orders of magnitude greater than the subseismic ones. The initial gradient in the recovery plot is controlled by the seismic fracture permeability up to approximately 0.32 fraction OOIP [Figure 4.10a]. For all scenarios this generated lower recovery at early times with greater water production between the high and low rate. The low rate injection rate recovers less oil for all cases relative to the high rate due to the higher viscous forces. [Figure 4.10b]. The watercut rate after breakthrough for the low rate cases appears to be controlled by the subseismic permeability, where the initial breakthrough time is the same for the 10000:1 and 100:1 but the rate after breakthrough is different. [Figure 4.10c,d]. The 1:1 permeability ratio case has a delayed watercut as the subseismic fractures are flushed at the same rate as the seismic, which also leads to 99 percent watercut at an earlier time as well.
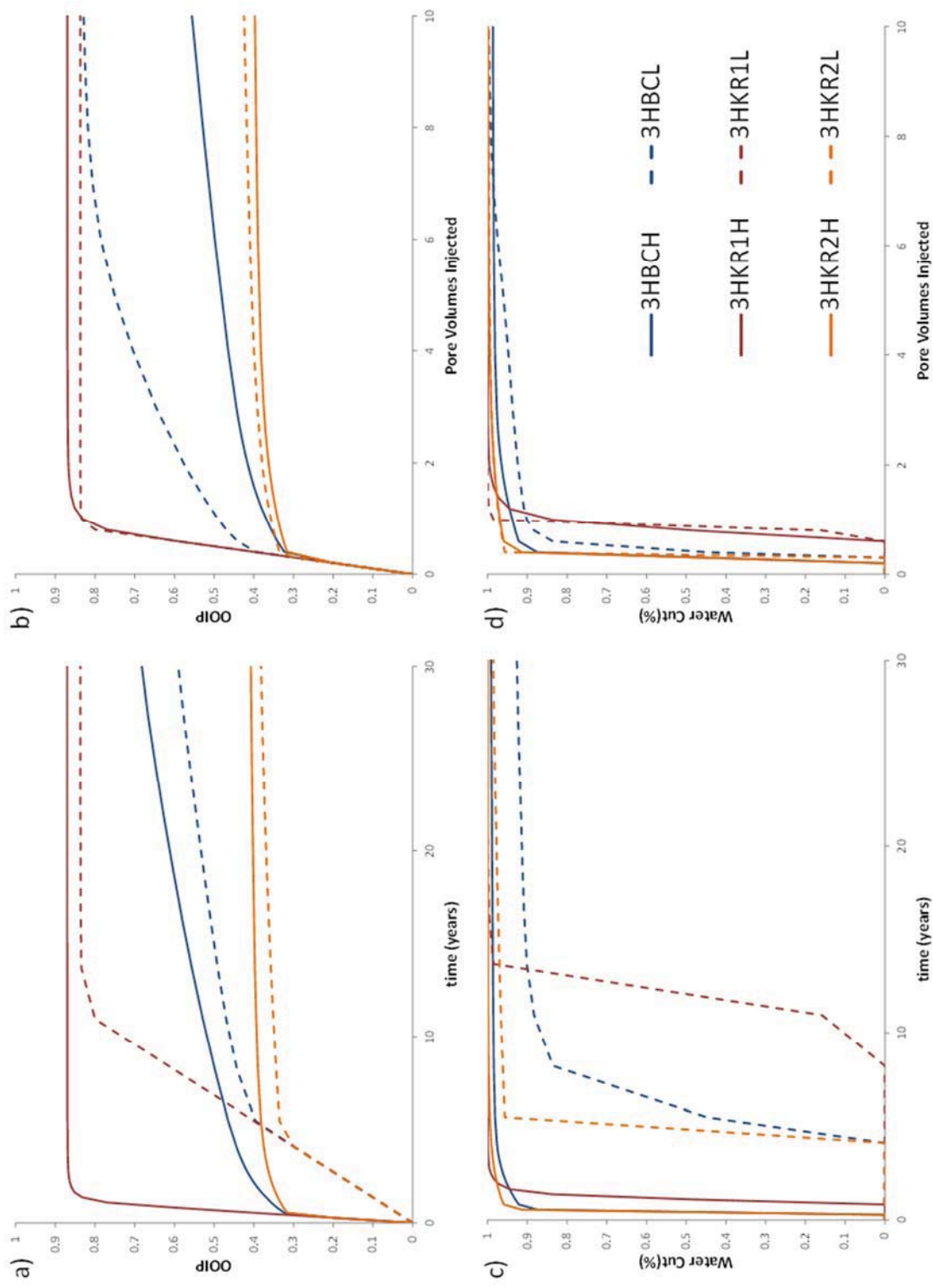
Figure 4.10: Comparison of recoveries and watercut by varying permeability ratios for the horizontal fracture model. (a) Fraction OOIP vs. time (b) Fraction OOIP vs. pore volumes injected (c) Watercut vs. time (d) Watercut vs. pore volumes injected.

4.4.2.3. Pore Volume Comparison

Similar to the simple mode the ratio of pore volumes between seismic and subseismic are decreased to analyze the differences in overall recovery with respect to time. The seismic pore volume is reduced to 5 percent and 1 percent and compared to the base case of 20 percent. A threshold capillary pressure is applied to the subseismic fractures in all cases. The total recovery overall decreases as seismic fracture storage is reduced [Figure 4.11a,b]. The high and low cases for each ratio move toward the same ultimate recovery as the storage volume of the seismic fractures is reduced. Overall the watercuts are similar between the scenarios, however, the low rate has considerably less water production than the high rate cases [Figure 4.11c,d].

4.4.2.4. Wettability Comparison

For the horizontal fracture model a comparison is made using oil-wet and water-wet relative permeability curves [Figure 4.12a - d]. Similar to the simple model the base case is assumed to be oil wet. Modified cases with all fractures water wet, as well as a case where seismic features are water wet and subseismic fractures are considered oil wet are investigated. The wettability in the horizontal fracture model does not have any considerable differences compared to the simple model other than reduced recoveries due to capillary trapping.

4.4.2.5. Capillary Pressure Comparison

An investigation of the magnitude of subseismic capillary pressure was undertaken. In addition to the base case, a scenario with an order of magnitude higher threshold pressure, as well as a case with no capillary pressure were compared. The case with no capillary
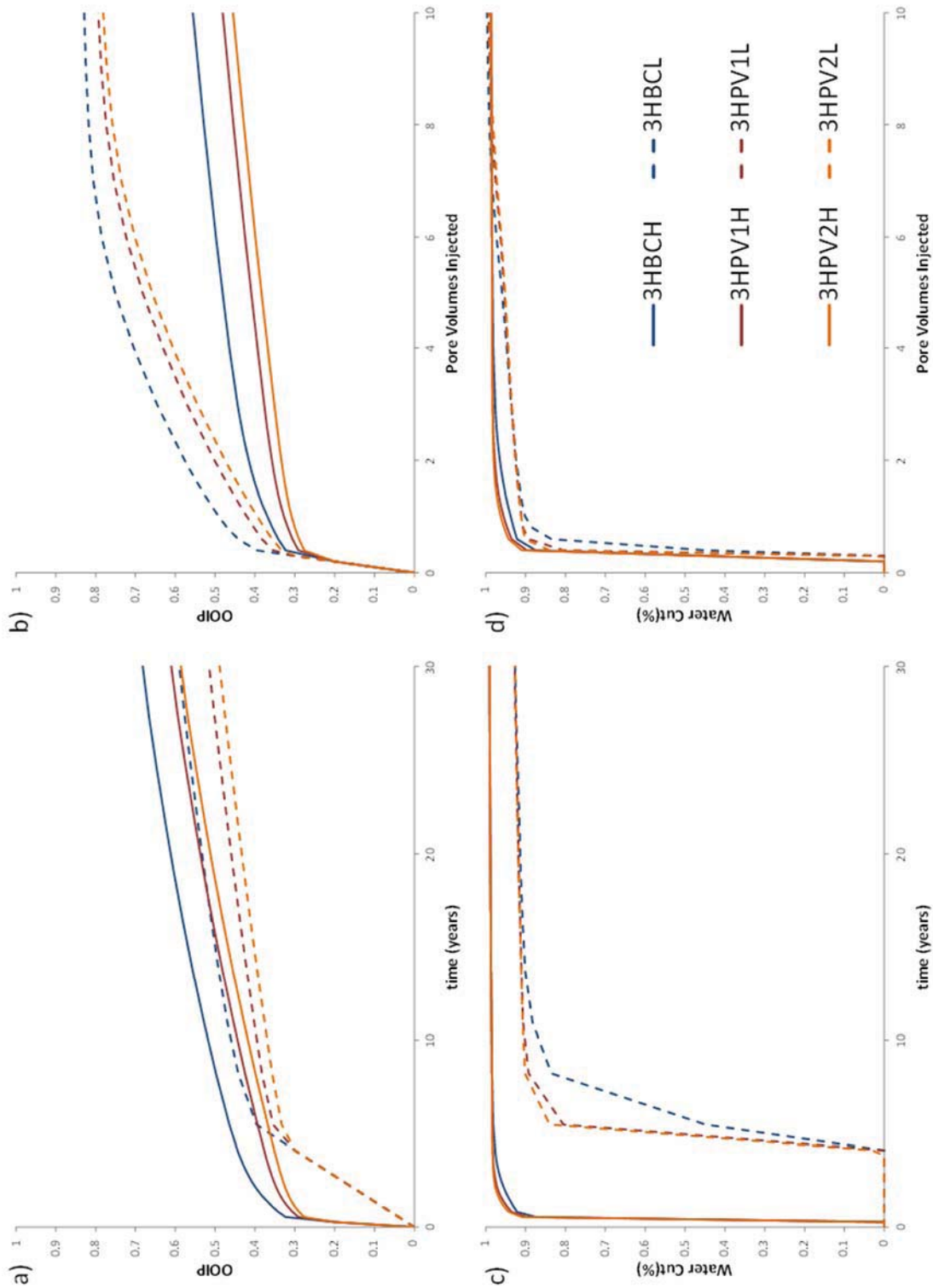
Figure 4.11: Comparison of recoveries and watercut by varying pore volume storage ratios for the horizontal fracture model. (a) Fraction OOIP vs. time (b) Fraction OOIP vs. pore volumes injected (c) Watercut vs. time (d) Watercut vs. pore volumes injected.
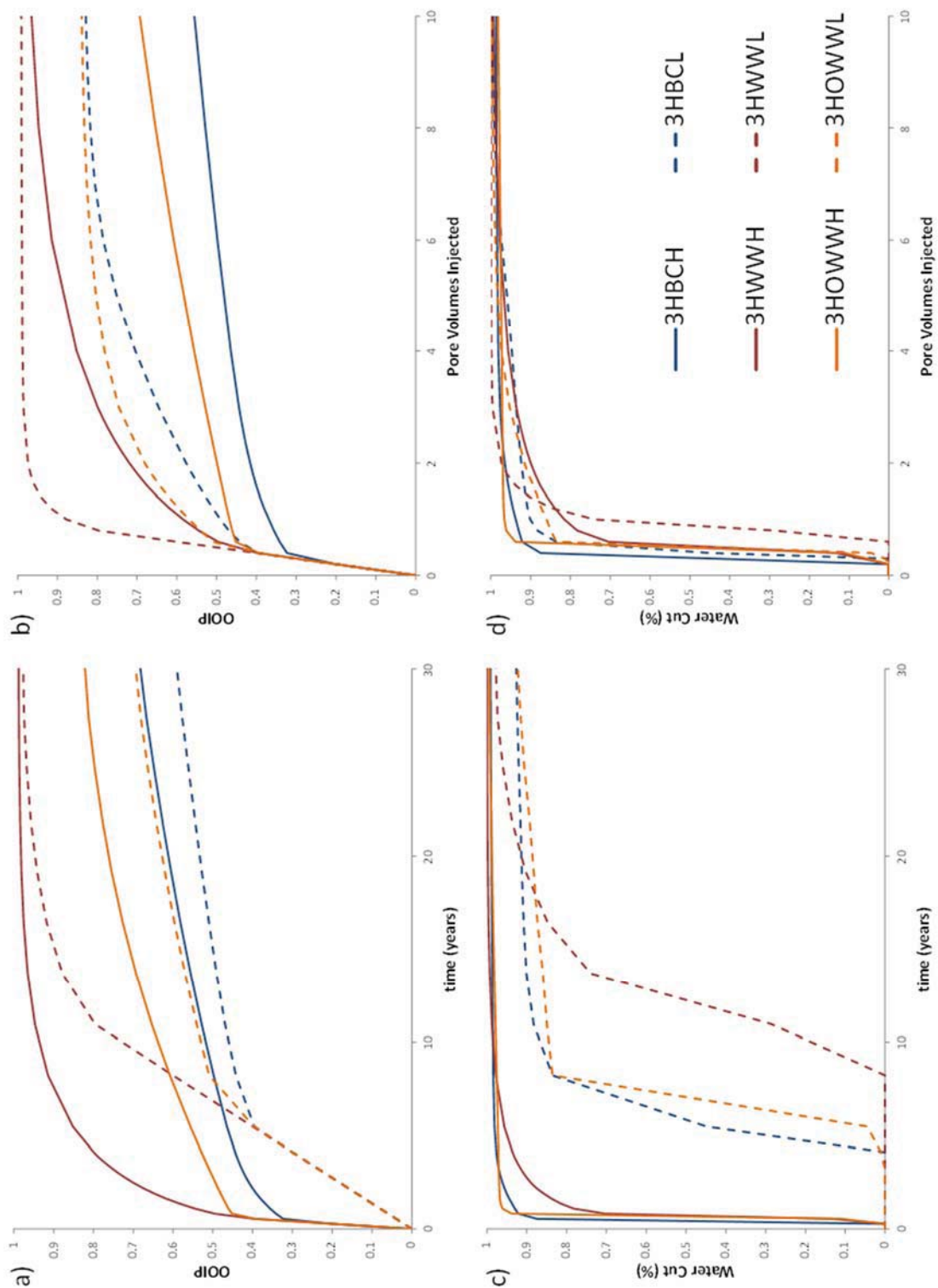
Figure 4.12: Comparison of recoveries and watercut by varying wettability for the horizontal fracture model. (a) Fraction OOIP vs. time (b) Fraction OOIP vs. pore volumes injected (c) Watercut vs. time (d) Watercut vs. pore volumes injected.

pressure achieves nearly equal overall recoveries [Figure 4.13a,b]. For the high capillary pressure case, the overall recoveries were also equal but reached the maximum recovery at a much earlier time. The capillary pressure in the subseismic fractures leads to earlier water breakthroughs and the overall watercut is controlled by the magnitude of the capillary pressure [Figure 4.13c,d].

4.4.2.6. Observations

As expected trapping occurs below the horizontal fractures at different amounts depending on the simulated parameters. Nearly all simulations reach a steady state or upper limit recovery amount that is only produced at very limited increments. It is possible to explain the recoveries, or the ability of the higher rate to producer higher oil volumes, using the dimensionless capillary equation.

4.5. Rate Dependent Relative Permeability Comparison

This comparison investigates the effect of rate-dependent relative permeabilities, where the high rate case curves are different than the low rate case [Figure 4.14]. It is hypothesized that the higher production rate will alter the relative permeability system. It is well known that flow structures can occur in flow where there is large density and viscosity contrasts, such as gas-water systems. These results show that if there is indeed a rate dependence on relative permeability and the end point that lower recovery will have a higher ultimate recovery [Figure 4.15]. These cases are the same as the capillary pressure cases (3HPC2H/L) with the exception that the high rate does not use the linear relative permeability curves. The first case (3HRP1H) has the modified relative permeability in only the seismically identified fractures, whereas the second case (3HRP2H) is only in the
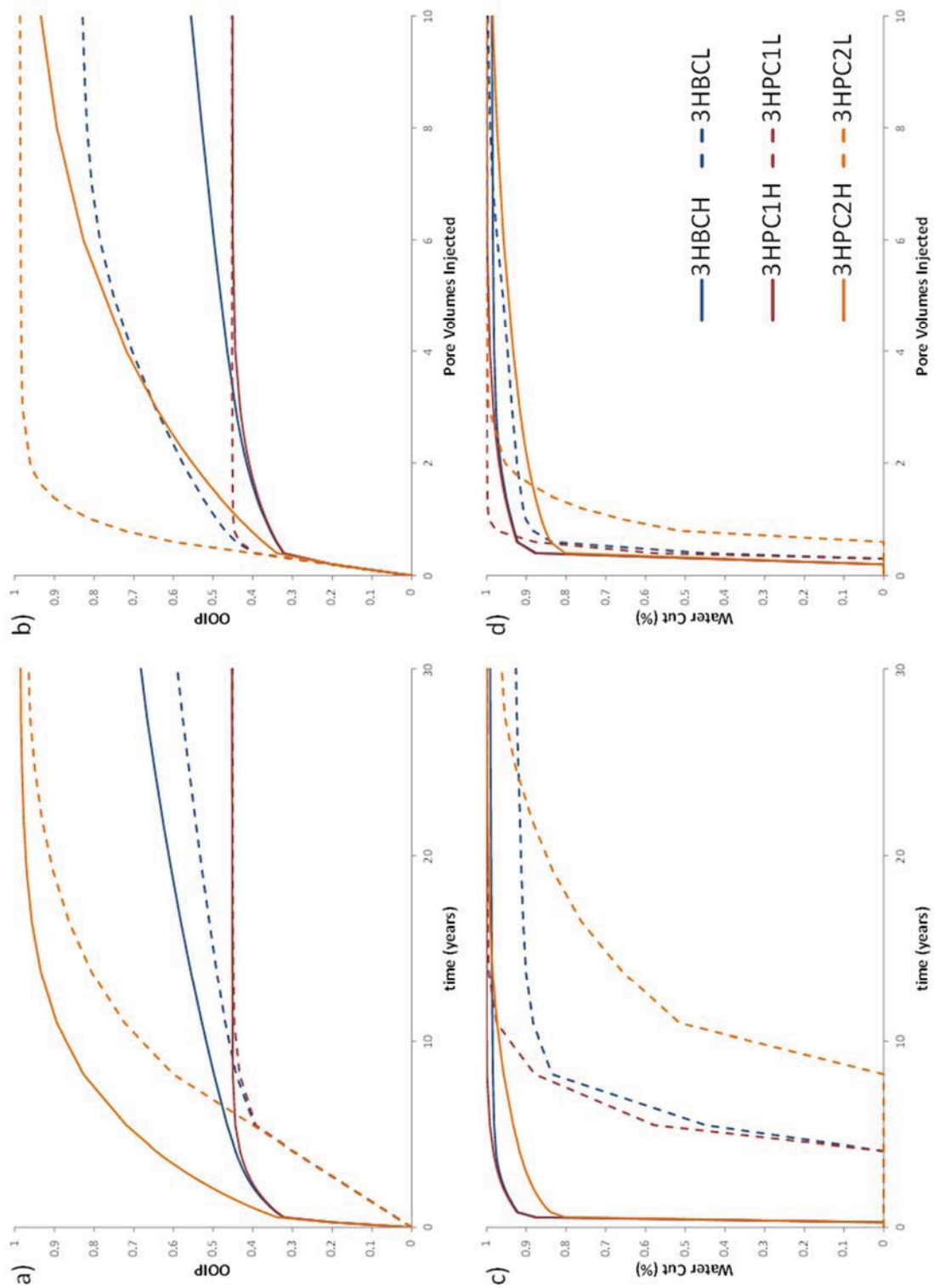
Figure 4.13: Comparison of recoveries and watercut by varying capillary pressure for the horizontal fracture model. (a) Fraction OOIP vs. time (b) Fraction OOIP vs. pore volumes injected (c) Watercut vs. time (d) Watercut vs. pore volumes injected.
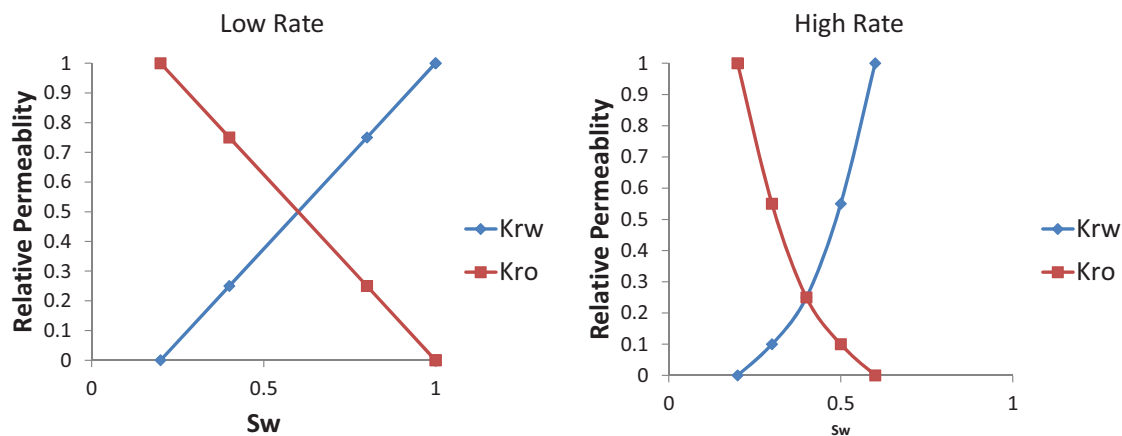
Figure 4.14: Rate-dependent relative permeability curves.

subseismically identified fractures. The third case (3HRP3H) has the modified relative permeability curves applied to both seismic and subseismically identified fractures. Not only is there higher recovery for the low rate case in all instances but there is also a crossover in the curves dependent on which fracture sets have the rate dependent relative permeability. Further work must be performed to understand if these mechanisms are possible in nature. These simplified models cannot capture the interaction between fault breccia, fault core and subseismic fractures where these rate effects will likely occur. A micromodel of the fracture network has been developed, where the recovery mechanism in these more complex models can be visualized.

4.6. Conclusions

A set of simple multiphase DFN models simulate production and watercut for seismic and subseismic faults and fractures. The simulations use a range of parameter variations including permeability ratio, capillary pressure, and relative permeability. The major portion of storage was assigned to subseismic faults.
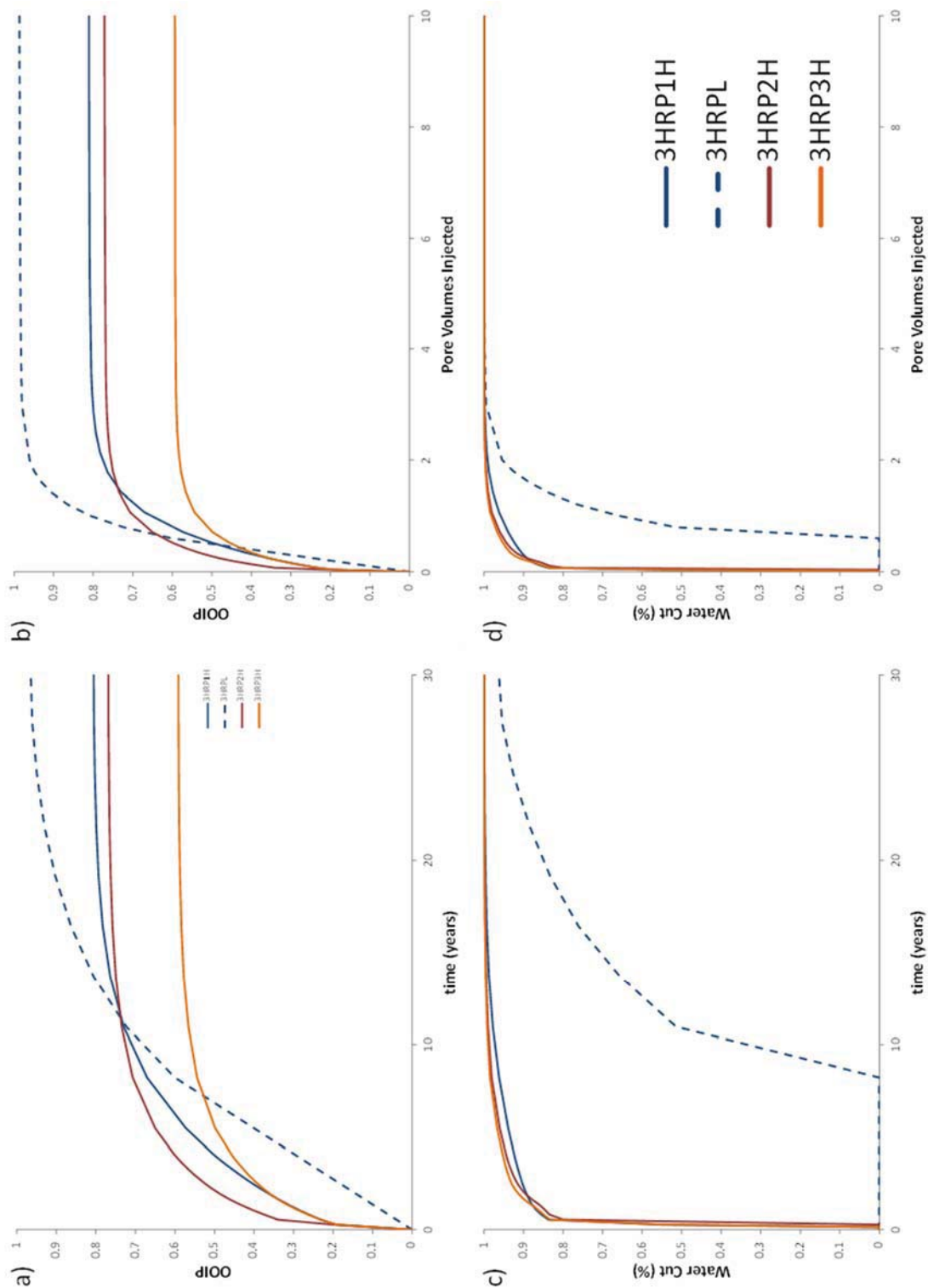
Figure 4.15: Comparison of recoveries and watercut with rate dependent relative permeabilities for the horizontal fracture model. (a) Fraction OOIP vs. time (b) Fraction OOIP vs. pore volumes injected (c) Watercut vs. time (d) Watercut vs. pore volumes injected.

The main objective of the simulations was the determination of conditions where lower production rate would result in higher ultimate recovery. This result did not appear in any of the simulations. The simulations were very consistent in showing that higher rates do not produce lower cumulative volumes over time than using lower rates as determined by crossovers of the low rate to the high rate cumulative production plots. We expect that this will not occur unless we use rate dependent multiphase properties, which may be difficult to rationalize. Although higher production rates appear to result in higher cumulative production, the higher rate has a cost in earlier water breakthrough and achieving the ultimate production with high water cuts that carry their own penalties in production cost and water handling.

The simulations used several ranges of permeability contrast. Stochastic fracture networks with preferred pathways produce strong breakthrough and delayed production from lower permeability faults. The simpler models with seismic and subseismic faults showed that porous but low-permeability portions of the basement reservoir, whether subseismic faults or lower conductivity portions of seismic faults, have delayed yields that continue to produce oil after water breakthrough, but with the penalty, again, of high water cuts.

4.7. <u>References</u>

1.   Nelson, R. A., Geologic Analysis of Naturally Fractured Reservoirs. 2nd ed.; Elsevier: 2001.

2.   Dershowitz, B.; LaPointe, P.; Eiben, T.; Wei, L., Integration of Discrete Feature Network Methods with Conventional Simulator Approaches. *SPE Journal* **1998,** *SPE 49069*.

3.   Yang, Y.-K. Finite-element Multiphase Flow Simulation. Doctorate of Philosophy, University of Utah, Salt Lake City, UT, 2003.

4.   Fu, Y. Multiphase Control Volume Finite Element Simulations of Fractured Reservoirs. Doctorate of Philosophy, University of Utah, Salt Lake City, UT, 2007.

5.   Araujo, H.; Lacentre, P.; Zapata, T.; Del Monte, A.; Dzelalija, F.; Repsol, Y. P. F.; Gilman, J.; Meng, H.; Kazemi, H.; Ozkan, E., Dynamic Behavior of Discrete Fracture Network (DFN) Models. *SPE Journal* **2004,** *SPE 93748*.

6.   Behrenbruch, P.; Du, P. Q., The Significance of Large Variations in Oil Properties of the Dai Hung Field, Vietnam. *SPE Journal* **1995,** *SPE 29302*.

7.   Sibbit, A. M., Quantifying Porosity and Estimating Permeability from Well Logs in Fractured Basement Reservoirs. *SPE Journal* **1995,** *SPE 30157*.

8.   Li, B.; Guttormsen, J.; Hoi, T. V.; Duc, N. V., Characterizing Permeability for the Fractured Basement Reservoirs. *SPE Journal* **2004,** *SPE 88478*.

9.   Mazurek, M.; Jakob, A.; Bossart, P., Solute Transport in Crystalline Rocks at Äspö - I: Geological Basis and Model Calibration. *Journal of Contaminant Hydrology* **2003,** *61*, 157-174.

10.   Chan, K.; Lam, D. D.; Ivanov, A.; Apisitsareekul, K.; Hai, L. V.; Nghi, N. C.; Hung, V. Q.; Lang, L. D., Production Improvement Water Shutoff for White Tiger Field. *SPE Journal* **2006,** *SPE 103329*.

11.   Wang, H. Multiphase, Multi-scale Simulation of Fractured Reservoirs. Doctorate of Philosophy, University of Utah, Salt Lake City, UT, 2008.

12.   Pooladi-Darvish, M.; Firoozabadi, A., Experiments and Modelling of Water Injection in Water-wet Fractured Porous Media. *Journal of Canadian Petroleum Technology* **2000,** *39* (3), 31-42.

13.   Kazemi, H.; Merrill, J., L. S.; Porterfield, K. L.; Zeman, P. R., Numerical Simulation of Water-Oil Flow in Naturally Fractured Reservoirs. *SPE Journal* **1976,** *SPE 5719*.

14.   Shook, G. M.; Li, D.; Lake, L. W., Scaling Immiscible Flow Through Permeable Media by Inspectional Analysis. *In Situ* **1992,** *16* (4), 311-349.

15. Kulkarni, M. M.; Rao, D. N. In *Characterization of Operative Mechanisms in Gravity Drainage Field Projects Through Dimensional Analysis (SPE 103230)*, SPE Annual Technical Conference and Exhibition, San Antonio, Texas, 24-27 September, 2006.

16. Van Golf-Racht, T. D., *Fundamentals of Fractured Reservoir Engineering*. Elsevier Scientific Publishing Company: New York, N.Y., 1982; p 710.